EFFECT OF CALCINATION TEMPERATURE ON THE COMPOSITION AND PHOTOCATALYTIC ACTIVITY OF NIGERIAN NATURAL ILMEN ITE, SPHALERITE AND WOLFRAMITE

By

Israila Joshua JOHN

DEPARTMENT OF CHEMICAL ENGINEERING

AHMADU BELLO UNIVERSITY

ZARIA NIGERIA

OCTOBER, 2014

EFFECT OF CALCINATION TEMPERATURE ON THE COMPOSITION AND PHOTOCATALYTIC ACTIVITY OF NIGERIAN NATURAL ILMEN ITE, SPHALERITE AND WOLFRAMITE

By

Israila Joshua JOHN, B. ENG. (ABU) 2009
MSc/ENG/8532/2011-2012

A THESIS SUBMITTED TO THE SCHOOL OF POSTGRADUATE STUDI ES,
AHMADU BELLO UNIVERSITY, ZARIA

IN PARTIAL FULFILMENT OF THE REQUIREMENTS FOR THE AWAR D OF A MASTER OF SCIENCE DEGREE IN CHEMICAL ENGINEERING

DEPARTMENT OF CHEMICAL ENGINEERING
AHMADU BELLO UNIVERSITY, ZARIA NIGERIA

OCTOBER, 2014

DECLARATION

I, JOHN Israila Joshua do solemnly declare that this thesis entitled “effect of calcination tempera ture on the composition and photocatalytic activity of natural ilmenite, sphalerite and wolframite was carried out by me in the Department of Chemical Engineering Ahmadu Bello University, Za ria. The information derived from the literature has been duly acknowledged in the text and list o f references provided. No part of this thesis was previously presented for another degree or diplo ma at this or any other institution.

Israila Joshua JOHN _____ _____

Signature Date

CERTIFICATION

This thesis entitled "EFFECT OF CALCINATION TEMPERATURE ON THE COMPOSITIO N AND PHOTOCATALYTIC ACTIVITY OF NATURAL ILMENITE, SPHALERITE AND WOLFRAMITE" by JOHN Israila Joshua meets the regulation governing the award of Master of Science Degree in Chemical Engineering of the Ahmadu Bello University Zaria. And it is theref ore approved for its contribution and literacy presentation.

Dr. A. Hamza Chairman Supervisory Committee	_____ Signature	_____ Date
Dr. B. Mukhtar Member Supervisory Committee	_____ Signature	_____ Date
Dr. I.A Mohammed-Dabo Head of Department	_____ Signature	_____ Date
Professor A.Z., Hassan Dean, postgraduate School Studies	_____ Signature	_____ Date

ACKNOWLEDGEMENT

I express my deepest gratitude to a number of people, without whom it would have not been possible for me to undertake this rigorous academic program during my two years at A.B.U. I sincerely thank my thesis supervisors Dr. A. Hamza and Dr. B. Mukhtar for their continuous support, encouragement, and insightful guidance during the course of my Masters studies at this University. I consider myself immensely fortunate and privileged to be able to work with them. I thank Dr. Hamza and Dr. Mukhtar for their reasoning that motivated me to delve deeper into my research. Your contribution has made me an independent thinker and researcher. I would like to appreciate the constant assistance, support and guidance afforded to me by teaching and non-teaching staff members of the department of Chemical Engineering, A.B.U Zaria. This achievement been accomplished, in no small measure, due to their professionalism and dedication which they demonstrated time after time.

I am also thankful to Dr Mohammed Dabo, the Head Chemical Engineering Department, A.B.U Zaria for his insightful comments, academic and moral advice and encouragement throughout my entire study period.

Thanks to my parents, Mr and Mrs Joshua for their unconditional love and support, without which I would not have been able to succeed in this endeavor. I am also thankful to my uncle Mr Dembo who has been a role model in my life.

I would like to thank my friends and colleagues Kehinde (whom I have been under his tutelage), Sani, Tsunatu, Johnson, Mr and Mrs Kingsley, Salisu, Namo, Mustapha amongst many others.

Finally, I wish to thank my special friends Mr. Felix Imologhome and Miss Malakai Wasossin for their continued support during the most difficult phase of my programme.

ABSTRACT

The growing concern for environmental preservation and the search for new energy sources to replace the fossil fuels have received much attention over the last four decades. Photocatalysis is a promising solution to these challenges. It is therefore, pertinent to investigate local indigenous photocatalysts and to increase their efficiency under visible light irradiation. Although visible light active photocatalysts require chemical modifications, their overall efficiencies can be significantly enhanced by controlling the structure and morphology. This structural and morphological modification can be achieved by calcination. Ilmenite, a natural occurring mineral ore of titanium as a visible light induced photocatalyst was characterized using XRF, XRD and specific surface area analysis (Sear's method). Elemental analysis of the raw ore indicates elemental titanium and iron constitute 69.0% and 22.2%, respectively, as the major constituent. XRD patterns of the raw and calcined ilmenite depicts that the rutile phase was the dominant polymorphs. The Specific Surface Area of ilmenite was found to increase from 33.40m^2/g to 66.92m^2/g as a result of increase in porosity and then decrease to 24.60m^2/g due to increase in crystal size as the calcination temperature increases. Photocatalytic activity of the samples was investigated for the degradation of methyl orange (MO) as a model pollutant under visible light irradiation. Calcination at 500^{o}C for two hours gave a better degradation rate constant of 1.3x10^{-3}min^{-1} and a degradation percentage of 19.07%. The structure and morphology of sphalerite, a mineral ore of ZnS was characterized by XRF, XRD, SEM and surface area analysis. The elemental composition of the sphalerite indicates that the main constituents are elemental zinc and sulphur of 58.6 and 16.0% respectively. XRD patterns of the raw and calcined samples depict a stepwise conversion of sphalerite into a ZnO composite photocatalyst. Photocatalytic test for the various samples were examined by measuring the degradation of MO. The result

indicates that sphalerite calcined at 700^{o}C exhibit a higher degradation efficiency of 90.93% and a rate constant of 3.58x10^{-3}min^{-1} due to phase change, decrease in crystal size, high specific surface area and oxygen vacancy defects of the calcined samples. Elemental composition of wolfram using XRF analysis indicated that the raw sample of the wolfram contains 64.45% tungsten and 15.10% iron. There XRD patterns did not show any remarkable differences in the number of peaks in the raw and calcined sample at 800^{o}C; however, the intensity of the peaks increases due to crystal growth. The specific surface area of the samples decreases gradually as calcination increases. This is attributed to the slight increase in crystal size from 35.45nm to 39.40nm. Photocatalytic activity of raw and calcined wolframite investigated shows that calcination at 600^{o}C for two hours gave a better degradation rate constant of 1.3x10^{-3}min^{-1} and a degradation percentage of 32.53%.

TABLE OF CONTENTS

LIST OF FIGURES

LIST OF TABLES

LIST OF ABBREVIATIONS

AOPs	Advance Oxidation Processes
BET	BrunauerEmmet Teller
CB	Conduction Band
CFCs	Chloroflurocarbons
DRS	Diffused Reflectance Spectroscopy
eV	Electron Volt
FWHM	Full Width at Half maximum
HOMO	Highest Occupied Molecular Orbital
HPO	Heterogeneous Photocatalytic Oxidation
I0	Raw Ilmenite
I500	IlmeniteCalcined at 500^{o}C
I600	IlmeniteCalcined at 600^{o}C
I700	IlmeniteCalcined at 700^{o}C
I800	IlmeniteCalcined at 800^{o}C
LUMO	Lowest Unoccupied Molecular Orbital
nm	Nanometer
PCA	Photocatalytic Activity

PZC	Point of Zero Charge
ROS	Reactive Oxidizing Specie
SSA	Specific Surface Area
S0	Raw Sphalerite
S500	SphaleriteCalcined at 500^{o}C
S600	SphaleriteCalcined at 600^{o}C
S700	SphaleriteCalcined at 700^{o}C
S800	SphaleriteCalcined at 800^{o}C
UV	Ultraviolet
VB	Valence Band
VLA	Visible Light Active
W0	Raw Wolframite
W500	WolframiteCalcined at 500^{o}C
W600	WolframiteCalcined at 600^{o}C
W700	WolframiteCalcined at 700^{o}C
W800	WolframiteCalcined at 800^{o}C
XPS	X-ray Photoelectron Spectroscopy
XRD	X- Ray Diffraction
XRF	X- Ray Fluorescence
SEM	Scanning Electron Microscopy

CHAPTER ONE

INTRODUCTION

1.1 PREAMBLE

The increase in energy consumption and the growing concern for environmental preservation along with the concept of distributed generation motivates the search for new sources of power. Heterogeneous photocatalysis has received much attention and has been an active research area over the last four decades. It is a promising solution to energy generation and environmental problems which has led to applications such as air and water purification systems, self- cleaning and self- sterilizing surfaces, solar cells and hydrogen production from water dissociation reaction (Murat, 2011). Since the discovery of photo- electrochemical splitting of water using titanium dioxide electrode under ultraviolet light by Fujishima and Honda in 1972, titanium dioxide has become the state- of- the- art material for photocatalytic reactions due to its relatively high efficiency under UV irradiation, abundance, low cost, photo- corrosion resistance and biocompatibility (Jina, 2010). Also, different kinds of semiconductors have been widely investigated as possible photocatalysts for photooxidation or photoreduction of organic pollutants. Various semiconductors with highly photoreductive activity have been developed in the past three decades (Yan *et al*, 2008). In this area, some of the most widely studied semiconductors are sphalerite and wolframite.

However, a fatal disadvantage for most photocatalysts is their large band gap (3.2, 3.0, 3.6 and 2.7 eV for anatase (TiO_2), rutile (TiO_2), sphalerite (ZnS) and wolframite respectively), which makes them effective under UV light irradiation (Pankaj, 2012). So their application is constrained to only the UV light range which makes up only 4-5 % of the solar spectrum, whereas approximately 40-50% of solar photons are in the visible region (Pelaez, *et al*, 2012). To extend their application into the dominant visible light range in solar light, many efforts have

been made but challenges still remain in finding new materials that can effectively utilize the visible light irradiation. Therefore, effective utilization of visible light has become one of the most difficult challenges in photocatalysis, and it is highly desirable to develop a photocatalyst that can use visible light in high efficiency under solar irradiation.

Various strategies have been adopted for improving the photocatalytic efficiency of photocatalysts. They can be summarized as either morphological modification, such as increasing surface area and porosity, or as chemical modifications, by incorporation of additional components in the photocatalyst structure. Although visible light active (VLA) photocatalysts require chemical modifications, their overall efficiencies have been significantly enhanced by controlling the semiconductor morphology (Pelaez *et al*, 2012).

Chemical modifications by non-metal doping of photocatalysts has shown great promise in achieving visible light active (VLA) photocatalysis, with nitrogen being the most promising dopant (Ibid) due to its comparable atomic size with oxygen, small ionization energy and high stability.

The main aim of this work is to study the chemical and morphological modification of three naturally occuring photocatalysts namely ilmenite, sphalerite and wolframite through calcinations at different temperatures in a furnace. More importantly Ilmenite, Sphalerite and Wolframite are found in great quantities in various parts of Nigeria (RMRDC, 2010). Naturally occurring photocatalysts generally are cheaper than synthetic photocatalysts (Yan *et al*, 2008). They could function well in visible light and may be suggested as cost-effective photocatalysts with potential applications in

environmental treatment and other solar energy-based technologies.

1.2 PROBLEM STATEMENT

i. High band gap of conventional semiconductor photocatalysts such as titanium dioxide (TiO_2) and sphalerite (ZnS) limits their applications to UV light.

ii. Synthesis of photocatalysts involves high purity chemicals that are expensive, which necessitate investigating the use of natural minerals.

iii. Effect of calcination temperature on the composition and photocatalytic activity of Nigeria natural ilmenite, sphalerite and wolframite has not been reported in the open literature.

1.3 AIM AND OBJECTIVES

The aim of this research work is to study the effect of calcination temperatures (500-800^{o}C) on the composition and photocatalytic activity of natural ilmenite, sphalerite and wolframite.

The specific objectives are:

i. To characterize the Ilmenite, Sphalerite and Wolframite before and after calcination using UV-Vis absorbance, XRD, XRF, SEM and surface area analysis.

ii. To calcine the Ilmenite, Sphalerite and Wolframite at 500, 600, 700 and 800^{o}C for two hours.

iii. To study photocatalytic activity by monitoring the degradation of methyl orange (a model pollutant) using raw and calcined samples of natural Ilmenite, Sphalerite and Wolframite under visible irradiation

iv. To study the effect of photocatalysts dosage and initial substrate concentration of methyl orange on photocatalytic process.

1.4 SCOPE OF THE WORK

This work is limited to the investigation of the effect of calcinations (at 500^{o}C, 600^{o}C, 700^{o}C and 800^{o}C for two hours) on the composition, physical properties and photocatalytic activity of

representative samples of Nigerian Ilmenite, Sphalerite and Wolframite using methyl orange as a model substrate under visible light irradiation.

1.5 RESEARCH JUSTIFICATION

i. Availability of the raw materials, Ilmenite, (Barkin Ladi, Plateau State), Sphalerite (Abuni, Nassarawa State), Wolframite (Anka, Zamfara State).

ii. Semiconductor photocatalysis has received much attention during last three decades as a promising solution for both energy generation and environmental remediation.

iii. The amount of energy utilized in this technology is low, as the process can be driven by sunlight which is a renewable energy source.

iv. Exploitation of these ores will open up market and enhance regional development.

CHAPTER TWO

LITERATURE REVIEW

2.1 PHOTOCATALYSIS

Photocatalysis is the acceleration of a photoreaction in the presence of a catalyst. It is widely used to describe the process in which the acceleration of a reaction occurs when a material, usually a semiconductor, interacts with light of sufficient energy (or of a certain wavelength) to produce reactive oxidizing species (ROS) which can lead to the photocatalytic generation of $H_2$and transformation of a wide variety of molecules (Pelaez *et al*, 2012). It must be noted that during the photocatalytic reaction, at least two events must occur simultaneously in order for the successful production of reactive oxidizing species to occur. Typically, the first involves the oxidation of dissociatively adsorbed H_2O by photogenerated holes, the second involves reduction of an electron acceptor by photoexcited electrons; these reactions lead to the production of a hydroxyl and superoxide radical anion, respectively.

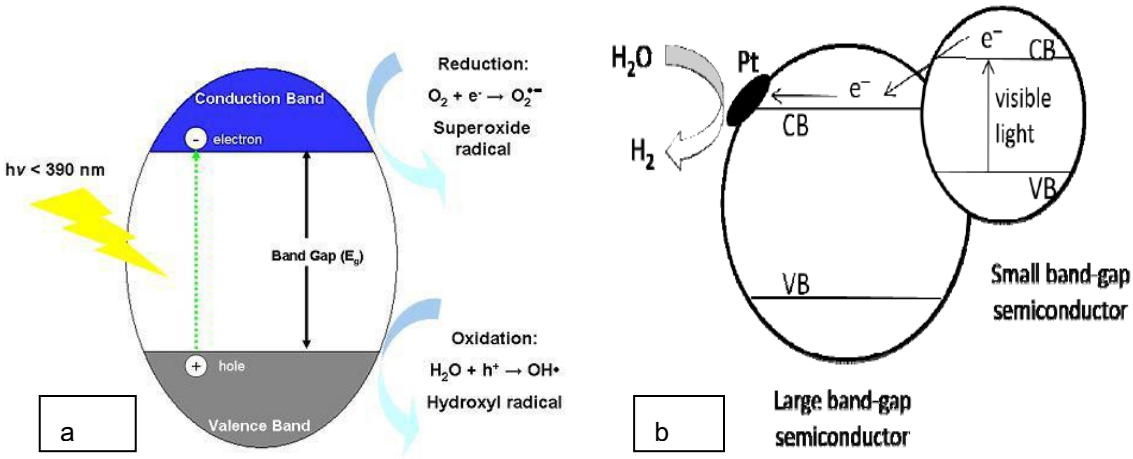

Figure (2.1) Simplified mechanism of (a) semiconductor photocatalytic process, (Pelaez, *et al*, 2012). (b) visible-light induced photocatalyst sensitized with small Band-Gap semiconductor called Hybrid or Composite photocatalysts, (Pankaj, 2012).

It is clear that photocatalysis implies photon-assisted generation of catalytically active species rather than the action of light as a catalyst in a reaction (Suppan, 1994). If the initial

photoexcitation process occurs in an adsorbate molecule, which then interacts with the ground state of the catalyst substrate, the process is referred to as a “catalyzed photoreaction”, if, on the other hand, the initial photoexcitation takes place in the catalyst substrate and the photoexcited catalyst then interacts with the ground state adsorbate molecule, the process is a "sensitized photoreaction" (Wang*et al*, 1997).

When a photocatalyst is illuminated by light with energy equal to or greater than the band-gap energy, the valence band electrons can be excited to the conduction band, leaving a positive hole in the valence band. In the case of anatase TiO_2, the band gap is 3.2 eV, therefore UV light ($\lambda \leq$ 387 nm) is required. The absorption of a photon of this energy will excites an electron to the conduction band (e^-_{CB}) generating a positive hole in the valence band (h^+_{VB}) (Ohtani, 2011) as shown in equation 2.1.

$$TiO_2 + h\nu \rightarrow h^+_{VB} + e^-_{CB}. \quad (2.1)$$

Charge carriers can be trapped as Ti^{3+} and O^- defect sites in the TiO_2 lattice, or they can recombine, dissipating energy (Hoffman*et al*, 1994). Alternatively, the charge carriers can migrate to the catalyst surface and initiate redox reactions with adsorbates. Positive holes can oxidize OH- or water at the surface to produce •OH radicals (Eq. 2.2) which, are extremely powerful oxidants. The hydroxyl radicals can subsequently oxidize organic species with mineralization producing mineral salts, CO_2 and H_2O (Eq. 2.5) (Ohtani, 2011).

$$e^-_{CB} + h^+_{VB} \rightarrow \text{energy} . \quad (2.2)$$

$$H_2O + h^+_{VB} \rightarrow {}^{\bullet}OH + H^+ \quad (2.3)$$

$$O_2 + e^-_{CB} \rightarrow O_2{\bullet}^- \quad (2.4)$$

$$\bullet OH + \text{pollutant} \rightarrow H_2O + CO_2 \quad (2.5)$$

$$O_2{\bullet}^- + H^+ \rightarrow \bullet OOH. \quad (2.6)$$

$$\bullet OOH + \bullet OOH \rightarrow H_2O_2 + O_2 \quad (2.7)$$

$$O_2^{\bullet-} + \text{pollutant} \rightarrow CO_2 + H_2O \quad (2.8)$$

$$\bullet OOH + \text{pollutant} \rightarrow CO_2 + H_2O \quad (2.9)$$

Electrons in the conduction band can be rapidly trapped by molecular oxygen adsorbed on the titania particle, which is reduced to form superoxide radical anion ($O_2^{\bullet-}$) (Eq, 2.4) that may further react with H^+ to generate hydroperoxyl radical ($^{\bullet}OOH$) (Eq. 2.6) and further electrochemical reduction yields H_2O_2 (Eq. 2.7). These reactive oxygen species may also contribute to the oxidative pathways such as the degradation of a pollutant (Eq. 2.8 and 2.9) (Choi, *et al*, 1994).

2.2 TYPES OF PHOTOCATALYSIS

2.2.1 Homogeneous Photocatalysis

In homogeneous photocatalysis, the reactants and the photocatalysts exist in the same phase. The most commonly used homogeneous photocatalysts include, ozone, transition metal oxide and ph oto-Fenton systems (Fe^+ and Fe^+/H_2O_2). The reactive species is the •OH which is used for differe nt purposes. According to Pankaj Chowdhury, (2012), **t**he mechanism of hydroxyl radical produc tion by ozone can follow two paths as follows:

$$O_3 + h\nu \rightarrow O_2 + O(1D). \quad 2.10$$

$$O(1D) + H_2O \rightarrow \bullet OH + \bullet OH. \quad 2.11$$

$$O(1D) + H_2O \rightarrow H_2O_2. \quad 2.12$$

$$H_2O_2 + h\nu \rightarrow \bullet OH + \bullet OH. \quad 2.13$$

Similarly, the photo-Fenton system produces hydroxyl radicals by the following mechanism

$$Fe^{2+} + H_2O_2 \rightarrow HO\bullet + Fe^{3+} + OH^{-}. \quad 2.14$$

$$Fe^{3+} + H_2O_2 \rightarrow Fe^{2+} + HO\bullet 2 + H^{+}. \quad 2.15$$

$$Fe^{2+} + HO\bullet \rightarrow Fe^{3+} + OH^{-}. \quad 2.16$$

In photo-Fenton type processes, additional sources of OH radicals should be considered: through photolysis of H_2O_2, and through reduction of Fe^{3+} ions under UV light:

$$H_2O_2 + h\nu \rightarrow HO\bullet + HO\bullet. \quad 2.17$$

$$Fe^{3+} + H_2O + h\nu \rightarrow Fe^{2+} + HO\bullet + H^{+}. \quad 2.18$$

The efficiency of Fenton type processes is influenced by several operating parameters like concentration of hydrogen peroxide, pH and intensity of UV. The main advantage of this process is the ability of using sunlight with wavelength up to 450 nm, thus avoiding the high costs of UV lamps and electrical energy (Suresh, *et al*, 2012).The disadvantages of the fenton type process are the low pH values which are required, since iron precipitates at higher pH values and the fact that iron has to be removed after treatment.

2.2.2 Heterogeneous Photocatalysis

Heterogeneous catalysis has the catalyst in a different phase from the reactants. Heterogeneous photocatalysis is a discipline which includes a large variety of reactions: mild or total oxidations, dehydrogenation, hydrogen transfer, $^{18}O_2$–$^{16}O_2$ and deuterium-alkane isotopic exchange, metal deposition, water detoxification, gaseous pollutant removal.

Most common heterogeneous photocatalysts are semiconductors, which have unique characteristics. Unlike the metals which have a continuum of electronic states, semiconductors possess a void energy region where no energy levels are available to promote recombination of an electron an

d hole produced by photoactivation in the solid (Jina Choi, 2010). The void region, which extend s from the top of the filled valence band to the bottom of the vacant conduction band, is called th e band gap. When light falls on these semiconductors, the electron present in the valence band ju mps to the conduction band, a result of which is the generation of a positive hole. The recombina tion of the electron and the hole must be prevented as much as possible if a photocatalyzed reacti on is to be favoured (Pelaez, *et al* 2012). The ultimate goal of the process is to have a reaction be tween the activated electrons with an oxidant to produce a reduced product, and also a reaction b etween the generated holes with a reductant to produce an oxidized product. Due to the generatio n of positive holes and electrons, oxidation-reduction reactions take place at the surface of semic onductors. In the oxidative reaction, the positive holes react with the moisture present on the surf ace and produce a hydroxyl radical.

Oxidative reactions due to photocatalytic effect are illustrated as follows:

$$UV + MO \rightarrow MO\ (h + e^{-}). \qquad 2.19$$

Here MO stands for metal oxide

$$h^{+} + H_2O \rightarrow H^{+} + \bullet OH. \qquad 2.20$$

$$2\ h^{+} + 2\ H_2O \rightarrow 2\ H^{+} + H_2O_2. \qquad 2.21$$

$$H_2O_2 \rightarrow HO\bullet + \bullet OH. \qquad 2.22$$

The reductive reaction due to photocatalytic effect is illustrated as follows:

$$e^{-} + O_2 \rightarrow \bullet O_2. \qquad 2.23$$

$$\bullet O_2{-} + HO\bullet 2 + H^{+} \rightarrow H_2O_2 + O_2. \qquad 2.24$$

$$HOOH \rightarrow HO\bullet + \bullet OH. \quad 2.25$$

Ultimately, the hydroxyl radicals are generated in both the reactions. These hydroxyl radicals are very oxidative in nature and non selective with redox potential of (E_0 = +3.06 V).

2.3 PHOTOCATALYST MATERIALS

Photocatalysts are often inorganic solid materials (Fujishima and Rao, 1997). They are usually crystals and its crystallinity is often determined by an X-ray diffraction (XRD) pattern. A photocatalytic material is also a substance that generates catalyst activity energy from light. It alters the rate of a chemical reaction when exposed to sunlight (Suresh, 2012).

The band gap of a material decides whether it can function as a photocatalyst or not. The bands that are filled with electrons are called the valence band and the empty bands are called the conduction band. The energy difference between the conduction band and the valence band is called the band gap. If the valence band cannot be completely filled with electrons, no band gap will be present and the material is called a metal. If the valence band is completely filled with electrons and a band gap greater than zero and less than 5eV, it will be called a semiconductor. A material with a band gap higher than 5eV is called an insulator (Jos *et al*, 2004).

There are several materials known for their photocatalytic activity of which most of them are metal oxides. Since the discovery of its photocatalytic effect by Honda and Fujishima in 1978, titanium dioxide has become the most popular photocatalytic material due to its abundance; low cost, chemical stability, biocompatibility and high efficiency under UV light (Murat, 2012).

Though not as popular as titanium dioxide, zinc oxide has been getting increasing attention as a photocatalytic material due to its similar electronic structure and catalytic efficiency with TiO_2. While zinc oxide can be a more efficient photocatalyst in near UV excitations compared to titanium dioxide, it has the problem of photo- corroding itself, limiting its wide use (van de Krol,

Liang *et al*. 2008).

TABLE 2.1. Band-gap energies for some common semiconductor materials.

Semiconductor	Band Gap (eV)	Semiconductor	Band Gap (eV)
Fe_2O_3	2.2	CdS	2.4
TiO_2	3.0~3.2	ZnS	3.7
WO_3	2.7	CdSe	1.7
ZnO	3.2	GaP	2.3
SnO_2	3.5	GaAs	1.4
$SrTiO_3$	3.4	SiC	3.0

2.4 APPLICATIONS OF PHOTOCATALYSIS

2.4.1 Hydrogen Generation

The world is moving from solid to liquid to gas fuels for future energy sources. The basic idea is decarbonization of the fuel. Coal has the lowest H:C ratio (0.5:1), for LPG the ratio goes up to 2.6:1 and for natural gas the ratio again increases to 4:1. Hydrogen is the fuel having H:C ratio of infinite (Murat, 2011). Hydrogen is the most abundant element in the universe found in water, life forms and hydrogen fuel. The driving forces for the energy transition towards hydrogen are many, but three major factors are i) growing energy demand, ii) oil scarcity in the near future and iii) risk of climate change. According to Murat (2011), by 2050 world population will be 10 billion and the expected energy demand will be doubled. Coal and oil are promising energy sources but still we need some other energy sources which are more abundant and can make up the future energy demand.

2.4.2 Water Purification

Water is the most precious natural resource in the world embracing over 70 % of the earth surface. In spite of this the accessibility of safe drinking water is a high priority issue for the survival of mankind as well as animals. This is because of the fact that water resources such as rivers, lakes and oceans are being contaminated by human beings through over-use and wastage. This affects natural environment as well as human health. Water pollutants are classified into two main groups namely i) point source (single source), and ii) non-point source (many sources) respectively (Murat, 2011). Causes of water pollution are many but major sources can be categorized as industrial waste, sewage and wastewater, agricultural waste, oil spills, marine dumping and nuclear wastes. The World Health Organization (W.H.O) reported that in 2008 some 884 million people still relied upon unimproved water sources – 84% of whom were living in rural areas. Many more are surviving by drinking microbiologically unsafe water and experiencing the agony of waterborne diseases including typhoid, hepatitis, and cholera (Pankaj, 2012).

The removal of harmful matters from wastewater and detoxification of pollutants in surface water, and groundwater is a key issue in the world. Secondary treatment helps in organic matter decomposition to some extent, but major oxidation process occurs in tertiary treatment where wastewater is disinfected by Cl_2, O_3 or UV light. There are numerous methods under tertiary treatment which can be classified into biological, chemical or physical oxidation process. Biological oxidations are inexpensive but presence of toxic pollutants creates difficulties during the operation. Treatments of pollutant at high temperature (thermal treatment) are quite successful but not economically feasible. On the other hand, chemical oxidation with the help of several oxidants such as H_2O_2, O_3, Cl_2, and ClO_2 do not experience such problem, although they could not afford complete mineralization of water pollutants (Jina, 2010). Advanced oxidation

processes (AOPs) have been introduced to eliminate different potentially harmful compounds that could not be effectively removed by conventional treatment processes. These AOPs include O_3/UV, H_2O_2/UV, O_3/H_2O_2/UV and TiO_2/UV. Among the AOPs, TiO_2/UV based photocatalytic oxidation processes have received great attention in the recent years as an alternative for water detoxification (Murat, 2011).

2.4.3 Self-Sterilization and Self- Cleaning Coatings

Although semiconductor photocatalysts performs very efficiently in their powdered form, an immobilized form is necessary for most practical applications (Miyauchi, *et al*. 2002). Titanium dioxide for instance being a wide band gap semiconductor is transparent, thus allowing its use as a thin film on a variety of surfaces without degrading the aesthetic view. Following the first demonstration of self-cleaning concept on titanium dioxide coated ceramic tiles by Hashimoto *et al*. in 1992; several commercial applications have emerged by large such as TOTO, Pilkington, PPG, Saint- Gobain, AFG (Murat, 2011).

Self- cleaning effect by photocatalytic titanium dioxide coating can be applied on a glass window. When titanium dioxide is illuminated by UV light (solar illumination), it starts decomposing contaminants to minerals and carbon dioxide. At the same time, titanium dioxide becomes superhydrophillic and it retains this property for a while after illumination ceases. This enables the easy washing (typically by rain) of stains adsorbed on the titanium dioxide surface as water penetrates to the molecular- level space between the stain and titanium dioxide surface (Jina, 2010).

2.4.4 Air Purification

The photocatalytic reactivity of titanium oxides can be applied for the reduction or elimination of polluted compounds in air such as NOx, cigarette smoke, as well as volatile compounds arising

from various construction materials. Also, high photocatalytic reactivity can be applied to protect lamp-houses and walls in tunneling, as well as to prevent white tents from becoming sooty and dark. Atmospheric constituents such as chlorofluorocarbons (CFCs) and CFC substitutes, greenhouse gases, and nitrogenous and sulfurous compounds undergo photochemical reactions either directly or indirectly in the presence of sunlight. In a polluted area, these pollutants can eventually be removed (Murat, 2011).

2.5 CHARACTERIZATION OF PHOTOCATALYSTS

2.5.1 X-Ray Diffraction (XRD) Spectroscopy

X-ray diffraction (XRD) is used to examine the crystal structures of photocatalysts particles. It is a method of determining the arrangement of atoms within a crystal, in which a beam of X-rays strikes a crystal and diffracts into many specific directions using a diffractometer. It provides detailed information on the crystallographic structure and physical properties of materials and thin films.

2.5.2 X-Ray Florescence (XRF) Spectroscopy

X-ray fluorescence is the emission of characteristic “secondary” (or fluorescent) X-rays from a material that has been excited by bombarding with high energy X-rays or gamma rays. The phen omenon is widely used for elemental and chemical analysis of minerals.

2.5.3 UV-Vis Absorption Spectroscopy

The absorbance of any specie in solution can be determined using the Beer-Lambert’s law. This a bsorbance can be converted to concentration to determine the concentration of any given specie i

n a sample.

Beer-Lambert's Law

According to the Lambert-Beer Law, Chun and Yizhong (1999), the absorbance (*A*) of methyl orange (MO) is proportional to its concentration (*c*), this generally followed the following equation:

$$\boldsymbol{A = \varepsilon bc}. \qquad 2.26$$

Where $\boldsymbol{\varepsilon}$is the molar absorption coefficient and $\boldsymbol{b}$is the thickness of the absorption cell. In experiments, all the testing parameters are kept constant, so that $\boldsymbol{\varepsilon}$and $\boldsymbol{b}$can be onsidered as a constant. Therefore, the changes of the concentration ($\boldsymbol{c}$) of MO aqueous solution can be determined by a UV-Vis spectrophotometer. As for the MO aqueous solution with low concentration, its photocatalytic decolorization is a pseudo-first-order reaction and its kinetics may be expressed as follows (Rashed and El-Amin, 2007).

$$\mathbf{Ln\ A = LnAo + }\boldsymbol{k}\mathbf{t}. \qquad \mathbf{2.27}$$

Where k is the apparent rate constant and A_0 and A_t are the initial and reaction absorbance of aqueous solution, respectively.

2.5.4 UV-Vis Diffuse Reflectance Spectroscopy

Diffuse Reflectance Spectroscopy provides an indication of the visible light activity of the photo catalysts. Diffuse reflectance spectra are obtained with UV-vis spectrometer and can be converted from reflection to absorption spectra by the Kubelka-Munk method.

2.6 FACTORS AFFECTING PHOCATALYST ACTIVITY

2.6.1 Band Structure

The general understanding of the mechanism of photocatalysis is that photoabsorption of a semiconducting material occurs to excite electrons from the valence band (VB) to the conduction band (CB) leaving positive holes in the VB, i.e., electron–hole pair (e^-h^+) generation (Pelaez, *et al* 2012). An important point is that photoabsorption and (e^-h^+) generation are inextricably linked; a VB electron is not excited after photoabsorption. This inter-band (band-to-band) excitation is often illustrated by three bands, CB, forbidden band (band gap) and VB, in which an electron moves vertically from the VB to CB, i.e., no spatial change in the position of an electron, though sometimes an electron migrates from the VB to CB spatially (Ohtani, 2011). Anyway, the above-mentioned interpretation seems to be a little strange considering the meaning of band structure and band-to-band transition, in which electrons are not localized and therefore electrons and positive holes can migrate within a crystal; an unlocalized excitation state may be described as "photoexcited crystal", e.g., an excited state of titania, without showing localized e^-,h^+. Do e^- and h^+ migrate in the CB and VB, respectively, after photoabsorption, i.e., photoexcitation? When we illustrate the electronic structure of a molecule, lines are drawn to show the electronic state; the length of these lines does not mean spatial distribution of electrons in those states. This should also be the case for semiconducting (or insulating) materials, and band-to-band transition just means that an electron in the VB is excited to the CB without clarifying the location of e^- and h^+.

A possible interpretation of a better understanding for e^- h^+ location is that there are sites trapping e^- or h^+ in the crystal lattice and that e^- and h^+ are trapped by these sites "immediately" after the band-to-band transition, i.e., photoabsorption (Suresh, *et al*, 2012). Location of e^- and h^+ in the initial stage of photocatalysis as well as the rate should be controlled by the density and spatial distribution of these traps in a photocatalyst. However, there is little information on the

density and spatial distribution of traps, since the structure of traps has not been fully clarified. The possible surface traps may be reaction sites, but not "active sites". It is thought that Fermi level is located just below the CB bottom and above the VB top for n-type and p-type semiconducting materials (Suppan, *et al* 1994), respectively (Fermi level is a kind of measure of equilibrium electrochemical potential of a solid material). Most metal oxides are categorized as n-type semiconductors with Fermi levels more cathodic (higher) than the standard electrode potential of an electrolyte in contact with the metal oxide, and thereby electrons in donor levels slightly below the CB are injected into the electrolyte to form a space charge (depletion) layer with an electric field, i.e., Schottky barrier. In the 1980's, it was thought that this inner electric field separates e^- h^+ effectively; i.e., e^- and h^+ migrate to the bulk and surfaces of semiconductor electrodes and particles, but it seems that this is not the case for untreated photocatalyst particles because of the expected large thickness of this layer due to very low density of donor levels in ordinary photocatalyst particles.

2.6.2 Band Gap

Since the ability of a photocatalyst is essentially governed by its band position, i.e., conduction-band (CB) bottom and valence-band (VB) top, as described in "Band structure", estimation of the potential of the CB bottom and VB top is important to predict the possibility for driving a photocatalytic reaction from the thermodynamic point of view. A general way for such estimation involves measurements of flat-band potential and band gap corresponding to the potential of the CB bottom and difference in potential between the CB bottom and VB top, respectively, enabling estimation of the potential of the VB top from them. Optical band gap can be estimated using the following equation (Ohtani, 2011).

$$(\alpha\nu)^{\frac{1}{n}} \propto h\nu - E_g, \quad . \quad . \quad . \quad . \quad . \quad . \quad . \quad . \quad .2.29$$

Where α, *h*, ν, *E*g and *n* are absorption coefficient, Planck constant, oscillation frequency, optical band gap and constant relating to a mode of transition. The constant *n* is ½, $\frac{3}{2}$, or 2 for allowed direct transition, forbidden direct transition or indirect transition, respectively, but the second forbidden direct transition has often been neglected. It is described in textbooks of semiconductor physics (or electronics) that by checking linearity of plots of $(\alpha\nu)^{\frac{1}{n}}$against *h*ν using *n* as 2 or ½, the mode of transition of a given crystal and optical band gap are estimated, the latter of which is estimated by an x-intercept of the straight line (Suresh, *et al*, 2012).

Another problem in the band-gap energy estimation is the influence of impurity or surface electronic states on absorption spectra; spectral curves at the absorption edge region may be markedly modified to give smaller band-gap energy, and it is very difficult to extract a part of the absorption due to band-gap excitation from that by impurities (dopants) or surface states. Therefore, especially for doped samples, discrimination of narrowing of the band gap and overlapping of absorption by bulk or surface modification from shift of absorption to longer wavelengths is difficult.

2.6.3 Crystallinity

Photocatalysts are often inorganic solid materials. They are usually crystals and the crystalline form is often determined by an X-ray diffraction (XRD) pattern. One of the problems in XRD analyses is that only crystals are detected, while an amorphous part, if present in samples, exhibits no diffraction peaks. Hallow may appear for amorphous parts, but there has been no report showing quantitative determination of amorphous content. Thus, amorphous content must be determined as a test of crystalline part and therefore precise determination of crystalline

content is necessary. It is believed that, in principle, XRD peak intensity is proportional to content of corresponding crystallites, but a problem is how can a global standardbe obtained for samples of each crystal, because smaller crystallites may exhibit lower peak intensity (Ohtani, 2011). A possible interpretation of this problem is that the outermost surface of particles cannot be involved in a crystal, which can be defined only for bulk, and the ratio of surface/bulk becomes appreciable when the size of crystallites becomes small. Thus, precise analysis of crystalline content can be guaranteed when pure crystalline particles included in a sample are extracted and used for making an XRD calibration curve (Klug and Alexander, 1974) based on the assumption that crystallites and amorphous particles are separated, but not in the form of, for example, a core-shell structure. In other words, if a sample particle is of a core-shell structure, precise determination of crystalline content may be very difficult.

Confusion regarding the term "crystallinity" arises because the term is discussed on the basis of sharpness of an XRD peak, e.g., "Sharpness of the peak indicated higher crystallinity of a photocatalyst." Since the width of an XRD peak reflects the size of a particle, i.e., the depth of crystallites measured in the direction vertical to a corresponding lattice plane (Scherer equation) (Suresh, *et al*, 2012), peak sharpness shows the size of crystallites. In this sense, "crystallinity" is used to show how crystallites grow to be larger-sized particles. Another usage of the term "crystallinity" is to show perfectness of crystals, i.e., higher crystallinity means lesser density of crystalline defects. As mentioned above, sharpness of XRD peaks might be a measure of crystallite size. Assuming that larger crystallites possess smaller density of crystalline defects, sharpness of XRD peaks can also be a relative measure of "crystallinity".

2.6.4 Surface Area

The photocatalytic activity of a semiconductor photocatalyst involves adsorption of the compound (to be oxidized) and trapping of holes and electrons on the catalyst surface. Number of trap centers is important and strongly influences the recombination rate. It is indeed, the competition between charge- carrier recombination and trapping that determines the overall quantum efficiency of a photocatalyst. The surface area of a photocatalysts determines the number of adsorption sites (Ohtani, 2012).

2.6.5 pH

The oxide/electrolyte interface has an electrical surface charge, which strongly depends on the p H of the medium (Jina, 2010). The electrokinetically mobilized charge is a determining paramete r in the colloidal stability of the oxide particle suspensions (Murat, 2011). This involves the study of particle sizing depending on the pH; if the pH is equal to the Point of Zero Charge (PZC), the particles aggregate and ensembles are larger. The pH of the aqueous solution significantly affects the photocatalysts, including the charge of the particle and the size of the aggregates it forms. 30 0nm sizes increases to 2-4μm when dispersion reaches PZC. The zero surface charge yields zero electrostatic surface potentials that cannot produce the interactive rejection necessary to separate the particles within the liquid. This induces a phenomenon of aggregation and the photocatalysts clusters become larger. This effect is clearly related to the capability of the suspension for transm itting and/or absorbing light. Furthermore, larger clusters sediment more quickly than small parti cles, thus the agitation necessary to maintain perfect homogeneity must be more vigorous. The P ZC for TiO_2 is around 7. Above and below this value, the catalyst is negatively or positively char ged according to:

$$-TiOH \leftrightarrow -TiO^- + H^+. \qquad 2.30$$

$-TiOH_2^+ \leftrightarrow TiOH + H^+$. 2.31

The abundance of all the species as a function of pH: $TiOH \geq 80\%$ when $3 \leq pH \leq 10$; $TiO^- \geq 20\%$ if $pH \geq 10$; $TiOH_2^+ \geq 20\%$ when $pH \leq 3$(Wolfrum and Turchi, 1992). Under these conditions, the photocatalytic degradation of the ionisable organic compounds is affected by the pH. At first sight a very acidic solution appears to be detrimental and a very basic solution to be favourable, since the variations are modest or non-existent around neutrality. In many cases, a very important feature of photocatalysis is not taken into account when it is to be used for decontamination of water, is that during the reaction, a multitude of intermediate products are produced that may behave differently depending on the pH of the solution. To use only the rate of decomposition of the original substrate could yield an erroneous pH as the best for contaminant degradation. Therefore, a detailed analysis of the best pH conditions should include not only the initial substrate, but also the rest of the compounds produced during the process (Jina, 2010).

2.6.6 Photocatalyst Dosage

There are number of studies in the literature on the influence of catalyst concentration on process efficiency. Although the results are quite different, it may be deduced from all of them that incident radiation on the reactor and length of path inside the reactor are fundamental in determining optimum concentration. This summarizes the conclusions if the radiation comes from a source placed outside the photoreactor (as in a reactor illuminated by solar radiation):

If the path length is short (1-2cm maximum), reaction rate is obtained with 1-2 gL^{-1} of TiO_2.

If the path length is several centimetres long, the appropriate catalyst concentration is several hundred milligrams per litre (Ohtani, 2011).

In all the cases described above, a "screening" effect is produced when TiO_2 concentration is ver y high. The reaction rate diminishes due to the excessive opacity of the solution, which prevents the catalyst farthest in from being illuminated. Approximately, $1gL^{-1}$ of catalyst reduces transmis sivity to zero in a 1-cm-inner-diameter cylinder. For the solar reactors, it is therefore necessary to find out the optimum catalyst concentration experimentally. That is, the minimum concentration at which the maximum reaction rate is obtained. When catalysts concentration is very high, after travelling a certain distance on an optical path length, turbidity impedes further penetration of lig ht in the reactor (Pankaj, 2012). The percentage of photons absorbed by the suspension and the p ercentage of photons scattered by the TiO_2particles is a very complex problem that cannot be sol ved experimentally, but must be experimentally estimated.

2.6.7 Substrate Concentration

Photocatalytic activity of semiconductor photocatalysts is strongly dependent on the underlying substrate due to the possible chemical interaction between the photocatalysts and the substrate material. The substrate molecules reacts with the photo-generated hole and/or hydroxyl radical and degrade to different compounds, thus, the concentration of the substrate continuously changes reaction progresses. The rate varied as a function of the substrate concentration according to Langmuir-type equation shown in equation 2.32 (Ohtani, 2011).

$$r = \frac{dC_{H_2}}{dt} = \frac{kKC_o}{1 + KC_o} \qquad 2.32$$

Where, **r** is the initial reaction rate, ***k*** the reaction rate constant, **K** the adsorption constant of substrate on the photocatalyst, and $\mathbf{C_o}$ is the initial concentration of substrate.

2.6.8 Charge Recombination

Recombination of photogenerated charge carriers is the major limitation in semiconductor photocatalysis as it reduces the overall quantum efficiency (Nishimoto, *et al* 1983). When recombination occurs, the excited electron reverts to the valence band without reacting with adsorbed species non-radiatively or radiatively, dissipating the energy as light or heat.

Recombination may occur either on the surface or in the bulk and is in general facilitated by impurities, defects, or all factors which introduce bulk or surface imperfections into the crystal. Serpone *et al.* (1995) found that trapping excited electrons as Ti^{3+} species for example, occurred on a time scale of ~ 30 ps and that about 90 % or more of the photogenerated electrons recombine within 10 ns (Nakabayashi, *et al* 1983). Doping with ions, heterojunction coupling and nanosized crystals (Ohtani, 2011) have all been reported to promote separation of the electron-hole pair, reducing recombination and therefore improve the photocatalytic activity. For example, the TiO_2 crystallites of Evonik (Degussa) P25 contain a combination of anatase (~80%) and rutile (~20%). The conduction band potential of rutile is more positive than that of anatase which means that the rutile phase may act as an electron sink for photogenerated electrons from the conduction band of the anatase phase (Ibid).

Many researchers attribute the high photocatalytic activity of this preparation to the intimate contact between two phases, enhancing separation of photogenerated electrons and holes, and resulting in reduced recombination.

2.7 METHODS OF IMPROVING THE ACTIVITY OF A PHOTOCATALYST

2.7.1 Sensitization

Dye photosensitization has been reported by different groups and to be one of the most effective ways to extend the photoresponse of photocatalysts into the visible region (Ohtani, 2011).

Indeed these types of reactions are exploited in the well known dye sensitized solar cells (O'Regan and Gratzel, 1991). The mechanism of the dye sensitized photo-degradation of pollutants is based on the absorption of visible light for exciting an electron from the highest occupied molecular orbital (HOMO) to the lowest unoccupied molecular orbital (LUMO) of a dye. The excited dye molecule subsequently transfers electrons into the conduction band of the photocatalysts, while the dye itself is converted to its cationic radical (Jina, 2010). The photocatalysts acts only as a mediator for transferring electrons from the sensitizer to the substrate on the photocatalysts surface as electron acceptors, and the valence band of the photocatalysts remains unaffected. In this process, the LUMO of the dye molecules should be more negative than the conduction band of the photocatalysts. The injected electrons hop over quickly to the surface of titania where they are scavenged by molecular oxygen to form superoxide radical $O_2^{\bullet-}$ and hydrogen peroxide radical ^{-}OOH. These reactive species can also disproportionate to give hydroxyl radical (Chen and Mao, 2007).

In addition to the mentioned species, singlet oxygen may also be formed under certain experimental conditions. Oxygen has two singlet excited states above the triplet ground ones. Such relatively long live oxygen species may be produced by quenching of the excited state of the photosensitizer by oxygen. The subsequent radical chain reactions can lead to the degradation of the dye (Ohtani, 2011).

Knowledge of interfacial electron transfer between semiconductor and molecular adsorbates is of fundamental interest and essential for applications of these materials. Ultrafast electron injection has been reported for many dye-sensitized photocatalysts systems. This injection depends on the nature of the sensitizer, the semiconductor, and their interaction. Asbury *et al* () observed very different electron injection times from *femto* to *pico* second by changing the semiconductor under the same conditions.

2.7.2 Doping

Since the discovery of visible light-induced activity of nitrogen-containing titania particles by Asahi *et a,* (2001) "doping" has been a keyword for fabrication of visible light-sensitive photocatalysts; any photocatalysts with poor visible-light activity can be modified with metal or non-metal elements to be active under visible-light irradiation. There seems to be two reasons for the explosive growth in the number of papers on doped material. One might be a lack of methodology to prove visible light-induced photocatalysis. Another reason is an unclear definition of the term "doping". The meaning of "doping" is incorporation of atoms or ions in a crystalline lattice, i.e., modification of the bulk structure of crystallites, but not modification of surfaces (Suresh, 2012). However, such location of hetero atoms or ions has been negligibly discussed.

If an adequate analytical method(s), if any, is (are) employed, average density of hetero atoms/ions can be determined, and if mapping of elements can be performed with higher sensitivity, spatial distribution may be elucidated. The effect of doping must be discussed on the basis of this structural information, though there have been few reports containing such discussion so far. In relation to this problem, recent papers have claimed that heptazine derivatives are produced on the surface of titania particles in the procedure for nitrogen doping using urea as a nitrogen source and that they work as a photosensitizer and/or photocatalyst (Ohtani, 2011) i.e., nitrogen is not "doped" in the titania lattice but is included as a surface modifier.

Even if introduced hetero atoms/ions are not "doped" in the lattice, it is useful to prepare modified photocatalysts with visible-light absorption by introducing hetero atoms/ions. One problem, however, is that newly appearing visible-light photoabsorption and photoinduced

reaction rate under visible-light photoirradiation are often described in papers. The use of organic dyes for a photoinduced degradation test is inappropriate because those dyes might be adsorbed and work as visible-light photosensitizers, and it is preferable to show resemblance of absorption (diffuse reflection) and actions spectra, i.e., photocatalysis by doped (modified) photocatalysts can be proved through action spectrum analysis.

2.8 THERMODYNAMICS OF PHOTOCATALYSIS

Although there are various definitions for the term "photocatalysis", in order to save space, "photocatalysis" or "photocatalytic reaction" can be defined as a chemical reaction induced by photoabsorption of a solid material, or "photocatalyst", which remains unchanged during the reaction. In other words, the solid acts catalytically (without change) under light and this explanation may be consistent with most definitions. "Photocatalysis" is the conceptual name for photocatalytic reactions (Suresh, 2012). From this understanding, basic data can be obtained by measuring the consumption of the starting materials and/or reaction products initiated by photoirradiation and then examining whether the photocatalyst or its properties have been modified during the reaction. This seems to be a relatively easy procedure. However, various problems are, in fact, encountered when trying to prove a given phenomenon as being photocatalytic.

The most significant difference, between photocatalysis and catalysis lies in their thermodynamics. In a general definition, a catalyst reduces activation energy of chemical reaction by changing the intermediate states and thereby accelerates the reaction which proceeds spontaneously with negative Gibbs energy change, i.e., catalysis is limited to thermodynamically possible reactions ($\Delta G < 0$, e.g., oxidative decomposition of organic compounds under aerated conditions). On the other hand, it is well known that photocatalysis can drive energy-storing

reactions ($\Delta G > 0$), e.g., splitting water into hydrogen and oxygen, as has been reported (Ohtani, 2011). In this sense, "photocatalysis" must be recognized as a concept completely different from that of "catalysis". Actually, apparent activation energy of photocatalysis estimated by an Arrhenius plot has been reported to be very small compared with that of catalytic reactions.

The principle of photocatalysis is often explained schematically as shown in **Fig. 2.2.** An electron in an electron-filled valence band (VB) is excited by photoirradiation to a vacant conduction band (CB), which is separated by a forbidden band, a band gap, from the VB, leaving a positive hole in the VB.

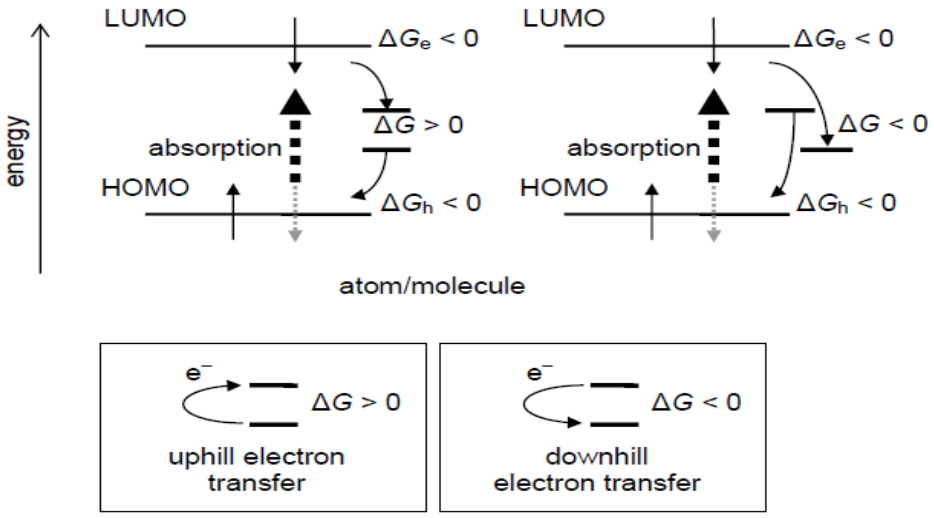

Figure 2.2: Gibbs-energy change in photocatalytic reactions by a photocatalyst of a molecule or a highly dispersed compound (Ohtani, 2011).

These electrons and positive holes drive reduction and oxidation, respectively, of compounds adsorbed on the surface of a photocatalyst. Such an interpretation accounts for the photocatalytic reactions of semiconducting and insulating materials absorbing photons by the bulk of materials. In the definition given above, however, no such limitation based on the electronic structure of a photocatalyst is included. For example, isolated chemical species not having the above-mentioned band structure on or in a solid can be a photocatalyst (Fig. 2.2), and even when a bulk material is used, the photoabsorption and resultant photocatalytic reaction may proceed at a

localized site when, for example, photocatalysts are photoirradiated at a wavelength near the band gap. Therefore, the interpretation using a band model is not always adequate for understanding photocatalysis. In this sense, the term "heterogeneous photocatalytic reaction (photocatalysis)" seems better than "semiconductor photocatalytic reaction" based on the electronic band structure.

2.9 SYNERGETIC EFFECT OF PHOTOCATALYST

The term "synergetic effect" in photocatalysis could be defined as follows: when more than two kinds of photocatalysts are used as a mixture, the overall photocatalytic activity exceeds the sum of activities of each photocatalyst (Ohtani, 2011). When a certain component alone is not a photocatalyst, and its mixture with a photocatalyst shows improved activity, that component is said to be a "co-catalyst" or "enhancer", and the improvement cannot be attributed to a synergetic effect. One of the representative discussions on the synergetic effect is for anatase-rutile mixed crystalline photocatalysts, such as Degussa P25, a commercial photocatalyst. The co-presence of anatase and rutile crystallites induces a high level of photocatalytic activity; transfer of photoexcited electrons and positive holes between interconnecting anatase and rutile particles may enhance charge separation and hence improve the efficiency of utilization of electron-hole pairs. However, there have been no reports showing direct evidence of such inter-particle charge migrations and the expected lower level of activity of pure anatase or rutile particles alone. In a scientific sense, isolation of anatase and rutile crystallites from P25 is necessary to determine the crystalline composition and to check the synergetic effect of anatase and rutile, since a synergetic effect can be proved only by showing better photocatalytic activity for a mixture of components. Ohno et al (1999) reported that in a certain photocatalytic system, commercial anatase and rutile powders exhibit a synergetic effect. The synergetic effect has not yet been proved for P25, and the effect seems to be speculation. This is natural considering that each component, anatase and

rutile, in P25 had not been isolated before the work of isolation of anatase (Ohtani, 2011). Even if all of the components are isolated from the mixture, how can the synergetic effectbe explained? Taking into consideration the fact that a photocatalytic reaction proceeds by photoabsorption of the photocatalysts and the fact that total number of absorbed photons is not directly proportional to mass (volume) of the photocatalyst, a control experiment using each component should be carried out with adjustment to make the flux of absorbed photons the same as that for the mixture. However, discussion is still needed to establish a method to clarify the synergetic effect in photocatalysis.

2.10 PARTICLE SIZE OF PHOTOCATALYST

Particle size of a photocatalyst is often evaluated by Scherer's equation using data of powder X-ray diffraction pattern (XRD). Scherer's equation is given by

$$L=\frac{k\lambda}{\beta cos\theta}. \qquad 2.33$$

Where *k* is the shape factor of the particle (k=0.98), λ is the X-ray wavelength, β is the half-maximum peak width and θ is the Bragg diffraction angle (Zhao, et al, 2012). Since *k* has been introduced in the derivation of this equation to be 0.891, *K* has its effective digits. The effective digits of the resulting size of particle *L* should be one if "0.9" is used for *k*. In order to show the size *L* with three-digit accuracy, a value of "0.891" should be used. Another point to be noted is the correction of full width at half maximum (FWHM). Two kinds of correction are required. One is correction for broadening due to Kα2 radiation, and the other is for broadening due to the optical path in the diffractometer. Generally speaking, the former and the latter corrections are made by assuming a radiation intensity ratio of Kα1 and Kα2 and by using FWHM of a standard large crystalline sample. There are at least three ways for the latter correction, but there seems to have been no discussion on the best way. The simplest way, subtraction of FWHM of the

standard, has often been employed. Both corrections appreciably affect the size of particles; a large error is expected without such corrections. Therefore, when the size of particles is demonstrated, the methods used for FWHM corrections should be described.

As described above, the size of particles in the direction vertical to the corresponding lattice plane can be estimated using Scherer's equation. In comparison with the data obtained in another way, e.g., transmission or scanning electron microscopy, difference due to this may be observed. Furthermore, broadening of FWHM of XRD peaks is also induced by distortion of the crystalline lattice. In other words, Scherer's equation neglects the effect of crystal lattice distortion (Ohtani, 2011).

Another topic related to particle size of a photocatalyst is "quantum-size effect". This frequently used term means that when the size (radius) of solid particles becomes smaller than their Bohr radius, the bottom of the conduction band and the top of the valence band shift in negative (high electronic energy) and positive (low electronic energy) directions, respectively, resulting in expansion of the band gap. The Bohr radius for anatase particles and that for rutile particles have been estimated to be 2.5 and 0.3 nm, respectively (Ohtani, 2011). Preparation of crystalline titania particles of such small size seems to be difficult, and titania particles claimed in papers to show a quantum-size effect might be larger than these sizes. A blue (shorter wavelength) shift, if observed, of the absorption edge of those samples might be due to the amorphous part of titania, not to the quantum-size effect. At least for a titania photocatalyst, use of quantum-size effect for interpreting the results seems inappropriate.

2.11 KINETICS OF PHOTOCATALYSIS

2.11.1 First Order Kinetics

It is well known that first-order kinetics is commonly observed for reactions occurring in homogeneous phases, i.e., reactions in homogeneous solutions or in gas phase. Ideally, the rate of a monomolecular reaction obeys a first-order rate expression that is explained by that proportion (number) of molecules having kinetic energy larger than the activation energy is determined only by temperature of the reaction, and that the actual number of molecules with energy for activation is proportional to the concentration (or pressure) of molecules. For these reactions, kinetic data are analyzed by plotting the logarithm of concentration of a substrate or a product against time of the reaction (Suresh, 2012) to obtain a linear line, and absolute value of the slope of the line is a rate constant, *k*. The rate (*r*) of consumption of a substrate (A) is shown by equation 2.34

$$r = -\frac{d[A]}{dt} = k[\mathrm{A}] \,. \qquad 2.34$$

On the other hand, kinetics of reactions occurring on a solid surface, i.e., catalysis or photocatalysis, must be significantly different. There are two representative extreme cases. One is the so-called "*diffusion controlled*" process, in which surface reactions and the following detachment process occur very rapidly to give a negligible surface concentration of adsorbed molecules, and the overall rate coincides with the rate of adsorption of substrate molecules. In this case, the overall rate is proportional to concentration of the substrate in a solution or gas phase (bulk), i.e., first-order kinetics is observed (Ohtani, 2011). The other extreme case is the so-called "*surface-reaction limited*" process; in which surface adsorption is kept in equilibrium during the reaction and the overall rate coincides with the rate of reaction occurring on the surface, i.e., reaction of e^- and h^+ with surface-adsorbed substrate. Under these conditions, the overall rate is not proportional to concentration of the substrate in the bulk unless the adsorption

isotherm obeys a Henry-type equation, in which the amount of adsorption is proportional to concentration in the bulk. In the former case, the rate of photocatalytic reaction obeys the first-order rate law, but this is only formal and does not mean the mechanism of monomolecular reaction with activation energy.

One of the most significant points that we must consider in scientific studies, not limited to studies on photocatalysis, is discrimination of "evidence" and "consistency". In other words, it is necessary to recognize every fact to be a "necessary condition" but not a "sufficient condition" in a strict scientific sense. For example, the fact that reaction rate obeys the first-order rate law giving a linear relation in a plot of datais only a necessary condition for a monomolecular reaction in homogeneous phase and also a necessary condition for heterogeneous photocatalytic reaction in diffusion-limited conditions or that in surface-reaction limited conditions with a Henry-type adsorption or a Langmuir-type adsorption in the lower concentration region.

2.11.2 Langmuir-Hinshelwood Kinetics

The term "Langmuir–Hinshelwood mechanism" has often been used in discussion of the mechanism of photocatalytic reaction in suspension systems, but, there has been no definition given for the Langmuir–Hinshelwood (L–H) mechanism in photocatalytic reactions. In most cases, authors have claimed that a photocatalytic reaction proceeds via the L-H mechanism when a linear reciprocal relation is observed between the reaction rate and the concentration of reaction substrate in a solution (Ohtani, 2011). These experimental results seem to be consistent with equation 2.35:

$$r = \frac{kSKC}{KC+1}. \qquad 2.35$$

where *r*, *k*, *K*, *S* and *C* are rate of the reaction, rate constant of the reaction of the surface-

adsorbed substrate with e^- (h^+), adsorption equilibrium constant, limiting amount of surface adsorption and concentration of substrate in the bulk at equilibrium, respectively, when the substrate is absorbed by a photocatalyst obeying a Langmuir isotherm and the adsorption equilibrium is maintained during the photocatalytic reaction, i.e., the rate of adsorption is faster than that of the reaction with electrons or holes. Such a situation is often called "light-intensity limited" conditions, i.e., photoabsorption is the rate-determining step (Murat, 2011). Several methods for linearization of **equation 2.35** have been reported, but two kinds of plots are often employed for analysis. As shown in **Fig. 2.3**, the most popular one is a plot of reciprocal rate against reciprocal concentration, and another one is a plot of ratio of concentration to rate against concentration. Both plots give ideally the same values of parameters, *k* and *K*, while the former plot reflects mainly lower-concentration data with probable relatively large experimental error.

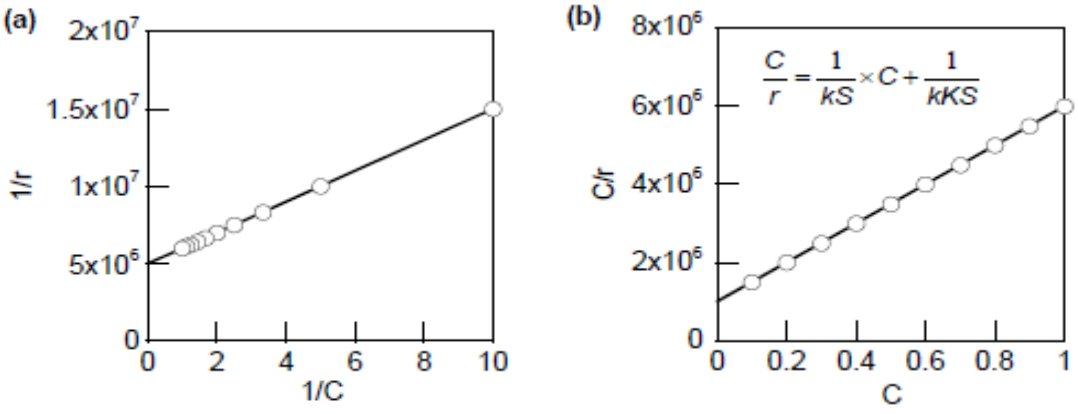

Figure 2.3: Simulation of linearized plots for kinetics governed by surfscae concentration of substrates adsorbed on the photocatalyst surface in a Langmuirian fashion (Ohtani, 2011).

The original meaning of the term "Langmuir–Hinshelwood mechanism" in the field of catalysis is presumably, a reaction of two kinds of molecules proceeding on a surface in which both molecules are adsorbed at the same surface adsorption sites with the surface reaction being the rate-determining step (in the original meaning of "rate-determining step"). Of course, the general

rate equation for the L-H mechanism (not shown here) includes two sets of parameters for two kinds of molecules, and when one set of parameters is neglected, the equation is for a monomolecular reaction, similar to the photocatalytic reaction of a substrate adsorbed in Langmuirian fashion (Ohtani, 2011). However, at least in the field of catalysis, the term L–H mechanism is rarely used for such monomolecular surface reactions, since the L–H mechanism has been discussed for a bimolecular surface reaction by comparing with the Rideal-Eley mechanism, in which a surface-adsorbed molecule reacts with a molecule coming from the bulk (outside).

Even if the L–H mechanism is defined as the reaction of a surface-adsorbed substrate obeying a Langmuir isotherm governing the overall rate, the frequently reported experimental evidence, a reciprocal linear relation between concentration of the substrate in solution and rate of photocatalytic reaction, is not always proof of this mechanism. From the linear plot, two parameters are calculated. One (often shown as "*k*", not as "*kS*") is a limiting rate of the reaction at the infinite concentration giving maximum adsorption, i.e., *kS*, and the other is the adsorption equilibrium constant, *K*. The former parameter is a product of rate constant and adsorption capacity of a photocatalyst and this may be a photocatalytic activity. The latter parameter shows the strength of adsorption and must be the same as that estimated from an adsorption isotherm measured in the dark. If kinetically obtained *K* is different from that obtained in dark adsorption measurement, the L-H mechanism cannot be adopted (Othani, *et al* 2010). Therefore, dark adsorption measurement is always required. Finally, it should be noted also in this case that a linear relation fitting to a Langmuir-type adsorption isotherm and similarity of adsorption equilibrium constants estimated using photocatalytic reaction rate and by dark adsorption experiments are only required conditions; the observed reaction rate is "consistent" with kinetics of a substrate undergoing Langmuir-type adsorption and does not exclude the possibility of other

reaction kinetics.

2.11.3 Rate Determining Step

Assuming that a certain reaction proceeds through a series of steps without any branching reactions, the rate may be the same as the rate of the slowest step, the rate-determining step, i.e., the overall activation energy is that of the rate-determining step. This original definition cannot be directly applied to photocatalysis. A plausible reason is that reactions by photoexcited electrons and positive holes occur in parallel, not in series (Ohtani, 2011).

Considering the requirement of photocatalysis for the same numbers of electrons and positive holes to be used, it seems possible to compare the rates of electron and positive-hole reactions.

However, it seems that overall reaction rate must also be influenced by the rate of recombination of e^- h^+ included in the process. In ordinary photochemistry in homogeneous phase, steady (stationary)-state approximation is used to analyze kinetics, (Ohtani, et al 2010) assuming a forward reaction to give products and a backward reaction, i.e., deexcitation. In such analyses, there may not be a rate-determining step.

On the other hand, it seems reasonable to consider that, under limited reaction conditions, non-chemical processes, i.e., physical processes, may govern the overall rate of photocatalytic reactions. Two possible representative examples are as follows. In the case in which a surface reaction of adsorbed substrates with photoexcited electrons and positive holes is much faster than adsorption from a solution or gas phase, the reaction rate should be the same as that of diffusion of the substrate, i.e., a diffusion-controlled process (assuming a very thin diffusion layer on the surface of a photocatalyst, the rate of diffusion may be proportional to surface area of the photocatalyst). Another example is a light intensity-controlled process. If surface reactions by photoexcited electrons and positive holes proceeds slower than the adsorption of substrates, the

surface concentration is always in equilibrium, and the overall rate should be the same as the rate of surface reaction, which is ideally proportional to the light intensity, a "light-intensity limited" process (Ohtani, 2011).

2.12 PHOTOCATALYTIC DEGRADATION KINETICS OF METHYL ORANGE

In most cases, authors have claimed that a photocatalytic reaction proceeds via the "Langmuir–Hinshelwood mechanism" when a linear reciprocal relation is observed between the reaction rate and the concentration of reaction substrate in a solution. The rate varied as a function of the substrate concentration according to L-H type equation as described in equation 2.36

$$-r=\frac{dc}{dt}=\frac{k_r k_e C}{1+k_e C}. \qquad 2.36$$

Where r is the oxidation rate of the reactant (mg/l.min), C is the concentration of the reactant (mg/l), t the illumination time (minutes), k_r the reaction rate constant (mg/l min), and k_e is the adsorption coefficient of the reactant (l/mg).

When the substrate concentration is very low, equation (2.36) reduces to equation 2.37

$$k_{app}C=\frac{k_r k_e C}{1+k_e C}. \qquad 2.37$$

Where k_{app} is the apparent rate constant of the reaction. Equation (2.37) can be expressed in linear form as shown in equation 2.38

$$\frac{1}{k_{app}}=\frac{1}{k_r k_e}+\frac{C}{k_r} \qquad 2.38$$

Determination of rate constant of the reaction for the surface-adsorbed substrate with e^- (h^+) pair, ***kr*** and rate constant for the adsorption equilibrium, **k*e*** would be based on **equation2.38**. The reciprocal of apparent constant, $\boldsymbol{k_{app}}$ values obtained from the plots of natural logarithm of

concentration (Ln C) against irradiation time would be plotted against initial concentration (C) to obtained ***kr*** and ***ke.***

2.13 MINERAL ORES USED AS PHOTOCATALYSTS IN THIS WORK

2.13.1 Ilmenite

Titanium dioxide is the ninth abundant element on the earth's crust (Murat, 2012). The most important mineral sources of titanium are Rutile (93-96% TiO_2), Ilmenite (44-70% TiO_2) and Leucoxene (60-90% TiO_2)

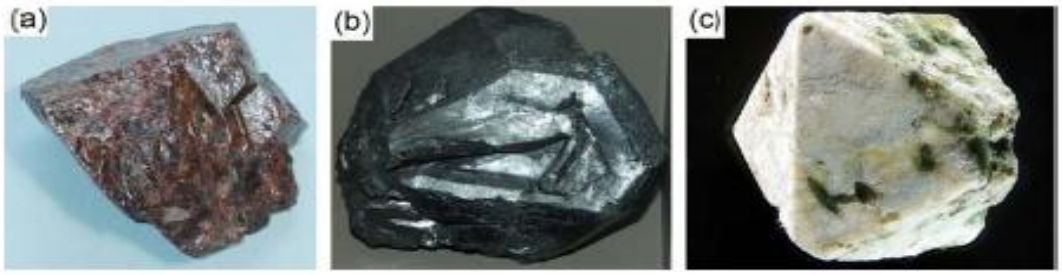

Figure 2.4: Titanium dioxide mineral (a) rutile (b) ilmenite (c) leucoxene adapted from Murat, 2012.

Titanium dioxide (TiO_2) exists as three different polymorphs; anatase, rutile and brookite (Suresh, *et al* 2012). The most stable form of TiO_2 is rutile. All three polymorphs can be readily synthesised in the laboratory and typically the metastable anatase and brookite will transform to the thermodynamically stable rutile upon calcination at temperatures exceeding ~600 °C (Hu, 2000). In all three forms, titanium (Ti^{4+}) atoms are coordinated to six oxygen (O^{2-}) atoms, forming TiO_6 octahedra (Suresh, 2012). Anatase is made up of corner (vertice) sharing octahedra which form (001) planes (Figure 2.5a) resulting in a tetragonal structure. In rutile the octahedra share edges at (001) planes to give a tetragonal structure (Figure 2.5b), and in brookite both edges and corners are shared to give an orthorhombic structure (Figure 2.5c).

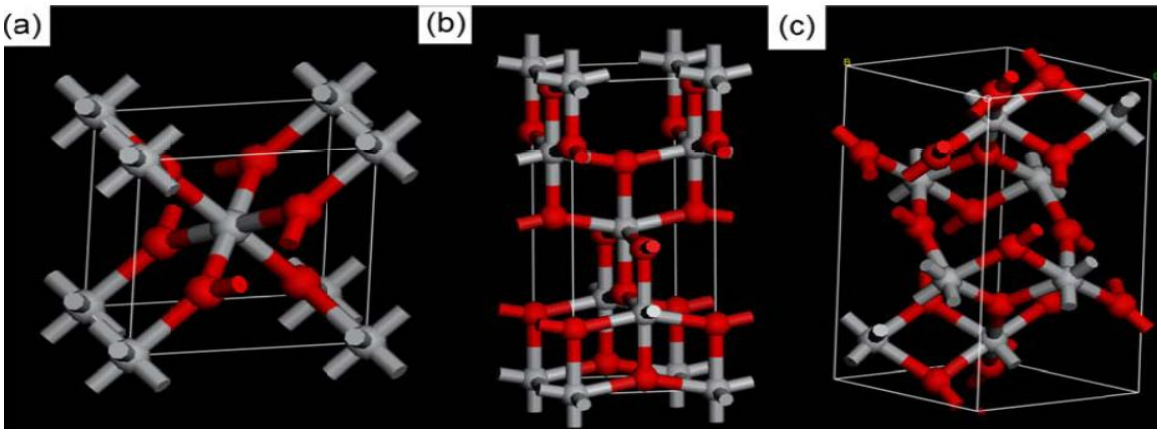

Figure 2.5: The three different phases of TiO_2, (a) Anatase (b) Rutile (c) Brookite (Kurtoglu *et al*, 2012).

Titanium dioxide is typically an *n*-type semiconductor due to oxygen deficiency (Suresh *et al*, 2012). The band gap is 3.2 eV for anatase, 3.0 eV for rutile, and ~3.2 eV for brookite, with anatase and rutile being the main polymorphs. TiO_2 is the most widely investigated photocatalyst due to high photo-activity, low cost, low toxicity and good chemical and thermal stability (Pelaez et al, 2012). In the past few decades there have been several exciting breakthroughs with respect to titanium dioxide. The first major advance was in 1972 when Fujishima and Honda reported the photoelectrochemical splitting of water using a TiO_2 anode and a Pt counter electrode. Titanium dioxide photocatalysis was first used for the remediation of environmental pollutants in 1977 when Frank and Bard reported the reduction of CN^- in water (Frank and Bard, 1977).

This led to a dramatic increase in the research in this area because of the potential for water and air purification through utilization of "free" solar energy. Other significant breakthroughs included Wang *et al.* (1977), who reported TiO_2 surfaces with excellent anti-fogging and self-cleaning abilities, attributed to the super hydrophilic properties of the photoexcited TiO_2surface and use of nano titanium dioxide in an efficient dye sensitized solar cell (DSSC) reported by Graetzel and O‟ Regan in 1991.

2.13.2 Sphalerite (Zinc Sulphide)

In photocatalysis, one of the most widely studied semiconductors is sphalerite (ZnS), because its conduction band is positioned at a much more negative potential (-1.4 V) (Li, et al, 2007) which is thermodynamically amenable for photoreduction of many organic pollutants, such as photoreductive dehalogenation of polyhalogenated benzenes and photoreductive decoloration of azo dyes (Wada, *et al* 1976).

However, with a bandgap of 3.6 eV, it is impossible for pure sphalerite to absorb visible light. This has a consequent limitation for the use of pure sphalerite as a solar light-activated catalyst, because the major fraction of solar spectrum is visible light.

Hence, extensive research was conducted to extend its optical response into the visible light region. One effective way was to incorporate a transition metal ion into the zinc lattice to alter the band structure. Previous studies indicated that the substitution of Zn^{2+} with Fe^{2+} decreased the band gap (Kudo, *et al* 2000); Ni^{2+}- or Pb^{2+}-doped ZnS exhibited high photoactivity for hydrogen evolution under visible light irradiation. Very recently, ZnS co-doped with two or more than two metal ions to form the polynary metal sulfides has been studied as a new promising class of stable photocatalysts (Chen, *et al* 1999).

Continuing efforts are being made in this field to synthesize various polynary chalcogenide semiconductors, which were not only effective in visible light but also economically feasible for large-scale application in environmental treatment (Hamadanian, *et al* 2002). It is very interesting to note that the naturally occurring sphalerite sample used in this study contains minor transition metal ions such as Fe^{2+}, Mo^{2+}, Si^{2+} and Ag^{+}. They partly substitute for Zn^{2+} to form the polynary metal sulfide. According to the reported band structure of the doped ZnS

(Tsuji, *et al* 2003), it is reasonable to infer that those transition metal ions alter the band structure of sphalerite, and probably leads to visible light-driven photocatalytic activity. More importantly, natural sphalerite exists in great quantities at the earth surface, so it is cheaper and easier to obtain than synthetic photocatalysts.

2.13.3 Wolframite (Iron-Manganese tungsten ore)

As highlighted above, the main drawback of TiO_2 is its relatively large bandgap (3.2 eV) and consequently, only a small fraction (5%) of the overall solar spectrum can be harnessed by this material. Motivated by this fact, tremendous efforts have been devoted both to sensitize TiO_2, and to find alternative semiconductors possessing similarly favorable properties, but having a narrower optical band gap. Moreover, it is generally accepted that several other parameters, which are directly related to the band structure of the materials, affect the efficiency of the photocatalyst, such as carrier transport, surface properties, chemical- and photo-stability (Janaky *et al*, 2012). A wide range of semiconductor photocatalysts have been examined among which is tungsten oxide.

Tungsten trioxide (WO_3) is an excellent photocatalyst for water oxidation (oxygen evolution), as was already demonstrated by Butler *et al*. in 1976. Furthermore, tungsten oxide shares many of the same attributes with TiO_2 in terms of chemical inertness and exceptional photo- and chemical stability in acidic to semi acidic aqueous media over a relatively wide pH range ($pH < 8$). Moreover, as pointed out very early in the history of study of this material the lower bandgap (Eg) value of WO_3 (2.7 eV vs. 3.2 eV for TiO_2) results in more substantial utilization of the solar spectrum. Since the first report, numerous studies investigated the photocatalytic properties of WO_3, however, no spontaneous hydrogen formation (high photocatalytic activity) was observed (neither under visible light nor ultraviolet (UV) light irradiation) because of its lower CB location with respect to the H^+/H_2 redox level (Anna Finlayson, 2006).

Wolframite, $(Fe,Mn)WO_4$, is an ironmanganesetungstatemineral that is the intermediate between ferberite (Fe^{2+} rich) and huebernite (Mn^{2+} rich). Along with scheelite, the wolframite series are the most important tungsten ore minerals. Wolframite is found in quartz veins and pegmatite associated with graniticintrusive. Associated minerals include cassiterite, Scheelite, bismuth, quartz, pyrite, galena, sphalerite, and arsenopyrite.

Tungsten occurs as Wolframite $(Fe,Mn)WO_4$. This wolframite occurs in closed association with cassiterite (Tin Ore) in the greisens and quartz veins found in younger Granite complexes in Nigerian deposits.

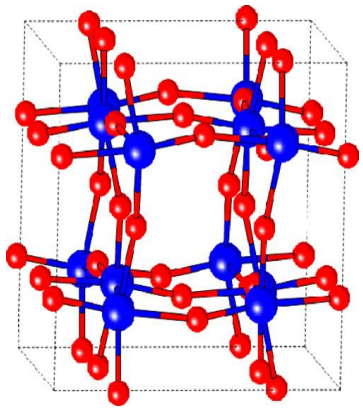

Figure 2.6: Monoclinic structure of WO_3 unit cell, where W and O atoms are represented blue and red balls, respectively (Janaky *et al*, 2012).

This mineral was historically found in Europe in Bohemia, Saxony, and Cornwall. China reportedly has the world's largest supply of tungsten ore with about 60%. Other producers are Portugal, Russia, Australia, Thailand, South Korea, Rwanda, Bolivia, the United States, and the Democratic Republic of the Congo (Cassano and Alfano, 2000).

CHAPTER THREE

MATERIALS AND METHODS

3.1 Materials

The main materials used in this work include:

1. Barkin-Ladi ilmenite obtained from National Metallurgical Development Center, Jos.
2. Abuni sphalerite obtained from National Metallurgical Development Center,, Jos.
3. Anka wolframite obtained from National Metallurgical Development Center, Jos.
4. Methyl Orange (guarantee reagent) grade
5. Hydrochloric Acid (analytical reagent) grade
6. Distilled water (obtained from Chemical Engineering, A.B.U Zaria).
7. Sodium Hydroxide pellets (guarantee reagent) grade
8. Sodium Chloride (guarantee reagent) grade
9. Hydrogen Peroxide (analytical reagent) grade

3.2 Apparatus

The apparatus used in this work are:

1. Conical flasks (250, 500ml)
2. Measuring cylinders (100ml, 200ml)
3. Plastic funnels
4. Retort stand and G-Clamp
5. Thermometer (0-360^{o}C)
6. Halogen Arc Lamps (500W), Star Gold.
7. Sieve (106 µm)
8. Plastic spoons
9. Rubber gloves
10. Nose masks
11. Syringe (20ml)
12. 90 Sample bottles (glass and plastic)

13. 1 Burette (50ml)
14. 1 Pipette (25ml)

3.3 Equipment

The major equipment employed in this work are:

1. Electronic Weighting scale (0-600g), China from Hyde Memorial Secondary School, Jengre.
2. Expose Element Furnace (30-3000^{o}C), Nabertherm GmbH Germany from Chemical Engineering A.B.U, Zaria.
3. Digital pH meter from Biochemistry Department, A.B.U, Zaria.
4. X-Ray Diffraction (XRD) Machine, PANalytical, England from National Geological Research Laboratory (NGRL), Barnawa, Kaduna
5. X-Ray Florescence (XRF) Machine, PANalytical, England from National Geological Research Laboratory (NGRL), Barnawa, Kaduna
6. Hot Plate with Magnetic Stirrer (0-300^{o}C), Stuart, England from Chemical Engineering, A.B.U, Zaria.
7. UV-Vis Spectroscopy Equipment, JENWAY 6405 from Multi User Research Laboratory (MURL), A.B.U, Zaria.
8. Scanning Electron Microscopy (SEM) Machine, JENWAY 3510 from Chemical Engineering, A.B.U Zaria.

3.4 Experimental Procedures (Methodology)

Block diagram of the experimental procedure followed in the course of this work is as shown in figure 3.1

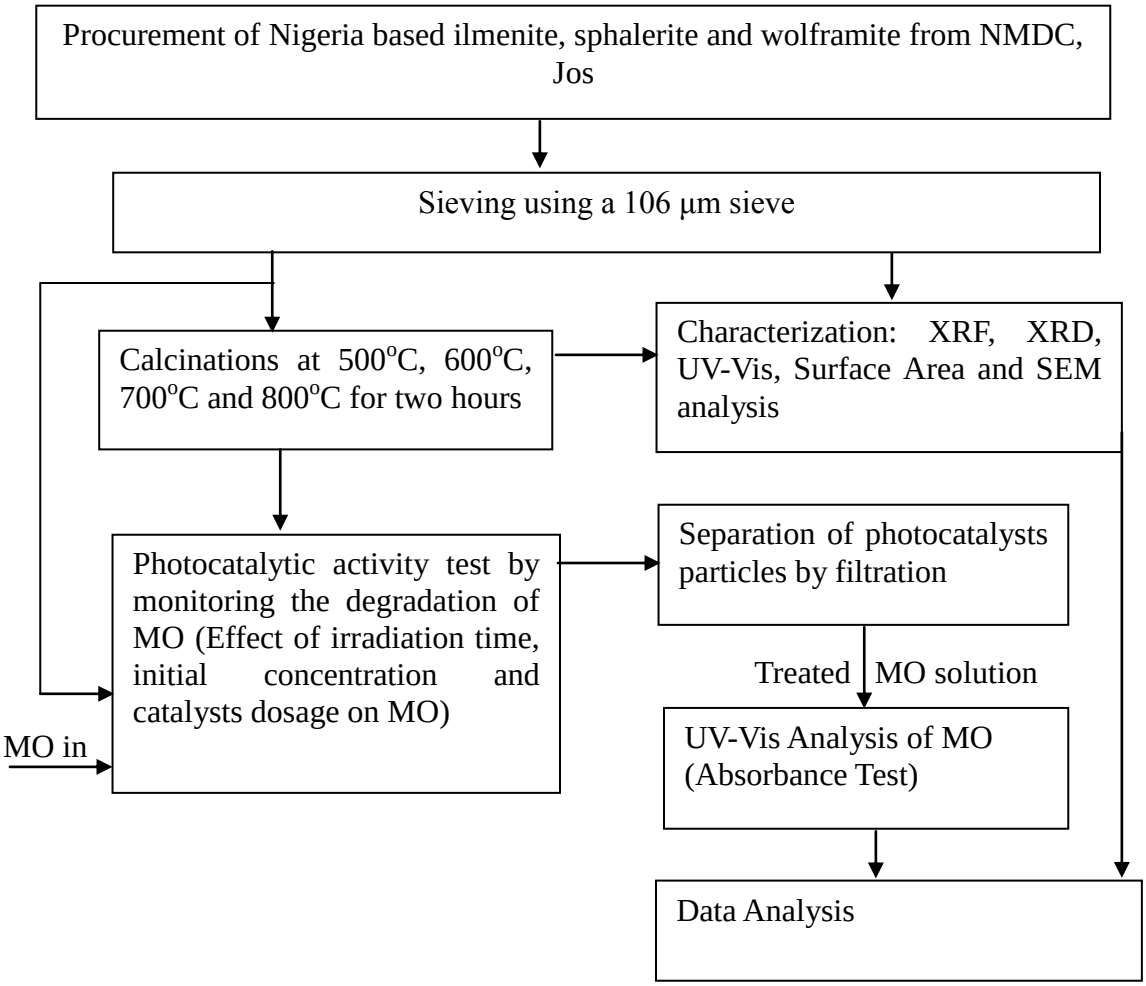

Figure 3.1: Block diagram of the experimental procedure.

3.4.1 Procurement of Samples

The raw samples were obtained from the National Metallurgical Development Centre (NMDC), Jos Plateau State, Nigeria.

3.4.2 Raw Samples Characterization

3.4.2.1 XRD Analysis

X-Ray Diffraction (XRD) patternsof the raw and calcined samples were recorded using a

PANalytical England Philips diffractometer at the National Geological Research Laboratory (NGRL), Barnawa Kaduna with a crystal monochromator at an accelerating voltage of 40kV with 100-mA flux. The X-ray source was CuKα1 with a wavelength of 1.5406Á.

3.4.2.2 XRF Analysis

Chemical composition of the raw samples was obtained XRF analysis using a PANalytical England Philips diffractometer at the National Geological Research Laboratory (NGRL), Barnawa Kaduna with a 15kV acceleration voltage and 10nA beam current.

3.4.2.3 SEM Analysis

Scanning Electron microscopy (SEM) of the raw and calcined samples for microstructures and morphologies were determined using a PHENON PRO-X machine in Chemical Engineering Department, A.B.U Zaria.

3.4.2.4 Surface area analysis using Sear's method

Specific surface area (SSA) of the raw and calcined samples was estimated according to Sear's method (Sears, 1981). A sample of the powdered photocatalyst (0.5g) was acidified with 0.1mol.dm^{-3} HCl to a pH 3-3.5. The volume was made up to 50cm^3 with distilled water after the addition of 10.0g of NaCl. The titration was carried out with standard 0.1mol.dm^{-3} NaOH to pH from 4.0, and then to pH 9.0. The volume (V) required to raise the pH from 4.0 to 9.0 was noted and the surface area computed from the following equation:

$$S\ (m^2.g^{-1}) = 32V-25. \qquad 3.1$$

Where S and V are the specific surface area in m^2g^{-1} and volume of NaOH in cm^3 respectively.

3.4.2.5 UV-Vis Spectroscopy

The UV-Vis spectra of the raw and calcined mineral ores were obtained on a JENWAY 6405

spectrophotometer at Multi User Research Laboratory (MURL) Chemistry Department, A.B.U Zaria.

3.4.3 Calcination Process

20g of each sample were placed in a crucible and calcined at 500, 600, 700 and 800^{o}C for two hours in an Expose Element Furnace (30-3000^{o}C), Nabertherm GmbH Germany, at Chemical Engineering A.B.U Zaria.

3.4.4 Photocatalytic Activity Test.

Methyl Orange (MO) was selected as a model pollutant for testing the photocatalytic activity. Photocatalytic activity of the samples was evaluated by the degradation of aqueous Methyl Orange (MO) solution. 0.2g of the photocatalyst was added to 200ml MO solution and stirred for 30 minutes in the dark to reach the absorption equilibrium, then exposed to light (500W high pressure Halogen lamp). To minimize the influence of temperature emanating from the lamp, the photoreactor was placed in a water bath. The degradation time was varied from 0 to 80 minutes at 20 minutes interval. Samples at the various degradation times were then taken and characterized with a JENWAY (6405) UV-Vis spectrophotometer in the Chemistry Department, ABU Zaria to monitor the degradation of MO molecules. The characteristic absorption peak of MO at (465nm) was chosen to monitor the photocatalytic degradation. The photocatalytic degradation efficiency was calculated using the expression

$$\text{Degradation } (\%) = \frac{C_o - C_t}{C_o} \text{ X } 100\%. \qquad 3.2$$

Where C_o is the initial concentration (mg/L) of MO, C_t is the MO concentration (mg/L) at a certain reaction time, t in minutes.

CHAPTER FOUR

RESULTS AND DISCUSSION

4.1 ILMENITE

4.1.1 Characterization of the Raw and Calcined Ilmenite Samples

4.1.1.1 Elemental Composition of Raw Ilmenite

The natural ilmenite used in this study was from Barkin-Ladi in Plateau State. The pulverized ilmenite obtained from the National Metallurgical Development Center (NMDC), Jos was sieved with a 106µm sieve. The X-Ray Florescence (XRF) result of the raw Ilmenite indicates that the main constituents are elemental titanium (69.0%) followed by iron (22.2%) as shown in Table 4.1. Ilmenite has a molecular formula $FeTiO_3$ with the percentage of titanium ranging from 44-70% (Murat, 2012).

Table 4.1: Elemental Composition of the Raw Ilmenite

Element	Concentration Wt%	Element	Concentration Wt %
Si	1.60	Zn	1.43
S	0.40	As	0.17
Ca	0.11	I	0.23
Ti	**69.00**	Eu	0.40
V	0.82	Ta	0.37
Mn	1.02	Pb	2.07
Fe	**22.20**	Bi	0.12

4.1.1.2 XRD Analysis of Ilmenite

XRD result of the raw ilmenite and ilmenite calcined at 800OC is shown in Figure 4.1. It is also important to note the XRD pattern of ilmenite calcined at 500, 600, and 700^{o}C was not considered due the correspondence in their degradation constant as shown in figure 4.2 and Table 4.3. The X-ray patterns of the raw ilmenite represented by the blue line on Figure 4.1 shows peaks at 23.8O, 32.06O, 52.99O and 68.98O which correspond to the peak angles of ilmenite (**I**) as presented by Hamadanian, (2009). However, peaks at 27.43O, 36.64O and 54.29O indicate the presence of the rutile phase **(R)**. Magnetite peak represented by **M** appear at Bragg angle of 56.8^{o}.

The XRD result of ilmenite calcined at 800OC (red line) indicates ilmenite peak only at 43.05O and the rutile peaks at 27.45O, 36.06O and 54.31O. This change in phase was due to increase in

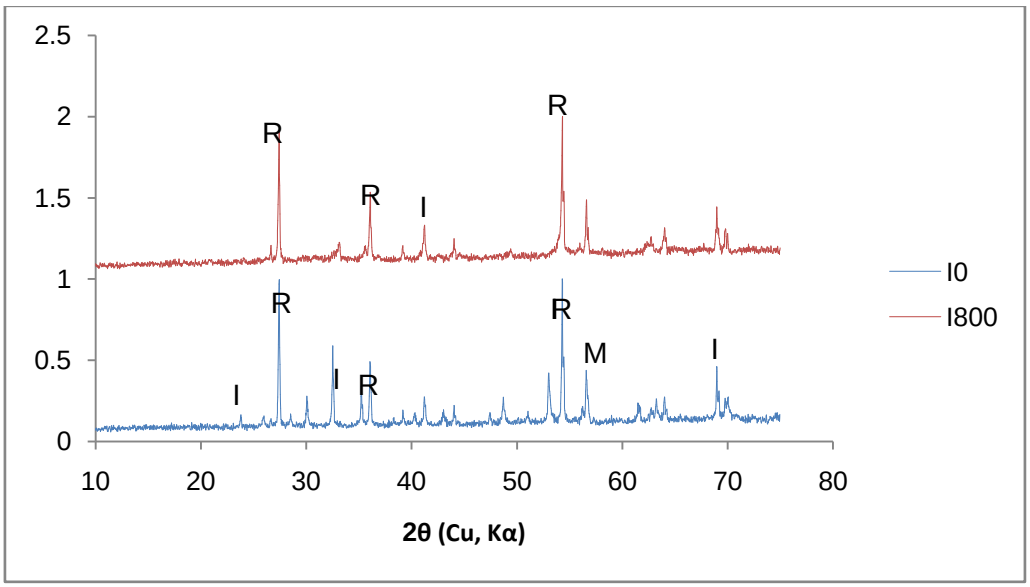

Figure 4.1: XRD patterns for raw (I0) and calcined ilmenite at 800^{o}C (I800)

the calcination temperature. Titanium dioxide generally exists in three different polymorphs: brookite, anatase and rutile (Suresh, et al, 2012). According to Pelaez, (2012), calcination of ilmenite above 600OC, the metastable brookite and anatase will transform to the thermodynamically more stable rutile.

4.1.1.3 Surface Areas and Crystal Size

Table 4.2: Surface areas and Crystal sizes for raw ilmenite, ilmenite calcined at 500, 600, 700 and 800^{o}C

Sample	Surface Area (m^2/g)	Crystal Size (nm)
I0	33.40	30.01
I500	66.92	NA
I600	66.35	NA
I700	33.30	NA
I800	24.60	43.82

The surface areas of the samples increases on calcination to 500^{o}C and 600^{o}C most likely due to opening of pores caused by the released of water and other volatile components of the raw

ilmenite. **The specific surface area decreases when the calcination temperature was raised to 700^{o}C and 800^{o}C due to increase in crystal size as evidence by the estimated crystal size of raw (I0) and calcined ilmenite at 800^{o}C (I800).**

4.1.2 Photocatalytic Activity of the Raw and Calcined Ilmenite Samples

Photocatalytic activity of raw ilmenite (I0), Ilmenite calcined at 500OC (I500), 600OC (I600), 700OC (I700) and 800OC (I800) was investigated. This test was carried out by monitoring the photocatalytic degradation of methyl orange (MO) irradiated with a 500W halogen lamp at various irradiation times shown in Figure 4.2. The apparent rate constant k_{app} (which was assumed to follow pseudo first-order kinetics at low concentration) was determined. It was observed that calcinations at 500^{o}C exhibit a better rate constant of 1.3x10-3 min-1. However, there was no considerable difference in the rate constant from raw ilmenite to ilmenite calcined at 700^{o}C. This was attributed to their comparable surface areas and low crystalinity as well as the presence of anatase phase.

Calcination at 800^{o}C gave a low activity of 0.99x10^{-3} (min^{-1}) as shown in Table 4.3. The low activity of I800 can be attributed to the complete transformation of ilmenite to the rutile phase, and increase in the crystal size with a corresponding decrease in surface area as discuss in section 4.1.1.2.

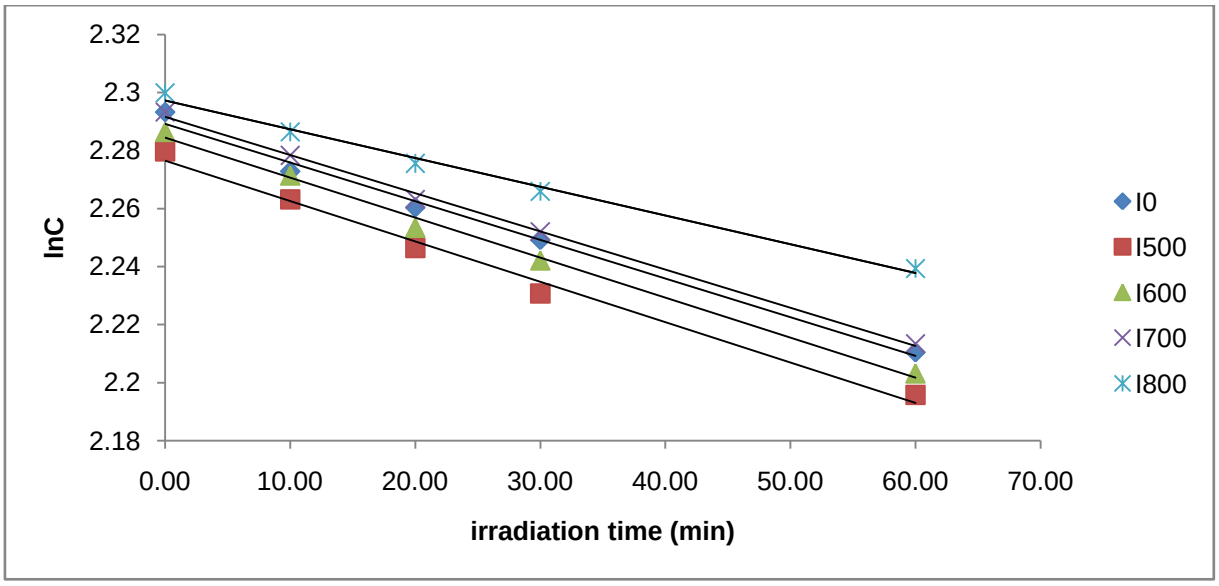

Figure 4.2: Photocatalytic degradation of MO using raw and ilmenite calcined at 500°C, 600°C, 700°C and 800°C as a function of irradiation time.

Table 4.3: Values of k_{app}(min^{-1}) and R^2 for MO degradation using ilmenite

Sample	Rate Constant, k(min^{-1})	R^2
I0	1.33	0.9916
I500	1.39	0.9905
I600	1.38	0.9952
I700	1.32	0.9979
I800	0.99	0.9922

4.1.3 Effect of Photocatalysts Dosage on the Degradation of MO

Table 4.3 shows the effect of calcined ilmenite on MO degradation. Ilmenite calcined at 500°C which gave the best activity for the degradation of MO was investigated. Figure 4.3 shows the effect of catalyst dosage on MO degradation. As shown in figure 4.3, catalyst dosage of 1.5g/200ml solution of 10mg/l MO gave the best degradation percentage of 19.07%. This is attributed to the following reasons:

At low concentration region such as 0.5g/200ml and 1.0g/200ml of TiO_2, the amount of electron-hole pair generated is low and this will lead to low degradation of MO. On the other hand, "scree ning" effect is produced when TiO_2 concentration is high (above 1.5g/200ml). The reaction rate d

iminishes due to the excessive opacity of the solution, which prevents the catalyst farthest from b eing illuminated. Also when catalysts concentration is high, after travelling a certain distance on an optical path length, turbidity impedes further penetration of light in the reactor. Another impor tant factor is the path length of the irradiated light. In this study, a path length of about 20cm was used. The percentage of photons absorbed by the suspension and the percentage of photons scatt ered by the TiO_2 particles is a very complex phenomenon that cannot be solved experimentally, b ut must be experimentally estimated.

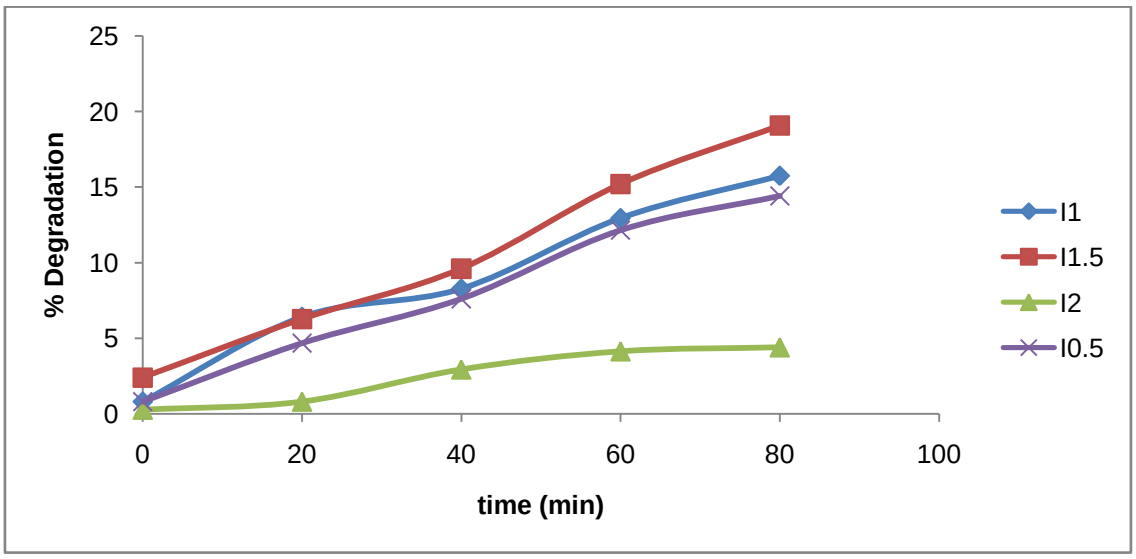

Figure 4.3: Photocatalytic degradation of MO (10mg/L) with various dosage of ilmenite calcined at 500^{o}C as a function of irradiation time.

Generally, the degradation of MO by ilmenite was low. An important reason could be that titanium dioxide exists in three phases: brookite, anatase and rutile. As shown in figure 4.1, the XRD result shows that for ilmenite ($FeTiO_3$), the rutile phase is the dominant phase which has an inherent low photocatalytic activity. Rutile has a much lower donor state compared to anatase due to its higher electron effective mass charge and therefore electron-hole recombination at the surface or the bulk of the photocatalyst is low. This lower recombination rates leads to anatase being a better photocatalyst than rutile (Tang, Prasad **et al**, 1994).

Anatase phase of titanium dioxide possesses strong hole trapping sites on the surface which result in higher lifetime of the carriers compared to rutile phase. This makes anatase a better photocatalytic material than rutile (Colbeau-Justin, Kunst **et al**, 2000).

The band gap of ilmenite may vary from 3.0-3.2eV which correspond to a wavelength of 412.5-387nm respectively and cannot absorb an appreciable fraction of solar light. The wavelength of visible light vary from 400-700nm, for this reason, ilmenite can only absorb 2.5-5% of visible light which account for its low photocatalytic activity. However, the slight increase in the activity of the calcined ilmenite at 500^{o}C (19.07% MO degradation) compared to that obtained by Lu, *et al* (2007) (7.14%) and Hamadanian, *et al* (2010) (14.28%) was ascribed to the presence of other semi-conductors photocatalysts such as Fe**2**O**3**, SiO**2** etc, which constitute a synergetic effect.

Table 4.4 gave a comparative degradation of MO by various forms of titanium dioxide as reported by different authors. As shown in the table for the same operating conditions shown under Table 4.4, the degradation of MO for the present work is higher.

Table 4.4: % degradation of MO by various forms of Titanium dioxide

Photocatalysts	(% degradation of MO)	References
Natural Rutile	7.14	Lu *et al* 2007
TiO_2	14.28	Hamadanian *et al*, 2010
Natural ilmenite	19.07	Present work

MO Conc. =10mg/L, Light source = visible, irradiated for 1hr, Photocatalyst dose=1g/L

4.1.4 Effect of Initial Substrate Concentration

To determine the effect of initial concentration of MO on the activity of ilmenite, a duration time of 80 minutes was chosen. The concentration was varied between 15, 20 and 30 mg/L of MO. The effect of these concentrations was studied on raw and calcined ilmenite at, 500OC and 800OC. It was observed that MO degradation increases with decrease in concentration of MO. This is because, for a photocatalytic reaction, substrates compete for the same number of photo-generated hole and/or

hydroxyl radical and degrade them to different compounds. Thus, the concentration of MO continuously changes as reaction progresses. Evaluation of k_r, first order reaction rate constant (mg/l.min), and k_e, the adsorption coefficient of the reactant (l/mg) was based on equations 2.38 and figure E1 in appendix E.

From the results tabulated in table 4.5, it is obvious that a higher rate constant was obtained for sample I500 (calcined at 500^{o}C), ^{kr}=0.3776 mg/l.min, there was no appreciable difference for I0 and I800 (raw and ilmenite calcined at 800^{o}C) with $^{k}_{r}$ values of 0.0866 mg/l.min and 0.0896 mg/l.min respectively. For raw ilmenite, low surface area, low porosity and the presence of recombination centers may have affected the activity of the photocatalyst. For ilmenite calcined at 800^{o}C, increase in crystal growth which leads to low surface area, and change of anatase phase to rutile phase may be the reason for the low activity. However, I500 is characterized by high surface area, low crystal size, high porosity and the presence of anatase phase must have contributed to the high rate of the degradation of MO.

Furthermore, the rate of the adsorption equilibrium constant, k_e shows a higher value for I0 (0.0262 l/mg) and I800 (0.0211 l/mg) and a relatively lower value for I500 (0.0084 l/mg). This could be due to the low surface area of I0 compared to sample (I800).

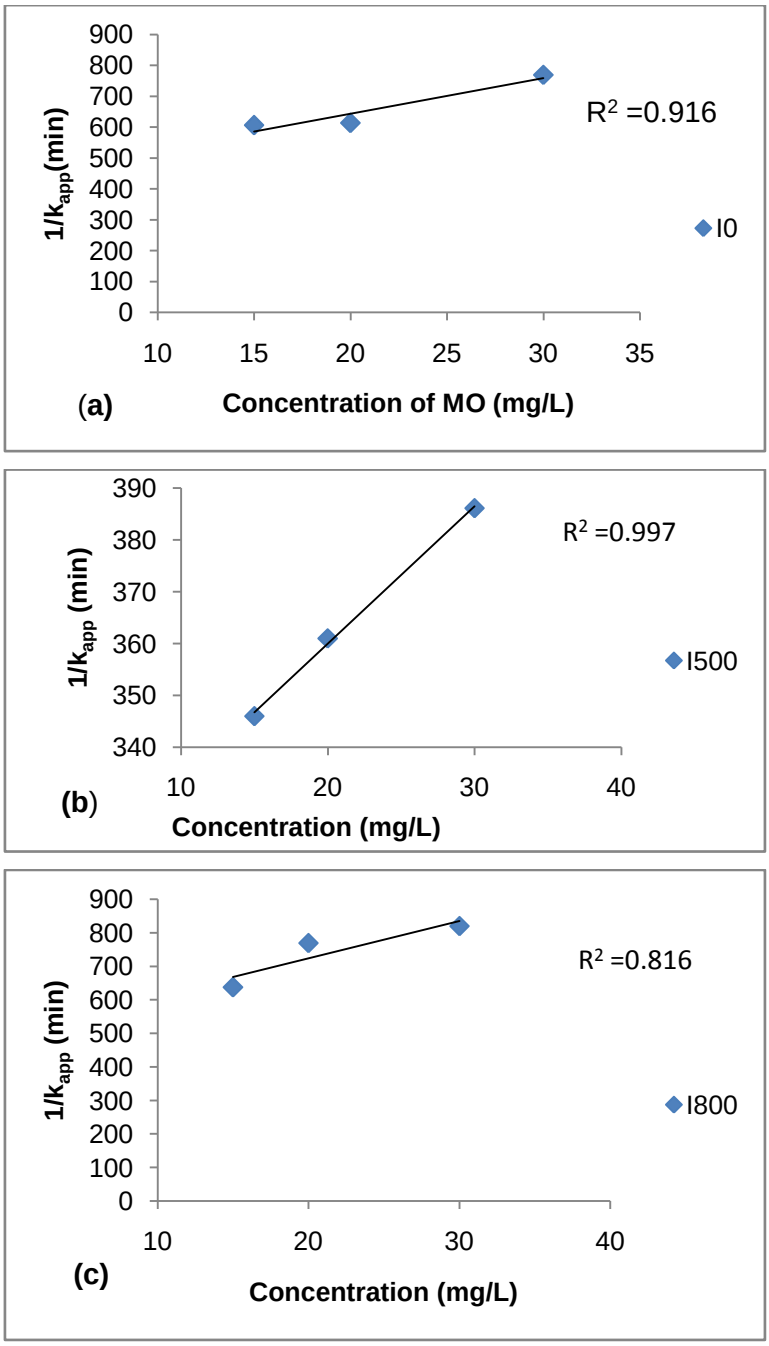

Figure 4.4: Plots of reciprocal of apparent rate constant against substrate concentration for (a) raw ilmenite (I0), (b) ilmenite calcined at 500°C (I500) and (c) ilmenite calcined 800°C (I800).

Table 4.5: Values of k_r and k_e for the various samples determined above

Samples	I0	I500	I800	S0	S600	S700	W0	W600	W800
kr(mg/l.min)	0.0866	0.3776	0.0896	0.1022	2.3474	3.5088	0.089	0.3422	0.0364
Ke {l/mg}	0.0262	0.0084	0.0211	0.0489	0.003	0.005	0.0274	0.0167	**0.25**

4.2 SPHALERITE

4.2.1 Characterization of the Raw and Calcined Sphalerite Samples

4.2.1.1 Elemental Composition of Raw Sphalerite

Table 4.6 shows the X-Ray Florescence (XRF) result of the raw sphalerite. The main constituents are elemental zinc (58.60%), sulphur (16%) and molybdenun (11%).

Table 4.6: Elemental Composition of Raw Sphalerite (ZnS)

Element	Concentration Wt %	Element	Concentration Wt%
Si	5.00	**Zn**	**58.60**
S	**16.00**	As	0.02
Ca	0.16	Y	0.47
Mn	0.02	Mo	11.00
Fe	4.85	Ag	2.60
Ni	0.03	La	0.02
Cu	0.08	Eu	0.02

Sphalerite has a molecular formula of ZnS with zinc and sulphur being the major constituents as confirmed by the XRF result. According to Yan Li, *et al* (2008), the percentage of Zn in sphalerite ranges between 50 – 64% and an appreciable percentage of molybdenum, silicon, manganese or iron.

4.2.1.2 XRD Analysis of Sphalerite

The XRD patterns of the raw and calcined sphalerite are shown in figure 4.5. ZnS was converted into ZnO and other trace oxides in a stepwise oxidation manner air furnace (equation 4.1).

$$2ZnS + O_2 \rightarrow 2ZnO + 2S \quad \ldots\ldots 4.1$$

The XRD of raw sphalerite (S0) showed peaks at 2Θ=28.5O, 47.5O and 56.3O represented by ZS which compared well with the result of S600 (calcinations at 600OC) was also well indexed to the sphalerite structure, and the only difference with S0 was that the intensity of the peaks increased, and a new peak at 34.8oappeared. This indicates that S600 has better crystallinity.

When ZnS was calcined at 700OC (S700), all the characteristics peaks of ZnS disappeared due to increase

in calcination temperature, and the XRD pattern showed a complete zinc oxide (ZnO) phase represented by ZO and F representing Fe_2O_3. S800 was also well indexed to the ZnO structure, with the exception that the intensity of the peaks increased and the half-peak width decreased as the calcinations temperature increased figure 4.5.

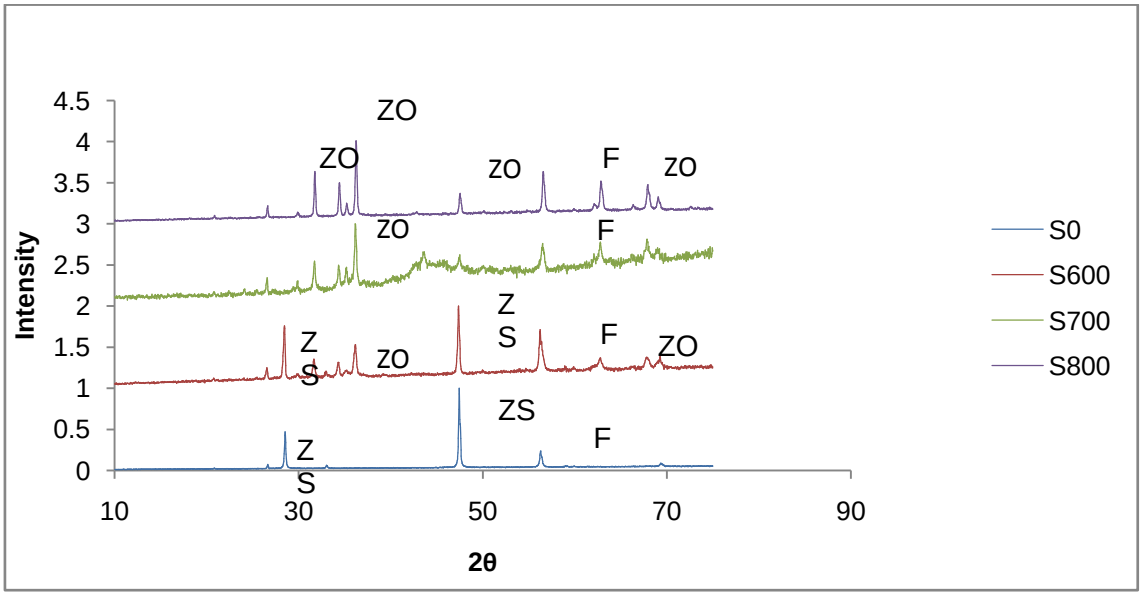

Figure 4.5: XRD patterns of raw and sphalerite calcined at 600°C, 700°C and 800°C

4.2.1.3 Surface Areas and Crystal Size

The ZnO nanoparticle size *L* (equation 2.33) was calculated via the Scherer formula (Appendix A) and the values are presented in Table 4.6. XRD peaks gave an average crystalline size of 28.293, 43.254, 19.155, 52.045 nm for S0, S600, S700 and S800, respectively. The surface area of these samples was evaluated using Sear's method and the result was summarized in Table 4.7. The values for S0, S600, S700 and S800 are 128.60, 121.84, 116.60, 152.60 and 107.80m^2/g, respectively. It was observed that the surface area decreases as calcination temperature was increase to 600°C due to growth in crystals. At 700°C, there was an increase in surface area with a corresponding decrease in crystal size due to complete oxidation of ZnS to ZnO as shown in Figure 4.5. The substituted small size oxygen replaced the sulphur which has a large Bohr radius and decreased the crystal size. As calcination was increased to 800°C, there was an increase in the crystal size and a corresponding decrease in surface area due to the elimination of

defects introduced by the substitution of oxygen in the crystal lattice of ZnS as shown in Table 4.7.

Table 4.7: Surface area and crystal size of raw sphalerite, sphalerite calcined at500, 600, 700 and 800^{o}C

Sample	Surface Area (m^2/g)	Crystal Size (nm)
S0	128.60	28.293
S500	121.84	NA
S600	116.60	43.254
S700	**152.60**	**19.155**
S800	107.80	52.045

4.2.1.4 UV-Vis Spectroscopy

Figure 4.6 shows the UV–visible light spectroscopy of the raw and calcined sphalerite at 700^{o}C. The onset of the absorption edge of the raw sphalerite sample is at 365 nm, corresponding to the band gap of 3.4 eV. This implies that the raw sphalerite sample could not utilize visible light to induce electron–hole pairs. However, the UV–vis spectroscopy of the calcined sphalerite sample shows both a steep absorption edge at about 400 nm and a broad absorption shoulder band in the vicinity of 400–600 nm. The UV–vis spectra of the calcined sphalerite sample suggest it could be a potentially good candidate in a visible light-driven photocatalytic reaction.

As is well known, the shape of the steep absorption edge revealed a band-gap transition between the valence and conduction bands in direct semiconductors (Yan Li, et al, 2008). According to Li, the adsorption shoulders indicated discontinuous energy levels formed by the defects in the forbidden band. As a result, the red shift of the steep absorption edge suggested that the intrinsic band gap of the catalyst narrowed due to the substitution of transition metal ions (Fe^{2+} and Mo^{2+}) for Zn^{2+}. Factually, as indicated by the XRF result (Table 4.6), the isomorphous substitution of Zn with Fe and Mo makes the natural sphalerite to exhibit a substantial photocatalytic activity in the visible region.

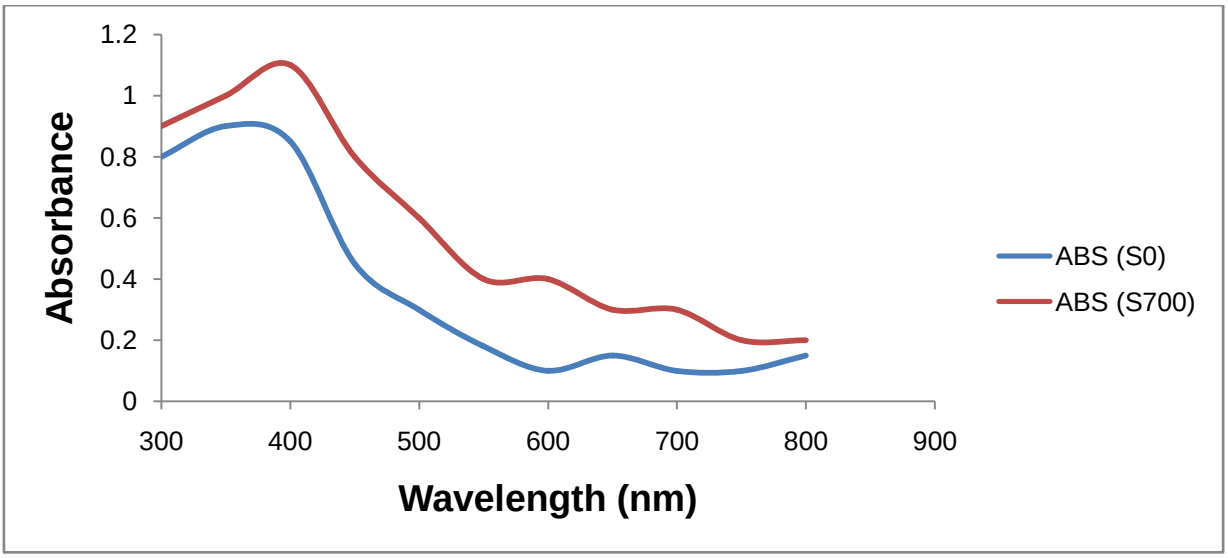

Figure 4.6: UV-Vis spectroscopy of Raw and Sphalerite Calcined at 700^{o}C

4.2.1.5 Scanning Electron Microscopy (SEM) of Raw and Calcined ZnS at 700^{o}C

Figure 4.7 shows the scanning electron microscopy (SEM) images of S0 and S700. Comparison of Figures 4.7a and 4.7b indicate that crystal size of S0 was much larger than S700, which indicates that the change in phase from ZnS to ZnO at 700^{o}C was responsible for this structural difference.

This result is in agreement with the values of the crystal sizes calculated using Sherrer equation (equation 2.33) as presented in Table 4.7.

Cleavage planes and fracture surfaces were prevalent on the surface of the natural sphalerite, which were probably produced by the mechanical grinding. Since cleavage planes and fracture surfaces are known to provide much more active sites than flat crystal faces (Zhao,et al, 2012) the reactivity of natural mineral surface is generally higher than that of its synthetic counterparts with perfect crystal faces.

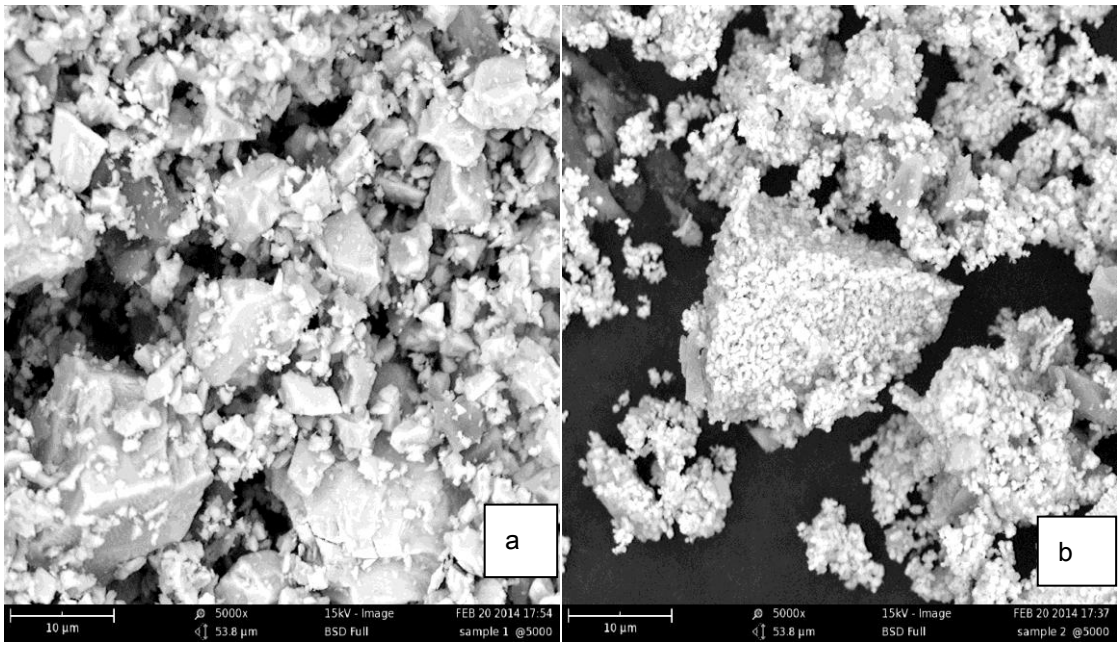

Figure 4.7: Scanning electron micrographs of raw (4.7a) and calcined sphalerite at 700^{o}C (4.7b)

4.2.2 Photocatalytic Activity of Abuni (Nasarawa State) Sphalerite (Raw and Calcined Samples)

The photocatalytic activity of the raw and calcined sphalerite was investigated by testing it on the photocatalytic degradation of MO. Figure 4.8 shows the degradation of MO as a function of irradiation time. As indicated in Table 4.8; it is clear that the apparent rate constant, k_{app} for S700 (3.58×10^{-3} min^{-1}) was higher than for S0 (1.68×10^{-3} min^{-1}), S500 (2.27×10^{-3} min^{-1}), S600 (2.86×10^{-3} min^{-1}), and S800 (2.75×10^{-3} min^{-1}). The above results indicated that pure ZnO obtained via calcinations, exhibited much better photocatalytic activity than ZnS or ZnS/ZnO in this study. The reason being that, the conduction-band electrons and valence-band holes are generated on the surface of the catalysts when they are illuminated by visible light. Holes can react with water adhering to the surface of the catalysts to form highly reactive hydroxyl radicals ($OH^{\cdot}$). Meanwhile, on the surface of the catalysts, oxygen is reduced as an electron acceptor to superoxide ($O_2^{\cdot}$), which leads to the production of $OH^{\cdot}$. These radicals have a powerful oxidation ability to degrade organic dyes such as MO. The yield of the photogenerated electron-hole pairs depend on the intensity of incident photons, with energy exceeding or equaling the catalysts band gap energy (Zhao et al, 2012). The band gap energy of ZnS is 3.7eV,

accordingly its threshold absorption wavelength is 335nm, whereas the threshold absorption wavelength of S700 (ZnO) was 388nm. The visible light used in this study emitted light at 387nm. Therefore, it may be concluded that this light was completely absorbed by S700, but only partially by ZnS. Thus S700 has better photocatalytic activity than S0, S500 S600 and S800. The high specific surface area and small crystal size of S700 was responsible for its higher photocatalytic activity than the other samples.

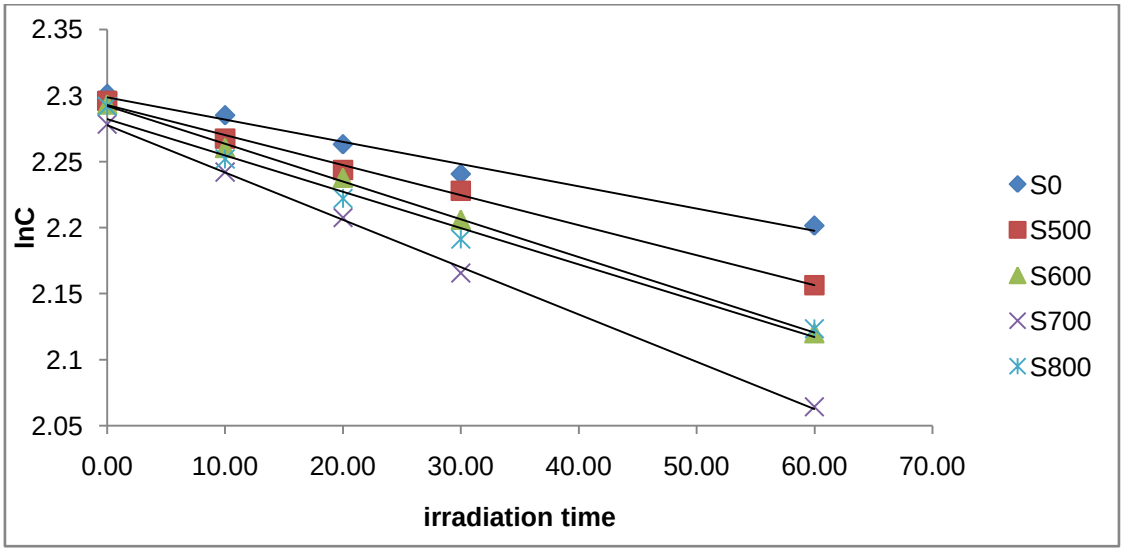

Figure 4.8: Photocatalytic degradation of MO using raw and sphalerite calcined at 500°C, 600°C, 700°C and 800°C as a function of irradiation time.

Table 4.8: Values of k_{app}(min^{-1}) and R^2 for MO degradation using sphalerite

Sample	Rate Constant, k(min^{-1})x10^{-3}	R^2
S0	1.68	0.9849
S500	2.27	0.9962
S600	2.86	0.9989
S700	**3.58**	**0.9990**
S800	2.75	0.9854

4.2.3 Effect of Photocatalysts Dosage on the Degradation of MO

Table 4.8 shows the effect of calcined sphalerite on MO degradation. Spalerite calcined at 700°C which gave the best activity for the degradation of MO was investigated. Figure 4.9 shows the effect of catalyst dosage on MO degradation. As shown in Figure 4.9, catalyst dosage of 1.0g/200ml solution of 10mg/l MO gave the best degradation percentage of 90.93%. Generally, a high degradation percentage was

observed for sphalerite samples. This is due to their low band gap (3.0-3.7eV), low crystal size, high specific surface area, high porosity, and the presence of defects which were eliminated at higher temperatures. Compare to commercial zinc oxide (ZnO), S700 was synthesized by calcination of ZnS at 700^{o}C in air. During the calcinations process, oxygen replaces sulphur in the ZnS crystal lattice, because sulphur has a larger Bohr radius than oxygen, which may introduce lattice distortion, giving rise to some new defects, such as oxygen vacancies. Therefore there were more oxygen vacancies in S700 than commercial ZnO. As for S700 and S800, the higher the calcination temperature, the more surface oxygen vacancy defects are eliminated.

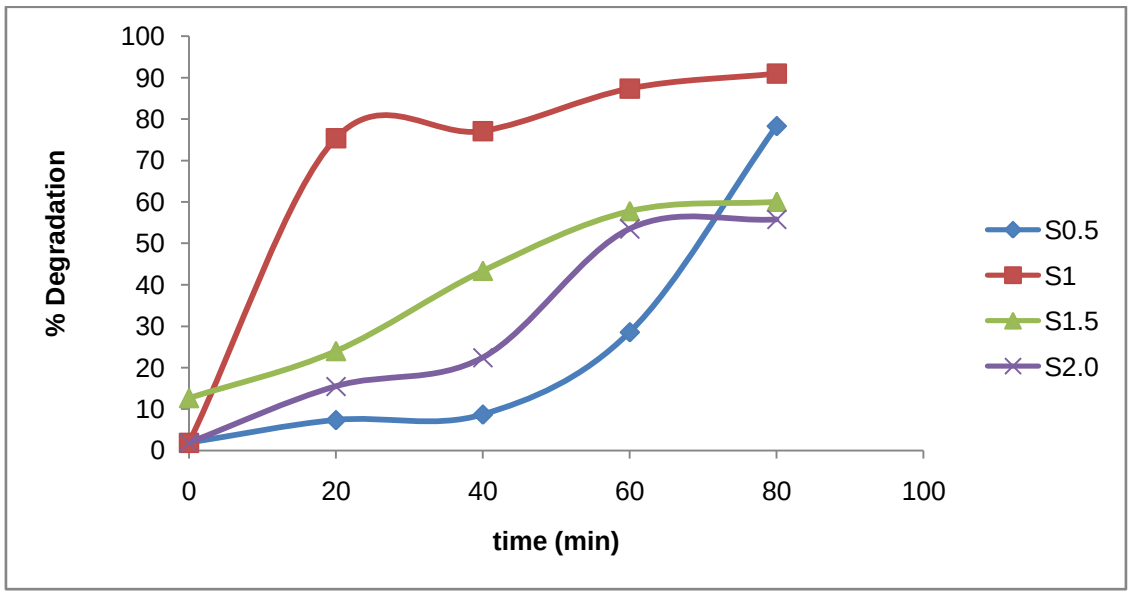

Figure 4.9: Photocatalytic degradation of MO (10mg/L) with various dosage of sphaleritecalcined at 700^{o}C as a function of irradiation time.

Figure 4.10 compares the degradation ratios obtained using zinc oxide obtained by calcination S700 (red line) and commercial ZnO (blue line) as photocatacysts. It can be seen that the degradation percentage were around 90.0% after 80minutes. However, after 20 min irradiation, the degradation was 75.0% and 43.0% for S700 and commercial ZnO respectively, suggesting that S700 had better degradation efficiency. Singto, *et al*, (2012) carried the photocatalytic degradation of MO using ZnO obtained through calcination and commercial ZnO and reported that after 20 minutes irradiation in visible light, 63% and

47% degradation of MO was achieved by synthesized ZnO through calcination and commercial ZnO respectively and 96% and 71% respectively after 40 minutes irradiation time. It can reasonably be concluded that ZnO obtained by calcination of natural sphalerite has a higher degradation percentage after 20 minutes irradiation time.

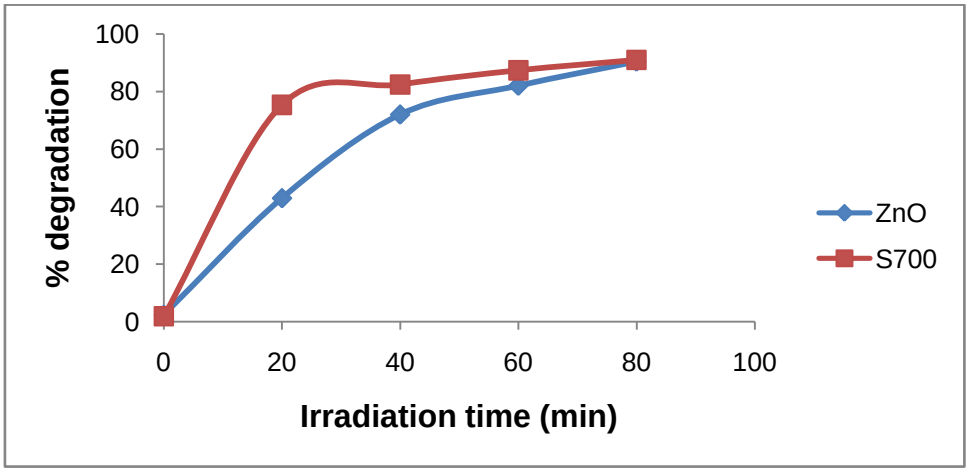

Figure 4.10: Photocatalytic degradation (%) of MO using sphalerite calcined at 700°C andcommercial zinc oxide as a function of irradiation time.

4.2.4 Effect of Initial Substrate Concentration

The effect of initial substrate concentrations was studied on raw and calcined sphalerite at, 600OC and 700OC. It was observed that MO degradation increases with decrease in concentration of MO. **From the results shown in Table 4.4, it is obvious that a higher rate constant was obtained for sample S700 (calcined at 700°C), k_r =3.5088 mg/l.min.**

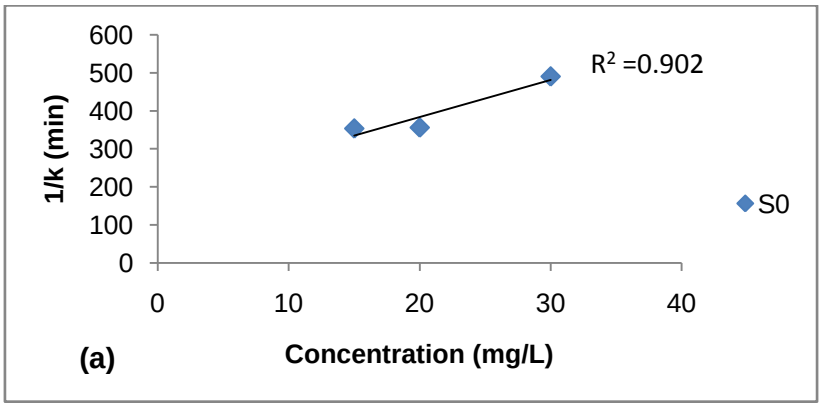

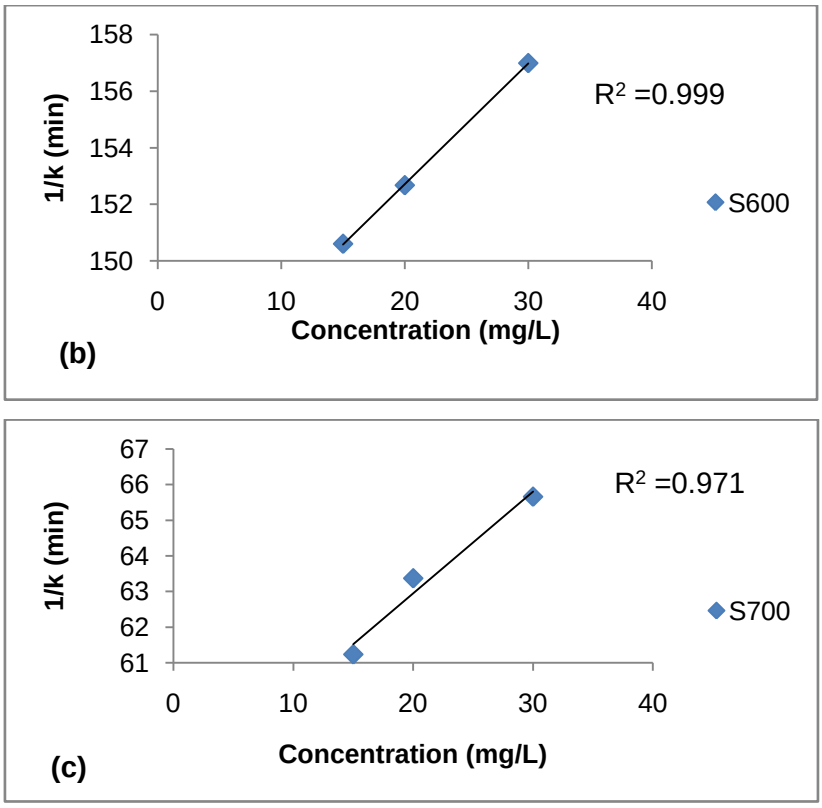

Figure 4.11: Plots of reciprocal of apparent rate constant against substrate concentration for (a) raw sphalerite (S0), (b) sphalerite calcined at 600^{o}C (S600) and (c) sphalerite calcined 700^{o}C(S700).

The k_r values of S0 and S600 were 0.1022 mg/l.min and 2.3474896 mg/l.min respectively. For raw sphalerite (S0), high band gap (3.7eV), low surface area, low porosity and the presence of recombination centers may have affected the activity of the photocatalyst. For sphalerite calcined at 600^{o}C (S600), increase in crystal growth which leads to low surface area was responsible for the low activity. However, at 700^{o}C (S700), the sample is characterized by high surface area, low crystal size, high porosity and the complete change from ZnS to ZnO, which inherently is a better photocatalyst, must have contributed to the high rate of the degradation of MO.

Furthermore, the rate of the adsorption equilibrium constant, ke **shows a higher value for S0 (0.0489 l/mg), and a relatively lower value for S700 (0.0050l/mg) and S600 (0.0030 l/mg).**

This is due to cleavage planes and fracture surfaces which were prevalent on the surface of the raw sphalerite.

4.3 WOLFRAMITE

4.3.1 Characterization of the Raw and Calcined Wolframite Samples

4.3.1.1 Elemental Composition of Raw Wolframite

The X-Ray Florescence (XRF) result of the raw wolframite indicates that the main constituents are elemental wolfram (64.45%) and iron (15.10%) as shown in table 4.9

Table 4.9: XRF Analysis of raw Wolframite

Element	Concentration Wt%	Element	Concentration Wt%
Si	0.60	Ag	2.30
Mn	0.28	Sn	4.60
Ca	2.27	La	0.01
Fe	**15.10**	Eu	0.11
Ge	0.19	Yb	0.00
Zr	3.10	**W**	**64.45**
Nb	6.10	Pb	0.97

Wolframite, $(Fe,Mn)WO_4$, is an iron-manganesetungstatemineral that is the intermediate between ferberite (Fe^{2+} rich) and huebernite (Mn^{2+} rich). Comparing the percentages of iron and manganese, it is obvious that the wolfram used in this study was ferberite. Hence, the molecular formula of this wolfram could be suggested as $FeWO_4$

4.3.1.2 XRD Analysis of Wolframite

The XRD patterns of the raw (W0) and calcined wolframite (W800) are shown in Figure 4.12. The choice for calcination at 800^{o}C was due to the comparable degradation rate constants as shown in Table 4.11.

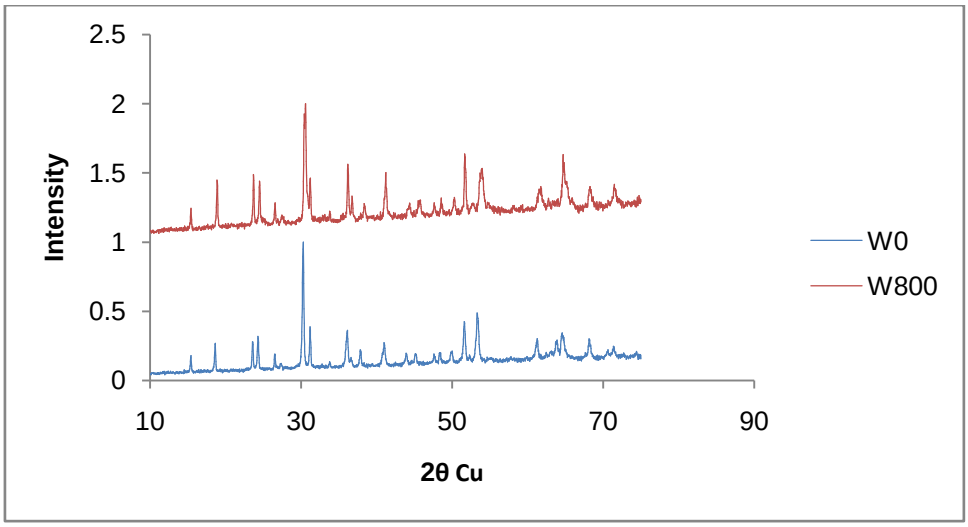

Figure 4.12: XRD patterns of raw wolframite and wolframite calcined at 800^{o}C

The major peaks observed for the raw wolframite are 18.59^{o}, 23.53^{o}, 30.39^{o}, 36.06^{o}, 43.86^{o} and 64.45^{o}. The same peaks also appear when the calcination was done at 800^{o}C. The XRD result did not show any difference in the number of peaks as calcination increases from 500^{o}C to 800^{o}C. The only observable difference is the intensity of the peaks. For raw wolfram (W0), it is seen that the intensity of the peaks is low, but as calcinations increases, there was a corresponding crystal growth and the photocatalyst became more crystalline. All the peaks were traced to that of WO_3 except those at 30.39^{o} and 36.06^{o} which traced to Fe_2O_3 and SiO_2.

4.3.1.3 Surface Areas and Crystal Size

The surface areas of the various samples were determined using Sear's method. Table 4.10 shows the specific surface area decreases from raw wolfram to that calcined at 800^{o}C due to growth in crystal size which was determined using Scherer equation. The crystal increases as calcinations temperature increases due to the elimination of oxygen vacancies and other defect sides.

Table 4.10: Surface areas of raw wolframite, wolframite calcined at 500, 600, 700 and800^{o}C

Sample	Surface Area (m^2/g)	Crystal Size (nm)
W0	89.40	35.45
W500	82.70	NA
W600	77.78	NA
W700	76.92	NA
W800	68.60	39.40

4.3.2 Photocatalytic Activity of Raw and Calcined Wolframite.

Photocatalytic activity analysis of raw wolframite (W0), and wolframite calcined at 500OC (W500), 600OC (W600), 700OC (W700) and 800OC (W800) was carried out. This was done by monitoring the photocatalytic degradation of methyl orange (MO) irradiated with a 500W halogen lamp. As shown in figure 4.13 plots, the apparent rate constant k_{app} (which was assumed to follow pseudo first-order kinetics at low concentration). It was observed that calcination at 600^{o}C gave a better rate constant of 1.92x10-3 min-1.

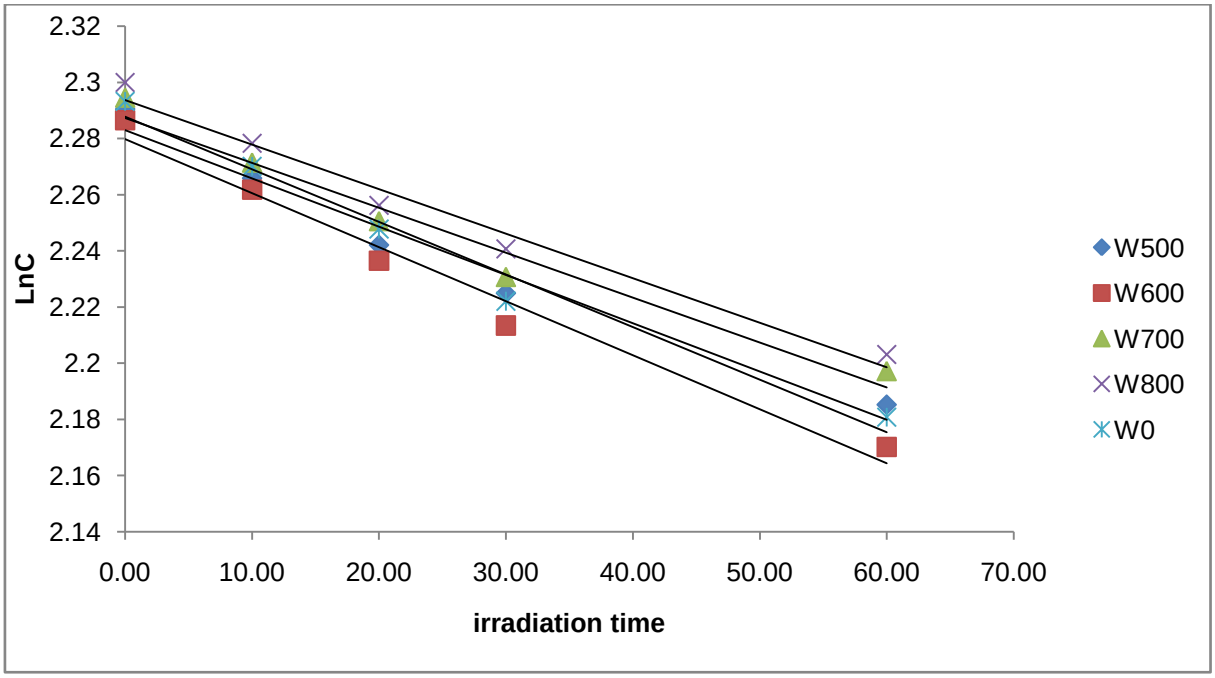

Figure 4.13: Photocatalytic degradation of MO using raw and wolframite calcined at 500^{o}C, 600^{o}C, 700^{o}C and 800^{o}C as a function of irradiation time.

However, there was no significant difference in the rate constant from raw wolframite to that calcined at 800^{o}C. The gradual increase in the activity of the photocatalyst from W0 to W600 was due to the creation of defect sides and the production of oxygen vacancies which were eliminated at higher

temperatures of 700°C and 800°C.

Table 4.11: Values of k_{app}(min^{-1}) and R^2 for MO degradation using wolframite

Sample	Rate Constant, k(min^{-1})x10^{-3}	R^2
W0	1.87	0.9849
W500	1.72	0.9962
W600	1.92	0.9777
W700	1.60	0.9990
W800	1.59	0.9775

4.3.3 Effect of Photocatalysts Dosage on the Degradation of MO

Figure 4.14 shows the effect of catalyst dosage using wolframite calcined at 600°C which gave a better activity for the degradation of MO as shown in Table 4.11. As shown in Figure 4.14, catalyst dosage of 1.2g/200ml solution of 10mg/l of MO gave the best degradation percentage of 32.53%.

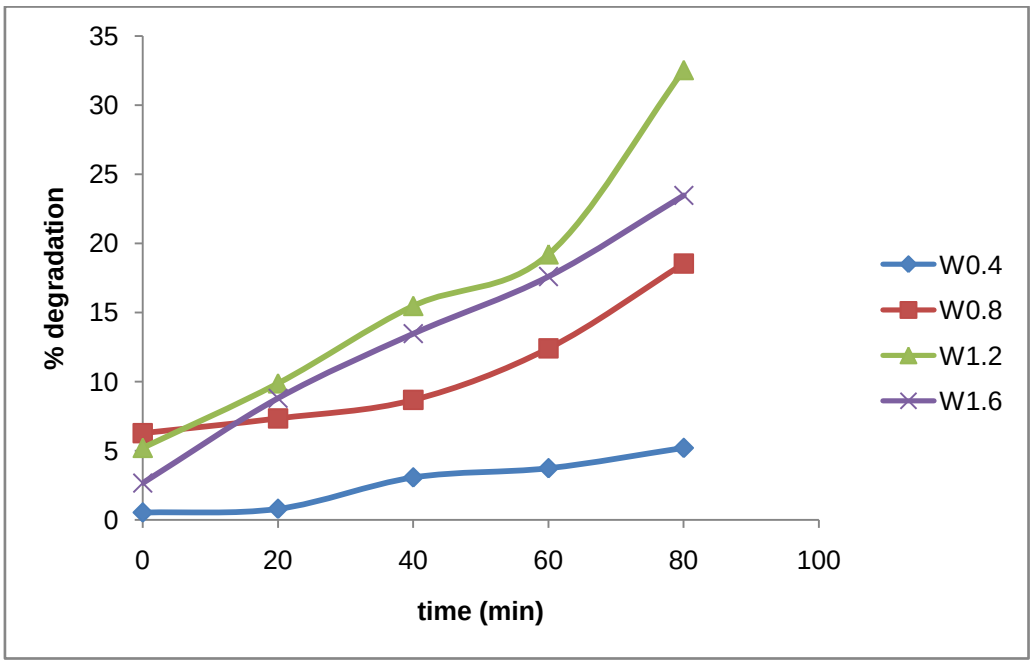

Figure 4.14: Photocatalytic degradation of MO (10mg/l) with various dosage of wolframitecalcined at 600°C as a function of irradiation time.

The rates increase with the amount of WO_3 from 0.4g to a maximum at 1.2g. This is due to the fact that more active sites are available for reaction, but when too much of WO_3 was present (above 1.2g) aggregation of particles occurred, which reduces the availability of reaction sites.

The rates also decrease because of increased solution opacity and light scattering.

Moreover, as pointed out very early in the history of study of this material the lower band gap (Eg value of WO_3 2.7 eV) results in more substantial utilization of the solar spectrum. WO_3, however, does not show any appreciable degradation under visible light irradiation because of its lower CB location with respect to the H^+/H_2 redox level.

4.3.4 Effect of Initial Substrate Concentration

The effect of these concentrations was studied on raw and calcined wolframite at 600OC and 800OC. The concentration of MO was varied between 15, 20 and 30 mg/l. It was observed that MO degradation increases with decrease in concentration of MO. This is because, for a photocatalyst reaction, substrates compete for the same number of photo-generated hole and/or hydroxyl radical and degrade them to different compounds.

Determination of rate constant of the reaction for the surface-adsorbed substrate with e^- (h^+) pair, ***kr*** and rate constant for the adsorption equilibrium, **ke** was carried out from the plots of the reciprocal of apparent rate constant k_{app} against initial concentration (C) as shown in Figure 4.15. This was also obtained based on Table E6 and Figure E11 in appendix E.

Table 4.5 shows that a higher rate constant (^{kr}=0.3422 mg/l.min) was obtained for sample W600 (calcined at 600^{o}C), 0.0890mg/l.min and 0.0364 mg/l.min for W0 and W800 respectively. For raw wolframite, low surface area, low porosity and the presence of recombination centers may have affected the activity of the photocatalyst. For wolframite calcined at 800^{o}C, increase in crystal growth which leads to low surface area, was responsible for the low activity. However, the rate constant for the adsorption equilibrium, **ke** for sample W800 was greater than rate constant of the reaction for the surface-adsorbed substrate with e^- (h^+) pair, ***kr***.

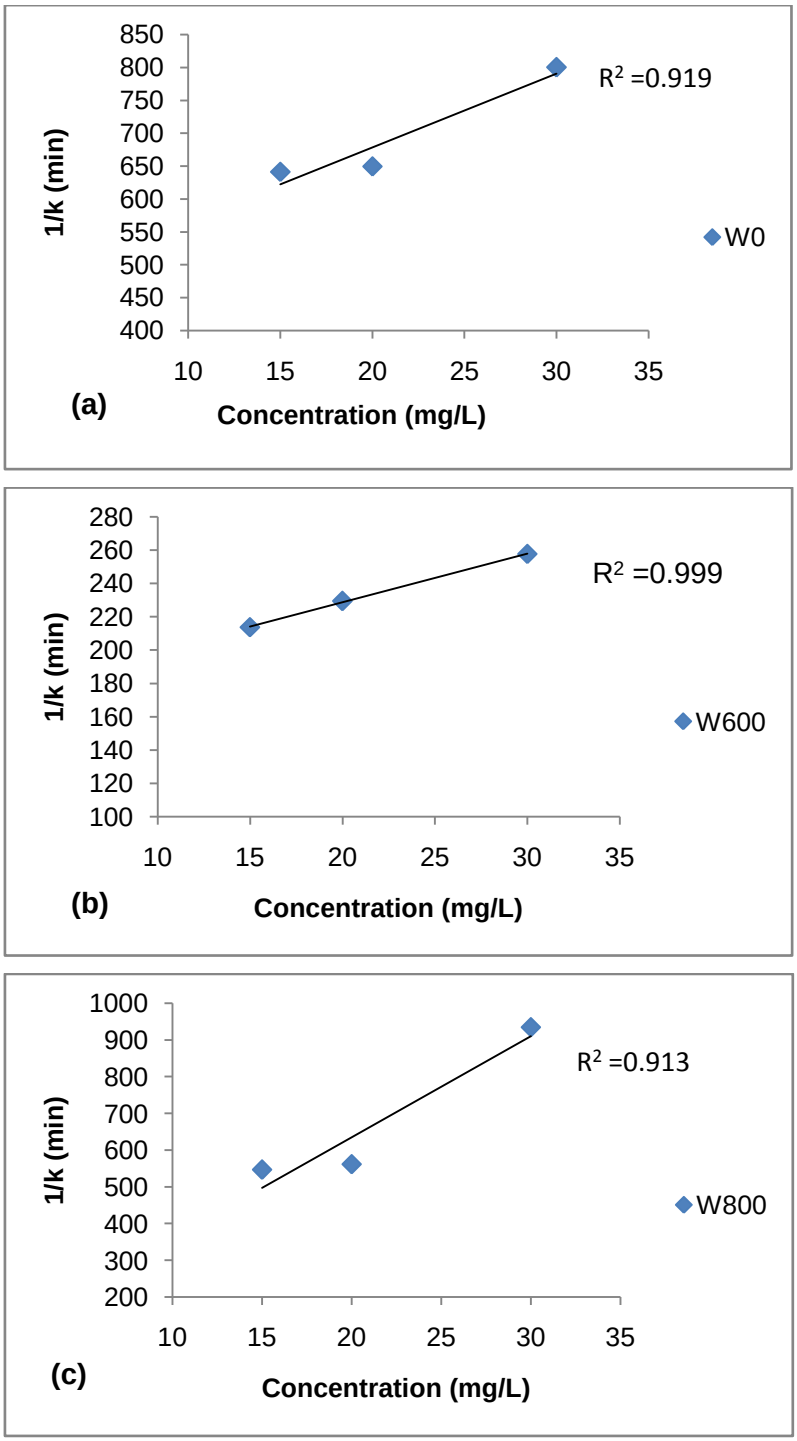

Figure 4.15: Plots of reciprocal of apparent rate constant against substrate concentration for (a) raw wolframite (W0), (b) wolframite calcined at 600^{o}C (W600) and (c) wolframite calcined 800^{o}C (W800).

CHAPTER FIVE

CONCLUSIONS AND RECOMMENDATIONS

5.1 Conclusions

The following conclusions could be drawn from the work

1. Ilmenite calcined at 500^{o}C was found to exhibit higher photocatalytic activity under visible light, though the samples generally, indicates low degradation of MO with the highest value being 19%. Calcination above this temperature lead to increase in crystal size and reduction in surface area with a corresponding phase change from Anatase to Rutile.
2. ZnO obtained through calcination of sphalerite semiconductor at 700^{o}C was found to exhibit a higher photocatalytic activity with a degradation of about 91% of MO. Above this temperature, the activity decreases due to growth in crystals and the elimination of oxygen defects.
3. Calcinatination of wolframite, an iron-manganese tungstate oxide (Fe, Mn)WO_4 at 600^{o}C gave the best degradation percentage of MO. Despite its low band gap, Wolframite still exhibit low activity under visible light irradiation.

5.2 Recommendations

1. Different indigenous sources of photocatalysts materials should be explored to investigate their photocatalytic activity.

3. Further research work should be carried out to design a pilot plant for the degradation of organic pollutants using sphalerite calcined at 700^{o}C (S700).

REFERENCES

Anna Finlayson (2006). *Synthesis, Characterisation and Modelling of Tungsten (VI) Oxide Based Visible Light Photocatalysts.* Graduate Thesis and Dissertations.

Asahi R., Morikawa T., Ohwaki T., Aoki K., Y. Taga Y. (2001) *Science* 293:269- 271.

Asbury J. B., Hao E., Wang Y., Ghosh H. N., Lian T. (2001) *Journal of Phys. Chem. B,* 105:4545.

Bahnemann W., Muneer M. and Haque, M.M. (2007). *Titanium dioxide-mediated photocatalysed degradation of few selected organic pollutants in aqueous suspensions.* Catalysis Today, 124:133-148.

Cassano A. and Alfano O. (2000).Reaction engineering of suspended solid heterogeneous photocatalytic reactors.*Catalysis Today* 58: 167-197.

Chen X. And Mao S. S. (2007). *A recent review on nanostructured titania photocatalysts:,* Chem. Rev. **107:**2891.

Chen S., Liu W. M. (1999). *Preparation and characterization of surface—coated ZnS nanioparticles.* Langmuir 15:8100.

Choi W, Termin A, Hoffmann M. R (1994). *Journal of Physical Chemistry* 98:13669-13679.

Colbeau-Justin, C., Kunst, M. (2003). *Structural influence on charge-carrier lifetimes in TiO_2 powders studied by microwave absorption.* Journal of Materials Science **38**(11): 2429-2437.

Chun H, Yizhong W (1999). *Decolorization and biodegradability of photocatalytic treated azo dyes and wool textile wastewater.* Chemosphere 39: 2107.

Daneshvar, N., Aber, S., Dorraji. M.S.S., Khataee, A.R. and Rasoulifard, M.H. (2007) Photocatalytic degradation of the insecticide diazinon in the presence of prepared nanocrystalline ZnO powders under irradiation of UV-C light. *Separation and Purification Technology,* 58: 91-98.

Daneshvar, N., Salari, D., Niaei, A. and Khataee, A.R. (2006). Photocatalytic degradation of the herbicide erioglaucine in the presence of nanosized titanium dioxide: Comparison and modeling of reaction kinetics. *Journal of Environmental Science and Health Part B,* 41:1273–1290.

Frank, S. N., and Bard, A. J., (1977).*Journal of Physical Chemistry, 81: 1484-1488.*

Fujishima, A. and Honda, K. (1972)."Electrochemical Photolysis of Water at a Semiconductor Electrode." Nature **238: 37-38.**

Fujishima, A. and Rao, T. (1997). "Recent advances in heterogeneous TiO_2 photocatalysis." Journal of Chemical Sciences **109: 471-486.**

Fujishima, A., Zhang, X. and Trykb, D.A. (2007) Heterogeneous Photocatalysis: From water photolysis to applications in environmental cleanup.*International Journal of Hydrogen Energy,* 32: 2664-2672.

Hamad, S., Cristol, S., Catlow, C. R (2002). *Surface structures and crystal morphology of ZnS:*

Computational study. Journal of Phys. Chem. B **106,** 11002–11008

Hashimoto K., Irie H., A. Fujishima A. (2005) *Journal of Applied Physics.* Japan. 44:8269-8285.

Hermann, J.M. (1999). Heterogeneous photocatalysis: fundamentals and applications to the removal of various types of aqueous pollutants. *Catalysis Today,* 53: 115-129.

Jang, Y.J., Simer, C. and Ohm, T. (2006).Comparison of zinc oxide nanoparticles and its nano-crystalline particles on the photocatalytic degradation of methylene blue.*Material Resources Bulletin*, 41(1): 67-77.

Jina Choi (2010). *Development of visible-light-active photocatalyst for hydrogen production and environmental application.*(Doctoral dissertation, California Institute of Technology, Pasadena, California).

Kitano, M., Matsuoka, M., Ueshima, M. and Anpo, M. (2007) Recent developments in titanium oxide-based photocatalysts.*Applied Catalysis A: General*, 325: 1-14.

Klug H. P., Alexander L. E. (1974). *X-Ray diffraction procedures for polycrystalline and amorphous materials* (2nd edition), Wiley, New York p. 687.

Kurtoglu Murat, (2012). *Effect of doping on the photocatalytic, electronic and mechanical properties of sol-gel titanium dioxide films*.(Doctoral dissertation, Drexel University).

Kurtoglu M. E., Longenbach T., Reddington T., Gogotsi Y. (2011). *Effect of* ***Calcinations*** *Temperature and Environment on Photocatalytic and Mechanical Properties of Ultrathin Sol-Gel Titanium Dioxide Films.* **J. Am. Ceram. Soc.,** ***94 [4] 1101-1108, 2011.***

Langford, J. and Wilson, A. (1981) *"*Scherrer after Sixty Years: A Survey and Some New Results in the Determination of Crystallite Size", *Journal of Applied Crystallography,* Vol. 11, pp. 102-103.

Linsebigler, A.L., Lu, G. and Yates, J.T. (1995). Photocatalysis on TiO_2 Surfaces: Principles, Mechanisms, and Selected Results. *Chemical Reviews,* 95: 735-758.

Litter, M.I. (1999) Heterogeneous photocatalysis Transition metal ions in photocatalytic systems.*Applied Catalysis B: Environmental*, 23: 89-114.

Magrini, K.A., Watt, A.S. and Rinehart, B. (1995).Photocatalyst evaluation for solar-based aqueous organic oxidation.*Solar Engineering ASME,* 1: 415-420.

Miyauchi, M., Nakajima A, et al. (2002). "*Photocatalysis and Photoinduced Hydrophilicity of Various Metal Oxide Thin Films*." Chemistry of Materials **14(6):** 2812-2816.

Nakabayashi S., Fujishima A. and Honda K. (1983). *Chem. Phys. Lett.* **102:**64.

Nishimoto S., Ohtani B., Yoshikawa T., Kagiya T, (1983). *J. Am. Chem. Soc.***105:**7180.

Ohno, T., Tanigawa F., Fujihara K., S. Izumi S., M. Matsumara M. (1999) *Journal of Photochem. Photobiol. A*, 127:107-110.

Pelaez M., de la Cruz A. A, Stathatos E., Falaras P., Dionysiou D. D. (2009) *Catalysis Today,* 2009, **144**, 19-25.

Pelaez M, Nolan N. T, Pillai S. C, Seery M. K, Falaras K. P, Kontos A. G, Dunlop P. M, Hamilton J. W, Byrne J, O'Shea K, Entezari M. H, Dionysiou D. D (2012). *A Review on*

*the Visible Light Active Titanium Dioxide Photocatalysts for Environmental Applications.*Applied Catalysis B 125 (2012) 331– 349

O'Regan, B. and Gratzel, M. (1991).*Nature, 353, 737-739.*

Ohtani B. (2011). *PhotocatalysisA to Z —What We Know and What We Don't Know in A Scientific Sense.* Catalysis Research Center, Hokkaido University, Sapporo 001-0021, Japan

Pankaj Chowdhury, (2012). *Solar And Visible Light Driven Photocatalysis For Sacrificial Hydrogen Generation And Water Detoxification With Chemically Modified* TiO_2. (Doctoral dissertation, The School of Graduate and Postdoctoral Studies. The University of Western Ontario London, Ontario, Canada).

Rashed M. N. and El-Amin A. A. (2007). International Journal of Physical Sciences Vol. 2 (3), pp. 073-081, March, 2007.

Sears G.W. (1981). *Determination of Specific Surface Area by Titration with Sodium Hydroxide.* Journal of Analytical Chem. 28

Serpone N., Marathamuthu P., Pichat P., Pelizzetti E., Hidaka H. (1995) *J. Photochemis Photobiology*, 85:247.

Suppan P (1994). *Chemistry and Light*. Royal Society of Chemistry, Cambridge. 33-35

Suresh P., Micahel S., Nicholas N., Miguel, Athanassios G. K., Patrick S.M., Jeremy W.J., J.Anthony B, Kevin O, Mohammad H. E, and Dionysios D. D (2012). A Review on the Visible Light Active Titanium Dioxide Photocatalysts for EnvironmentalApplications. 125: 331-349

Tsuji I., Kudo A. (2003). *H_2 evolution from aqueous sulfite solutions under visiblelight irradiation over Pb and halogen-codoped ZnS photocatalysts,* Journal of Photochemistry and Photobiology.156:249.

Wada Y., Yin H., Kitamura T., Yanagida S. (1976). *Photoreductive dechlorination of chlorinated benzene derivatives catalyzed by ZnS nanocrystallites.* Chem. Commun. 24:2683.

Wang, R., Hashimoto, K., Fujishima, A., Chikuni, M., Kojima, E., Kitamura, A., (1977). *Nature, 388, 431-432.*

Wang, Y., Huang, Y., Ho, W., Zhang, L., Zou, Z., Lee, S., (2009). *Journal of Hazardous Materials.* 26:77-87

Wolfrum E. I and Turchi S. (1992). *Comments on Reactor Dynamics in the Evaluation of Oxidation Kinetics.* Journal of Catalysis, 136, 626-628.

Yan Li, Anhuai Lu, Changqiu Wang, Xiaolei Wu (2008). *Characterization of natural sphalerite as a novel visible light-driven photocatalyst*. Journal of Hazardous Materials 170 479–486

Zhao J., Wu T., Oikawa K., Hidaka H., Serpone N. (1998). *Environmental Science Technology* 32:2394-2400.

APPENDIX A

CRYSTALLINE SIZE DETERMINATION FROM XRD DATA

The crystal sizes were determined using Scherer's equation, $D=\frac{K\lambda}{\beta cos\theta}$ from data obtained from XRD analysis. For the samples under discussion, K=0.89, λ=0.1540 nm and $\beta=(\Theta_2-\Theta_1)\frac{\pi}{180}$

Where, D = particle size, nm
λ=1.54Å
β= width at Full Width at Half Maximum (FWHM) in radians
2θ=Bragg angle

1. Raw ilmenite (I0);

   At $2\Theta=54.114^o$, $\Theta_1= 54.2^o$, $\Theta_2=54.5^o$

   $\beta=(54.5-54.2)\frac{\pi}{180} = 0.00524$

   $D1=\frac{K\lambda}{\beta cos\theta} = \frac{0.89x0.1540}{0.00524xcos\ 27.157} = 29.750nm$

   At $2\Theta=27.404^o$, $\Theta_1=27.6^o$, $\Theta_2=27.3^o$

   $\beta=(27.6-27.3)\frac{\pi}{180} = 0.00524$

   $D1= \frac{K\lambda}{\beta cos\theta} = \frac{0.89x0.1540}{0.00524xcos\ 13.702}= 30.2734nm$

   $D_{I0}=\frac{D1+D2}{2} = \frac{29.750+30.2734}{2} = 30.012nm$

2. Ilmenite calcined at 800°C

   At $2\Theta=27.43^o$, $\Theta_1=27.36^o$, $\Theta_2=27.55^o$

   $\beta=(27.55-27.36)\frac{\pi}{180} = 0.003316$

   $D1= \frac{K\lambda}{\beta cos\theta} = \frac{0.89x0.1540}{0.003316xcos\ 13.715} = 43.0224nm$

   At $2\Theta=54.288^o$, $\Theta_1=54.2^o$, $\Theta_2=54.4^o$

   $\beta=(54.4-54.2)\frac{\pi}{180} = 0.00349$

D2= $\frac{K\lambda}{\beta cos\theta}$ = $\frac{0.89x0.1540}{0.00349xcos\ 27.144}$ = 44.6203nm

D_{I800}=$\frac{D1+D2}{2}$ = $\frac{43.0224+44.6203}{2}$ = 43.82nm

3. Raw sphalerite (S0)

   At 2Θ=28.522^o, Θ_1=28.3^o, Θ_2=28.6^o

   β=(28.6-28.3)$\frac{\pi}{180}$ = 0.005234

   D1= $\frac{K\lambda}{\beta cos\theta}$ = $\frac{0.89x0.1540}{0.005234xcos\ 14.261}$ = 27.0088nm

   At 2Θ=47.45^o, Θ_1=47.25^o, Θ_2=47.54^o

   β=(47.54-47.25)$\frac{\pi}{180}$ = 0.005061

   D2= $\frac{K\lambda}{\beta cos\theta}$ = $\frac{0.89x0.1540}{0.005061xcos\ 23.725}$ = 29.577nm

   D_{S0}=$\frac{D1+D2}{2}$ = $\frac{27.0088+29.577}{2}$ = 28.293nm

4. Sphalerite calcined at 600^{o}C (S600)

   At 2Θ=28.44^o, Θ_1=28.3^o, Θ_2=28.49^o

   β=(28.49-28.30)$\frac{\pi}{180}$ = 0.003215

   D1= $\frac{K\lambda}{\beta cos\theta}$ = $\frac{0.89x0.1540}{0.003215xcos\ 14.22}$ = 43.638nm

   At 2Θ=47.35^o, Θ_1=47.25^o, Θ_2=47.45^o

   β=(47.45-47.25)$\frac{\pi}{180}$ = 0.003491

   D2= $\frac{K\lambda}{\beta cos\theta}$ = $\frac{0.89x0.1540}{0.003491xcos\ 28.675}$ = 42.869nm

   D_{S600}=$\frac{D1+D2}{2}$ = $\frac{43.638+42.869}{2}$ = 43.254nm

5. Sphalerite calcined at 700^{o}C (S700)

At $2\Theta=36.14^{o}$, $\Theta_1=36.00^{o}$, $\Theta_2=36.27^{o}$

$\beta=(36.27-36.00)\frac{\pi}{180} = 0.004712$

$D1= \frac{K\lambda}{\beta cos\theta} = \frac{0.89x0.1540}{0.004712xcos\ 18.07} = 30.594nm$

At $2\Theta=56.50^{o}$, $\Theta_1=56.30^{o}$, $\Theta_2=56.60^{o}$

$\beta=(56.6-56.3)\frac{\pi}{180} = 0.005236$

$D2= \frac{K\lambda}{\beta cos\theta} = \frac{0.89x0.1540}{0.005236xcos\ 28.25} = 29.716nm$

$D_{S700}=\frac{D1+D2}{2} = \frac{30.594+29.716}{2} = 30.155nm$

6. Sphalerite calcined at $800^{o}C$ (S800)

At $2\Theta=36.218^{o}$, $\Theta_1=36.20^{o}$, $\Theta_2=36.36^{o}$

$\beta=(36.36-36.20)\frac{\pi}{180} = 0.002793$

$D1= \frac{K\lambda}{\beta cos\theta} = \frac{0.89x0.1540}{0.002793xcos\ 18.109} = 51.638nm$

At $2\Theta=56.55^{o}$, $\Theta_1=56.48^{o}$, $\Theta_2=56.65^{o}$

$\beta=(56.65-56.48)\frac{\pi}{180} = 0.002971$

$D2= \frac{K\lambda}{\beta cos\theta} = \frac{0.89x0.1540}{0.002971xcos\ 28.275} = 52.452nm$

$D_{S800}=\frac{D1+D2}{2} = \frac{451.638+52.452}{2} = 52.045nm$

7. Raw wolframite (W0)

At $2\Theta=18.85^{o}$, $\Theta_1=18.76^{o}$ $\Theta_2=18.98^{o}$

$\beta=(18.98-18.76)\frac{\pi}{180} = 0.00384$

$D1= \frac{K\lambda}{\beta cos\theta} = \frac{0.89x0.1540}{0.00384xcos\ 9.425} = 36.590nm$

At $2\Theta=30.576^{o}$, $\Theta_1=30.3^{o}$ $\Theta_2=30.54^{o}$

β=(30.54-30.3)$\frac{\pi}{180}$ = 0.004189

D2= $\frac{K\lambda}{\beta cos\theta}$ = $\frac{0.89x0.1540}{0.004189xcos\ 15.288}$ = 34.3022nm

D_{W0}=$\frac{D1+D2}{2}$ = $\frac{36.590+34.3022}{2}$ = 35.450nm

8. Wolframite calcined at 800^{o}C (W800)

At 2Θ=30.576^{o}, Θ_1=30.47^{o}, Θ_2=30.68^{o}

β=(30.68-30.47)$\frac{\pi}{180}$ = 0.003536

D1= $\frac{K\lambda}{\beta cos\theta}$ = $\frac{0.89x0.1540}{0.003536xcos\ 15.288}$ = 38.766nm

At 2Θ=53.872^{o}, Θ_1=53.70^{o}, Θ_2=53.92^{o}

β=(53.92-53.70)$\frac{\pi}{180}$ = 0.003423

D2= $\frac{K\lambda}{\beta cos\theta}$ = $\frac{0.89x0.1540}{0.003423xcos\ 26.396}$ = 40.041nm

D_{W800}=$\frac{D1+D2}{2}$ = $\frac{38.766+40.041}{2}$ = 39.404nm

APPENDIX B

SURFACE AREA DETERMINATION USING SEAR'S METHOD

The specific surface areas (SSA) of the samples were determined using Sear's method according to the equation S (m^2/g) = 32V-25

1. Raw ilmenite (I0)

   Titre values: V_1= 1.80cm3, V_2=1.85cm3

   SSA1= 32x1.8 – 25

   SSA1= 32.60m^2/g

   SSA2 = 32x1.85 – 25

   SSA2 = 34.20m^2/g

   $SSA_{I0}= \frac{32.60 + 34.20}{2}$ =33.40m^2/g

2. Ilmenite calcined at 800^oC (I800)

   Titre values: V_1= 1.60cm^3, V_2=1.50cm^3

   SSA1= 32x1.60 – 25

   SSA1= 26.20m^2/g

   SSA2 = 32x1.50 – 25

   SSA2 = 23.00m^2/g

   $SSA_{I800}= \frac{26.20 + 23.00}{2}$ =24.60m^2/g

3. Raw sphalerite (S0)

   Titre values: V_1= 4.80cm^3, V_2=4.80cm^3

   SSA= 32x4.80 – 25

   SSA_{S0}= 128.60m^2/g

4. Sphalerite calcined at 600^oC (S600)

Titre values: V_1= 4.35cm^3, V_2=4.50cm^3

SSA1= 32x4.35 – 25

SSA1= 114.20m^2/g

SSA2 = 32x4.50 – 25

SSA2 = 119.00m^2/g

$SSA_{S600}= \frac{114.20 + 119.00}{2}$ =116.60m^2/g

5. Sphalerite calcined at 700^{o}C (S700)

   Titre values: V_1= 5.500cm^3, V_2=5.60cm^3

   SSA1= 32x5.55 – 25

   SSA1= 151.00m^2/g

   SSA2 = 32x5.60 – 25

   SSA2 = 154.20m^2/g

   $SSA_{S700}= \frac{151.00 + 154.20}{2}$ =152.60m^2/g

6. Sphalerite calcined at 800^{o}C (S800)

   Titre values: V_1= 4.20cm^3, V_2=4.10cm^3

   SSA1= 32x4.20 – 25

   SSA1= 109.40m^2/g

   SSA2 = 32x4.10 – 25

   SSA2 = 106.20m^2/g

   $SSA_{S800}= \frac{109.40 + 106.20}{2}$ =107.80m^2/g

7. Raw wolframite (W0)

   Titre values: V_1= 3.50cm^3, V_2=3.65cm^3

   SSA1= 32x3.50 – 25

SSA1= 87.00m^2/g

SSA2 = 32x3.65 – 25

SSA2 = 91.80m^2/g

$SSA_{W0}= \frac{87.00 +91.80}{2}$ =89.40m^2/g

8. Wolframite calcined at 800^oC (W800)

Titre values: V_1= 2.95cm^3, V_2=2.90cm^3

SSA1= 32x2.95 – 25

SSA1= 69.40m^2/g

SSA2 = 32x2.90 – 25

SSA2 = 67.80m^2/g

$SSA_{W800}= \frac{69.40 +67.80}{2}$ =68.60m^2/g

APPENDIX C

PHOTOCATALYTIC ACTIVITY TEST

To determine the photocatalyst with the best activity, it was necessary to determine the photocatalytic degradation of MO by both the raw and calcined samples. In order to convert the absorbance to concentration, absorbance of MO was taken at various concentrations as shown in table C. A plot of absorbance against concentration as shown in figure C gave the equation A=kC in which A= absorbance, C= concentration (mg/l), k= constant (0.075). this equation was used to convert all absorption to concentration

Table C. absorption of MO at various concentrations

C (mg/L)	A (a.u)
25.0	1.860
12.5	0.956
6.25	0.505

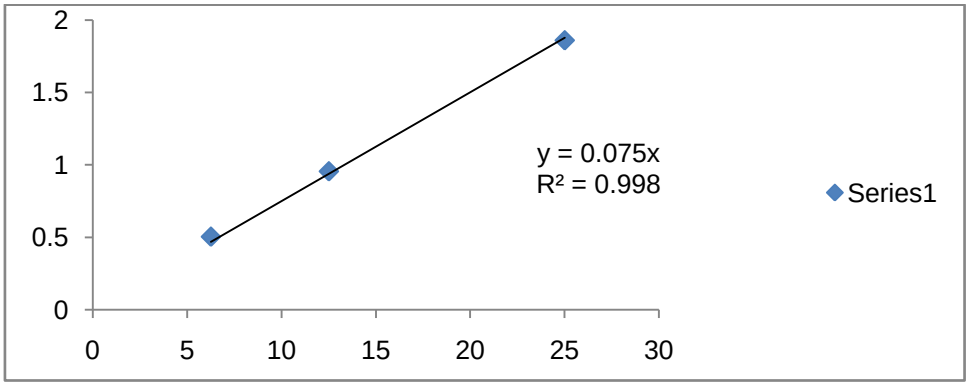

Figure C. A plot of absorption against concentration

Initial concentration of methyl orange (MO) =10mg/L

Maximum wavelength (λmax) for MO absorption =465nm

Catalyst dosage= 0.2g/200ml of solution

Source of light = 500W halogen lamp

Dark absorption= 60 minutes

IO= raw ilmenite

I500= ilmenite calcined at 500^{o}C

I600= ilmenite calcined at 600^{o}C

I700= ilmenite calined at 700^{o}C

I800= ilmenite calcined at 800^{o}C

Table C1: Absorbance test for photocatalytic degradation of MO using raw and calcined ilmenite

	ABSORBANCE				
t (min)	I0	I500	I600	I700	I800
0	0.74300	0.73300	0.73800	0.74300	0.74800
10	0.72800	0.72100	0.72700	0.73200	0.73800
20	0.71900	0.70900	0.71400	0.72100	0.73000
30	0.71100	0.69800	0.70600	0.71300	0.72300
60	0.68400	0.67400	0.67900	0.68600	0.70400

	CONCENTRATION				
t(min)	I0	I500	I600	I700	I800
0.00000	9.9067	9.7733	9.8400	9.9067	9.9733
10.00000	9.7067	9.6133	9.6933	9.7600	9.8400
20.00000	9.5867	9.4533	9.5200	9.6133	9.7333
30.00000	9.4800	9.3067	9.4133	9.5067	9.6400
60.00000	9.1200	8.9867	9.0533	9.1467	9.3867

	LN C				
t (min)	I0	I500	I600	I700	I800
0.00000	2.293208	2.279658	2.286456	2.293208	2.299915
10.00000	2.272813	2.263151	2.271438	2.278292	2.286456
20.00000	2.260373	2.246367	2.253395	2.263151	2.275556
30.00000	2.249184	2.230731	2.242127	2.251993	2.265921
60.00000	2.210470	2.195742	2.203133	2.213390	2.239290

SO= raw sphalerite
S500= sphalerite calcined at 500^{o}C
S600= sphalerite calcined at 600^{o}C
S700= sphalerite calined at 700^{o}C
S800= sphalerite calcined at 800^{o}C
Table C2: Absorbance test for photocatalytic degradation of MO using raw and calcined sphalerite

	ABSORBANCE				
t (min)	S0	S500	S600	S700	S800
0.00000	0.74900	0.74500	0.74300	0.73200	0.74200
10.00000	0.73700	0.72400	0.71900	0.70600	0.71300
20.00000	0.72100	0.70700	0.70300	0.68200	0.69200
30.00000	0.70500	0.69600	0.68100	0.65400	0.67100
60.00000	0.67800	0.64800	0.62500	0.59100	0.62700
	CONCENTRATION mg/L				
t (min)	S0	S500	S600	S700	S800
0.00000	9.986667	9.933333	9.906667	9.76	9.893333
10.00000	9.826667	9.653333	9.586667	9.413333	9.506667
20.00000	9.613333	9.426667	9.373333	9.093333	9.226667
30.00000	9.400000	9.280000	9.080000	8.720000	8.946667
60.00000	9.040000	8.640000	8.333333	7.880000	8.360000
	LN C				
t (min)	S0	S500	S600	S700	S800
0.00000	2.301251	2.295896	2.293208	2.278292	2.291861
10.00000	2.285100	2.267303	2.260373	2.242127	2.251993
20.00000	2.263151	2.243543	2.237869	2.207542	2.222098
30.00000	2.240710	2.227862	2.206074	2.165619	2.191281
60.00000	2.201659	2.156403	2.120264	2.064328	2.123458

WO= raw wolframite
W500= wolframite calcined at 500^{o}C
W600= wolframite calcined at 600^{o}C
W700= wolframite calcined at 700^{o}C
W800= wolframite calcined at 800^{o}C

Table C3: Absorbance test for photocatalytic degradation of MO using raw and calcined wolframite

	ABSORBANCE				
t (min)	W0	W500	W600	W700	W800
0.00000	0.74300	0.74100	0.73800	0.74400	0.74800
10.00000	0.72600	0.72300	0.72000	0.72700	0.73200
20.00000	0.71000	0.70600	0.70200	0.71200	0.71600
30.00000	0.69200	0.69400	0.68600	0.69800	0.70500
60.00000	0.66400	0.66700	0.65700	0.67500	0.67900
	CONCENTRATION				
t (min)	W0	W500	W600	W700	W800
0.00000	9.906667	9.880000	9.840000	9.920000	9.973333
10.00000	9.680000	9.640000	9.600000	9.693333	9.760000
20.00000	9.466667	9.413333	9.360000	9.493333	9.546667
30.00000	9.226667	9.253333	9.146667	9.306667	9.400000
60.00000	8.853333	8.893333	8.760000	9.000000	9.053333

		LNC			
t (min)	W0	W500	W600	W700	W800
0.00000	2.29321	2.290513	2.286456	2.294553	2.299915
10.00000	2.27006	2.265921	2.261763	2.271438	2.278292
20.00000	2.24777	2.242127	2.236445	2.250590	2.256192
30.00000	2.22209	2.224984	2.21339	2.230731	2.240710
60.00000	2.18079	2.185302	2.170196	2.197225	2.203133

APPENDIX D

EFFECT OF CATALYSTS DOSAGE

The effect of catalyst dosage was investigated using ilmenite calcined at 500^{o}C, sphalerite calcined at 700^{o}C and wolframite calcined at 600^{o}C which gave a better activity for the degradation of MO.

Ilmenite calcined at 500^{o}C

I0.5 = 0.5g/200ml solution
I1.0 = 1.0g/200ml solution
I1.5= 1.5g/200ml solution
I2.0 = 2.0g/200ml solution

Table D1: Absorbance test for photocatalytic degradation of MO using ilmenite calcined at 500^{o}C

	ABSORBANCE			
t (min)	I0.5	I1.0	I1.5	I2.0
0	0.744	0.73	0.732	0.748
20	0.715	0.702	0.703	0.744
40	0.693	0.688	0.678	0.728
60	0.659	0.653	0.636	0.719
80	0.642	0.632	0.607	0.717

	CONCENTRATION			
T	I0.5	I1	I1.5	I2
0	9.920000	9.733333	9.760000	9.973333
20	9.533333	9.360000	9.373333	9.920000
40	9.240000	9.173333	9.040000	9.706667
60	8.786667	8.706667	8.480000	9.586667
80	8.560000	8.426667	8.093333	9.560000

	DEGRADATION			
T	I0.5	I1	I1.5	I2
0	0.008000	0.026667	0.024000	0.002667
20	0.046667	0.064000	0.062667	0.008000
40	0.076000	0.082667	0.096000	0.029333
60	0.121333	0.129333	0.152000	0.041333
80	0.144000	0.157333	0.190667	0.044000

	% DEGRADATION			
T	I0.5	I1	I1.5	I2
0	0.800000	2.666667	2.400000	0.266667

20	4.666667	6.400000	6.266667	0.800000
40	7.600000	8.266667	9.600000	2.933333
60	12.13333	12.93333	15.20000	4.133333
80	14.40000	15.73333	19.06667	4.400000

Sphalerite calcined at 700^{o}C
S0.5 = 0.5g/200ml solution
S1.0 = 1.0g/200ml solution
S1.5= 1.5g/200ml solution
S2.0 = 2.0g/200ml solution

Table D2: Absorbance test for photocatalytic degradation of MO using sphalerite calcined at 700^{o}C

	ABSORBANCE			
t (min)	S0.5	S1.0	S1.5	S2.0
0	0.736	0.736	0.655	0.736
20	0.695	0.185	0.570	0.634
40	0.685	0.172	0.425	0.582
60	0.536	0.095	0.317	0.349
80	0.163	0.068	0.300	0.332

CONCENTRATION

t(min)	S0.5	S1.0	S1.5	S2.0
0	9.8133	9.8133	8.7333	9.8133
20	9.2667	2.4667	7.6000	8.4533
40	9.1333	2.2933	5.6667	7.7600
60	7.1467	1.2667	4.2267	4.6533
80	2.1733	0.9067	4.0000	4.4267

	DEGRADATION			
t (min)	S0.5	S1.0	S1.5	S2.0
0	0.0187	0.0187	0.1267	0.0187
20	0.0733	0.7533	0.2400	0.1547
40	0.0867	0.7707	0.4333	0.2240
60	0.2853	0.8733	0.5773	0.5347
80	0.7827	0.9093	0.6000	0.5573

	%DEGRADATION			
t (min)	S0.5	S1	S1.5	S2.0
0	1.8667	1.86667	12.6667	1.8667
20	7.3333	75.3333	24.0000	15.4667
40	8.6667	77.0667	43.3333	22.4000
60	28.5333	87.3333	57.7333	53.4667
80	78.2667	90.9333	60.0000	55.7333

Wolframite calcined at 600^{o}C
W0.4 = 0.4g/200ml solution
W0.8 = 0.8g/200ml solution
W1.2= 1.2g/200ml solution
W1.6 = 1.6g/200ml solution

Table D3: Absorbance test for photocatalytic degradation of MO using wolframite calcined at 600oC

	ABSORBANCE			
t (min)	W0.4	W0.8	W1.2	W1.6
0	0.746	0.703	0.711	0.73
20	0.744	0.695	0.676	0.684
40	0.727	0.685	0.634	0.649
60	0.722	0.657	0.606	0.618
80	0.711	0.611	0.506	0.574

	CONCENTRATION			
t (min)	W0.4	W0.8	W1.2	W1.6
0	9.946667	9.373333	9.48	9.733333
20	9.920000	9.266667	9.013333	9.120000
40	9.693333	9.133333	8.453333	8.653333
60	9.626667	8.760000	8.080000	8.240000
80	9.480000	8.146667	6.746667	7.653333

DEGRADATION				
t(min)	W0.4	W0.8	W1.2	W1.6
0	0.005333	0.062667	0.052000	0.026667
20	0.008000	0.073333	0.098667	0.088000
40	0.030667	0.086667	0.154667	0.134667
60	0.037333	0.124000	0.192000	0.176000
80	0.052000	0.185333	0.325333	0.234667

%DEGRADATION				
t (min)	W0.4	W0.8	W1.2	W1.6
0	0.533333	6.266667	5.200000	2.666667
20	0.800000	7.333333	9.866667	8.800000
40	3.066667	8.666667	15.46667	13.46667
60	3.733333	12.40000	19.20000	17.60000
80	5.200000	18.53333	32.53333	23.46667

APPENDIX E

EFFECT OF SUBSTRATE (MO) CONCENTRATION

Raw ilmenite (I0)

The concentration was varied between 15, 20 and 30 mg/L of MO. The tables below were used to determine apparent rate constant, k_{app}, ***kr*** and **ke.**

Table E1: Absorbance test for photocatalytic degradation of MO using raw ilmenite (I0) at a concentration of 15, 20, and 30mg/L

ABSORBANC a.u			
t (min)	I0 (15)	I0 (20)	I0 (30)
0	1.021	1.382	2.102
20	0.935	1.265	1.93
40	0.912	1.236	1.904
60	0.897	1.216	1.883
80	0.884	1.198	1.868
	CONCENTRATION IN mg/L		
t (min)	I0 (15)	I0 (20)	I0 (30)
0	13.61333	18.42667	28.02667
20	12.46667	16.86667	25.73333
40	12.16	16.48	25.38667
60	11.96	16.21333	25.10667
80	11.78667	15.97333	24.90667
	Ln C		
t (min)	I0 (15)	I0 (20)	I0 (30)
0	2.61105	2.913799	3.333156
20	2.523058	2.825339	3.247787
40	2.498152	2.802148	3.234224
60	2.481568	2.785834	3.223133
80	2.466969	2.770921	3.215136

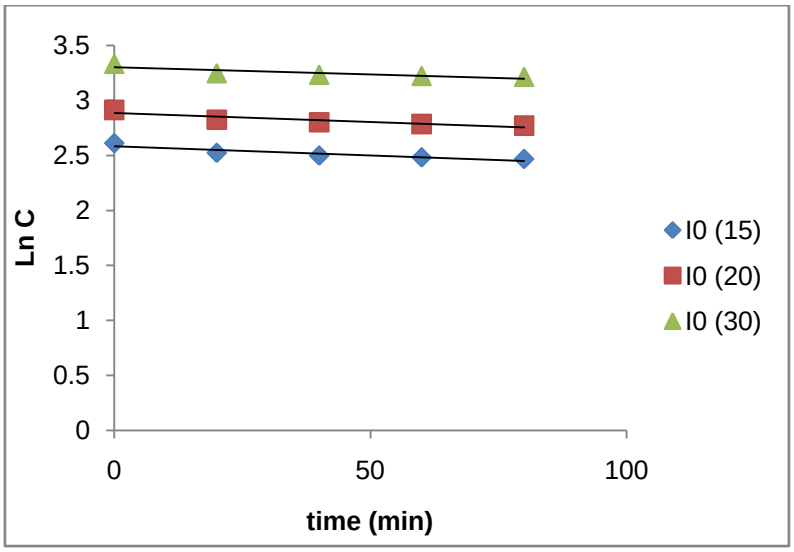

Figure E1: Photocatalytic degradation of MO at 15, 20 and 30mg/L with 1.5g dose of raw ilmenite as a function of irradiation time.

Table E2: Apparent rate constant, ***k*** values for the photocatalytic degradation of MO using raw ilmenite (I0) at a concentration of 15, 20, and 30mg/L.

Co(mg)	k(mn^{-1})	1/k(min)
15	0.00165	606.0606
20	0.00163	613.4969
30	0.0013	769.2308

Ilmenite calcined at 500^{o}C (I500)

Table E3: Absorbance test for photocatalytic degradation of MO using ilmenite calcined at 500^{o}C (I500) at a concentration of 15, 20, and 30mg/L

	ABSORBANCE a.u		
t (min)	I500 (15)	I500 (20)	I500 (30)
0	1.013	1.38	2.106
20	0.965	1.316	2.009
40	0.926	1.264	1.932
60	0.867	1.186	1.814
80	0.81	1.089	1.701
	CONCENTRATION in mg/L		
t (min)	I500 (15)	I500 (20)	I500 (30)
0	13.50667	18.4	28.08
20	12.86667	17.54667	26.78667
40	12.34667	16.85333	25.76
60	11.56	15.81333	24.18667
80	10.8	14.52	22.68
	Ln C		

t (min)	I500 (15)	I500 (20)	I500 (30)
0	2.603183	2.912351	3.335058
20	2.55464	2.864864	3.287904
40	2.513386	2.824548	3.248823
60	2.447551	2.760853	3.185802
80	2.379546	2.675527	3.121483

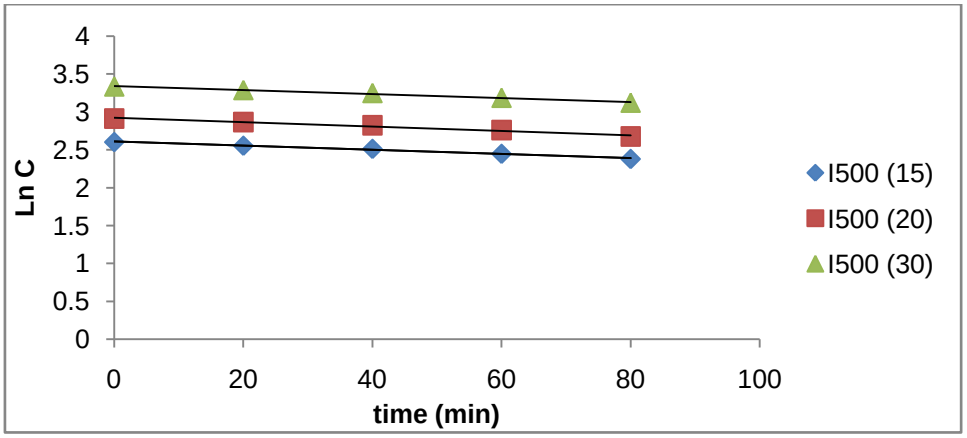

Figure E2: Photocatalytic degradation of MO at 15, 20 and 30mg/L with 1.5g dose of ilmenite calcined at 500oC as a function of irradiation time.

Table E4: Apparent rate constant, ***k*** values for the photocatalytic degradation of MO using ilmenite calcined at 500^{o}C (I500) at a concentration of 15, 20, and 30mg/L

Co(mg)	k(mn^{-1})	1/k(min)
15	0.00289	346.0208
20	0.00277	361.0108
30	0.00259	386.1004

Ilmenite calcined at 800^{o}C (I800)

Table E5: Absorbance test for photocatalytic degradation of MO using ilmenite calcined at 800^{o}C (I800) at a concentration of 15, 20, and 30mg/L

ABSORBANCE a.u

t (min)	I800 (15)	I800(20)	I800(30)
0	0.982	1.329	2.004
20	0.914	1.297	1.907
40	0.901	1.221	1.866
60	0.887	1.102	1.834
80	0.875	1.069	1.809

CONC. (C) in mg/L

t (min)	I800 (15)	I800(20)	I800 (30)
0	13.09333	17.72	26.72
20	12.18667	17.29333	25.42667

40	12.01333	16.28	24.88
60	11.82667	14.69333	24.45333
80	11.66667	12.92	24.12

	Ln C		
t (min)	I800 (15)	I800 (20)	I800 (30)
0	2.572103	2.874694	3.285412
20	2.500342	2.850321	3.235798
40	2.486017	2.789937	3.214064
60	2.470357	2.687394	3.196767
80	2.456736	2.558776	3.183041

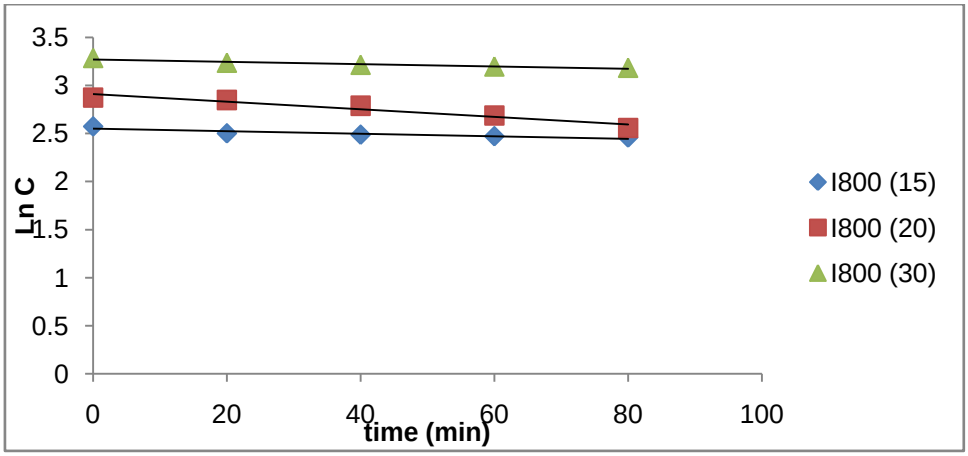

Figure E3: Photocatalytic degradation of MO at 15, 20 and 30mg/L with 1.5g dose of ilmenite calcined at 800oC as a function of irradiation time.

Table E6: Apparent rate constant, ***k*** values for the photocatalytic degradation of MO using ilmenite calcined at 800oC (I800) at a concentration of 15, 20, and 30mg/L

Co(mg)	*k*(mn-1)	1/*k*(min)
15	0.00157	636.9427
20	0.0013	769.2308
30	0.00122	819.6721

Raw sphalerite (SO)

Table E7: Absorbance test for photocatalytic degradation of MO using raw sphalerite (S0) at a concentration of 15, 20, and 30mg/L

	ABSORBANCE a.u		
t (min)	S0(15)	S0(20)	S0(30)
0	1.036	1.401	2.112
20	0.923	1.25	1.946
40	0.864	1.172	1.847
60	0.832	1.123	1.813

80	0.822	1.116	1.784
	CONC. (C) in mg/L		
t (min)	S0(15)	S0(20)	S0(30)
0	13.81333	18.68	28.16
20	12.30667	16.66667	25.94667
40	11.52	15.62667	24.62667
60	11.09333	14.97333	24.17333
80	10.96	14.88	23.78667
	Ln C		
t (min)	S0 (15)	S0 (20)	S0 (30)
0	2.625634	2.927453	3.337903
20	2.510141	2.813411	3.256043
40	2.444085	2.748979	3.20383
60	2.406344	2.706271	3.18525
80	2.394252	2.700018	3.169125

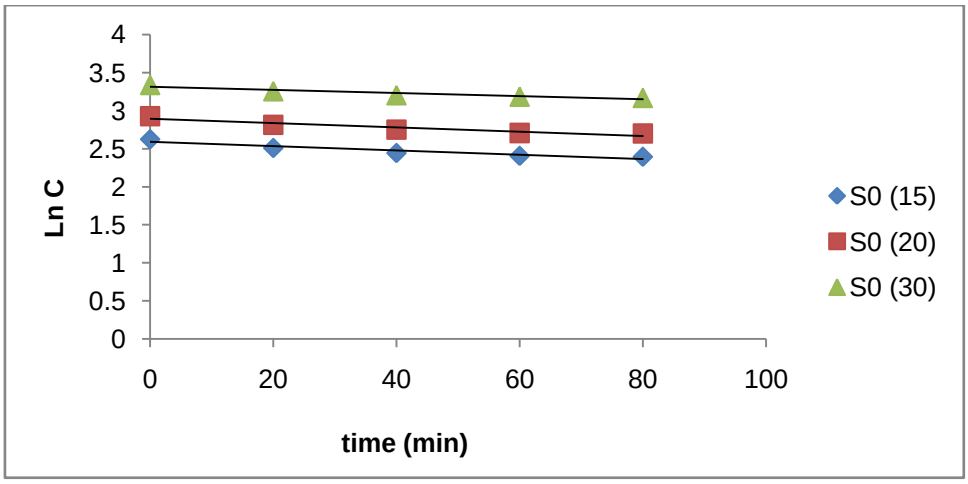

Figure E4: Photocatalytic degradation of MO at 15, 20 and 30mg/L with 1.0g dose of raw sphalerite as a function of irradiation time.

Table E8: Apparent rate constant, ***k*** values for the photocatalytic degradation of MO using raw sphalerite (S0) at a concentration of 15, 20, and 30mg/L.

Co(mg)	k(mn^{-1})	1/k(min)
15	0.00283	353.3569
20	0.00281	355.8719
30	0.00204	490.1961

Sphalerite calcined at 600^{o}C (S600)

Table E9: Absorbance test for photocatalytic degradation of MO using sphalerite calcined at 600oC (S600) at a concentration of 15, 20, and 30mg/L

		ABSORBANCE a.u	
t (min)	S6(15)	S6(20)	S6(30)
0	1.025	1.386	2.109

20	0.909	1.232	1.985
40	0.863	1.18	1.945
60	0.724	0.985	1.608
80	0.591	0.798	1.239

	CONC. (C) in mg/L		
t (min)	S6(15)	S6(20)	S6(30)
0	13.66667	18.48	28.12
20	12.12	16.42667	26.46667
40	11.50667	15.73333	25.93333
60	9.653333	13.13333	21.44
80	7.88	10.64	16.52

	Ln C		
t (min)	S6 (15)	S6(20)	S6(30)
0	2.61496	2.916689	3.336481
20	2.494857	2.798906	3.275886
40	2.442927	2.755782	3.255529
60	2.267303	2.575154	3.065258
80	2.064328	2.36462	2.804572

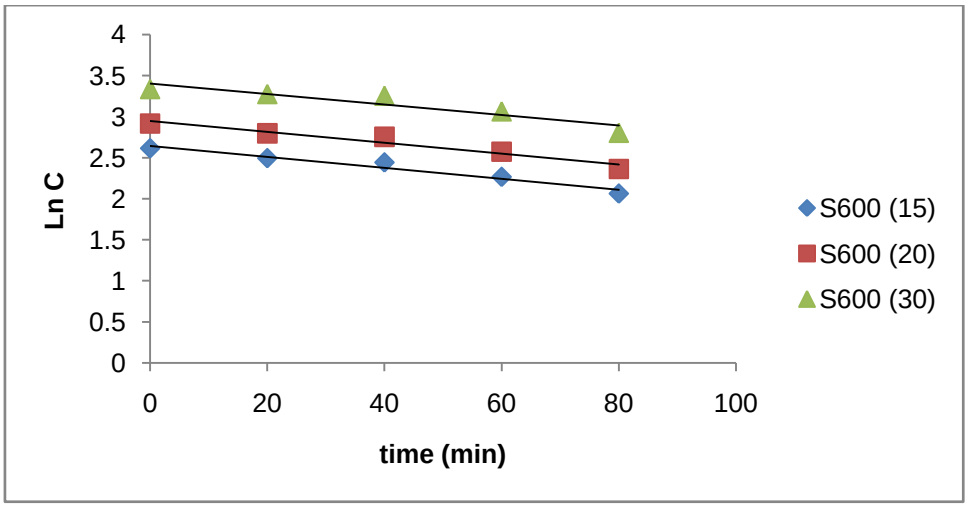

Figure E5: Photocatalytic degradation of MO at 15, 20 and 30mg/L with 1.0g dose of sphalerite calcined at 600oC as a function of irradiation time.

Table E10: Apparent rate constant, ***k*** values for the photocatalytic degradation of MO using sphalerite calcined at 600oC (S600) at a concentration of 15, 20, and 30mg/L.

Co(mg)	$k(mn^{-1})$	$1/k$(min)
15	0.00664	150.6024
20	0.00655	152.6718
30	0.00637	156.9859

Sphalerite calcined at 700^{o}C (S700)

Table E11: Absorbance test for photocatalytic degradation of MO using sphalerite calcined at 700oC (S700) at a concentration of 15, 20, and 30mg/L

	ABSORBANCE a.u		
t (min)	S7(15)	S7(20)	S7(30)
0	0.913	1.358	2.118
20	0.862	1.237	1.965
40	0.774	1.169	1.815
60	0.514	0.904	1.498
80	0.231	0.328	0.529
	CONC (C) in mg/L		
t (min)	S7(15)	S7(20)	S7(30)
0	12.17333	18.10667	28.24
20	11.49333	16.49333	26.2
40	10.32	15.58667	24.2
60	6.853333	12.05333	19.97333
80	3.08	4.373333	7.053333
	Ln C		
t (min)	S7(15)	S7(20)	S7(30)
0	2.499248	2.89628	3.340739
20	2.441767	2.802956	3.265759
40	2.334084	2.746416	3.186353
60	1.924735	2.489341	2.994398
80	1.12493	1.475525	1.9535

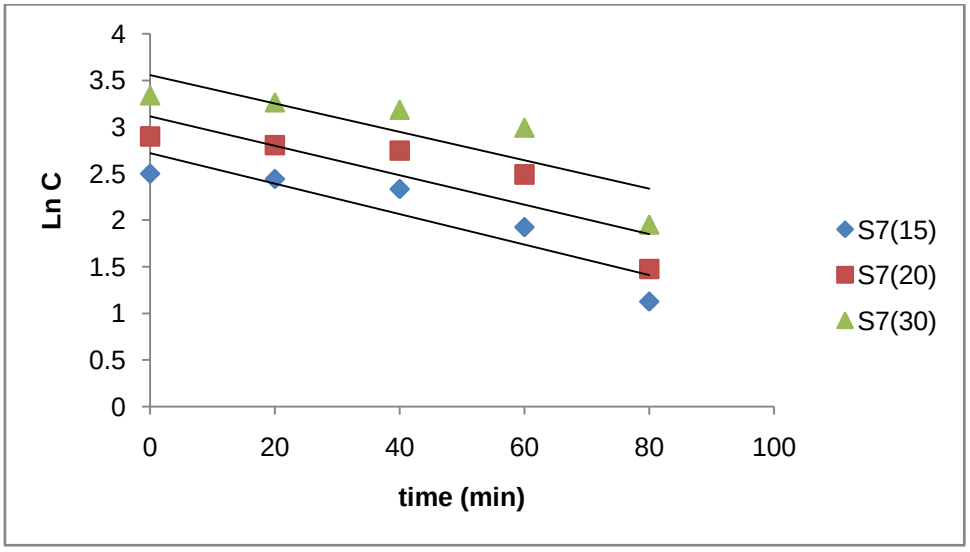

Figure E6: Photocatalytic degradation of MO at 15, 20 and 30mg/L with 1.0g dose of sphalerite calcined at 700^{o}C as a function of irradiation time.

Table E12: Apparent ***k*** values for the photocatalytic degradation of MO using ilmenite calcined at 700oC (S700) at a concentration of 15, 20, and 30mg/L

Co(mg)	$k(mn^{-1})$	$1/k$(min)
15	0.01633	61.23699
20	0.01578	63.37136
30	0.01523	65.65988

Raw wolframite (W0)

Table E13: Absorbance test for photocatalytic degradation of MO using raw wolframite (W0) at a concentration of 15, 20, and 30mg/L

	ABSORBANCE a.u		
t (min)	W0(15)	W0(20)	W0(30)
0	1.018	1.377	2.096
20	0.924	1.252	1.929
40	0.902	1.223	1.903
60	0.893	1.210	1.886
80	0.886	1.201	1.871
	CONC. (C) in mg/L		
t (min)	W0(15)	W0(20)	W0(30)
0	13.57333	18.36000	27.94667
20	12.32000	16.69333	25.72000
40	12.02667	16.30667	25.37333
60	11.90667	16.13333	25.14667
80	11.81333	16.01333	24.94667
	Ln C		
t (min)	W0(15)	W0(20)	W0(30)
0	2.608107	2.910174	3.330298
20	2.511224	2.815009	3.247269
40	2.487126	2.791574	3.233699
60	2.477098	2.780888	3.224725
80	2.469229	2.773422	3.21674

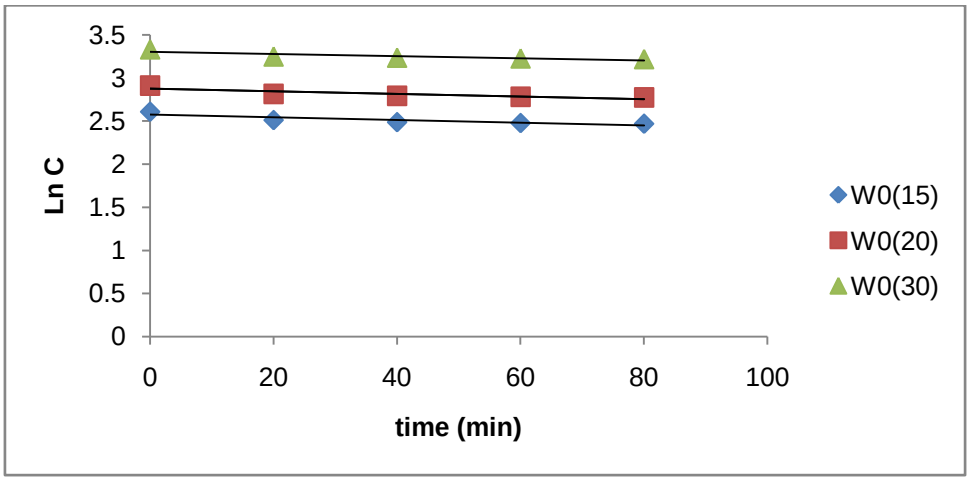

Figure E7: Photocatalytic degradation of MO at 15, 20 and 30mg/L with 1.2g dose of raw wolframite as a function of irradiation time.

Table E14: Apparent rate constant, ***k*** values for the photocatalytic degradation of MO using raw wolframite (W0) at a concentration of 15, 20, and 30mg/L.

Co(mg)	*k*(mn^{-1})	1/*k*(min)
15	0.00156	641.0256
20	0.00154	649.3506
30	0.00125	800.0000

Wolframite calcined at 600^{o}C (W600)

Table E15: Absorbance test for photocatalytic degradation of MO using wolframite calcined at 600oC (W600) at a concentration of 15, 20, and 30mg/L

	ABSORBANCE a.u		
t (min)	W6(15)	W6(20)	W6(30)
0	1.088	1.47	2.173
20	1.009	1.365	2.078
40	0.941	1.274	1.942
60	0.835	1.19	1.862
80	0.749	1.018	1.558
	CONC. (C) in mg/L		
t (min)	W6(15)	W6(20)	W6(30)
0	14.50667	19.6	28.97333
20	13.45333	18.2	27.70667
40	12.54667	16.98667	25.89333
60	11.13333	15.86667	24.82667
80	9.986667	13.57333	20.77333
	Ln C		
t (min)	W6(15)	W6(20)	W6(30)
0	2.674608	2.97553	3.366376
20	2.599227	2.901422	3.321673
40	2.529455	2.832429	3.253986
60	2.409944	2.76422	3.211918
80	2.301251	2.608107	3.03367

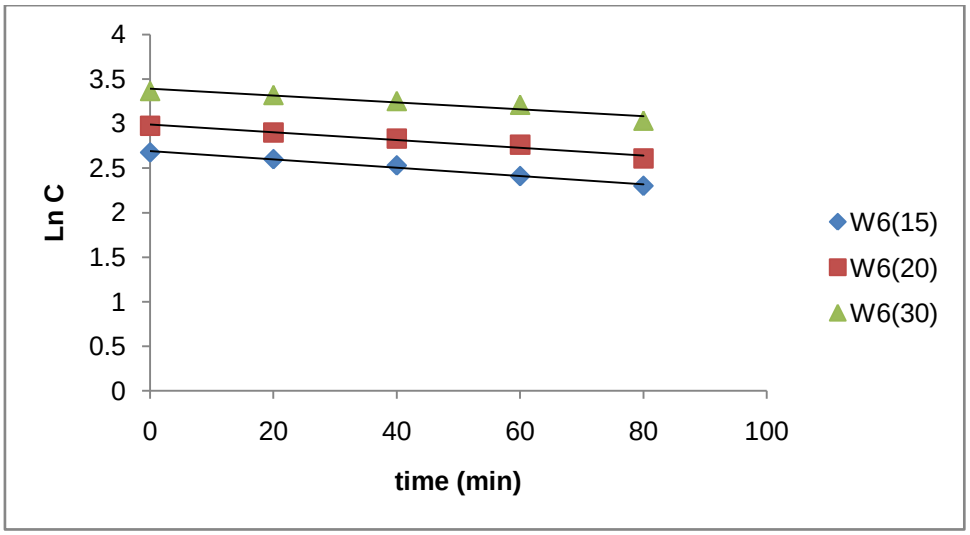

Figure E8: Photocatalytic degradation of MO at 15, 20 and 30mg/L with 1.2g dose of wolframite calcined at 600^{o}C as a function of irradiation time.

Table E16: Apparent rate constant, ***k*** values for the photocatalytic degradation of MO using wolframite calcined at 600^{o}C (W600) at a concentration of 15, 20, and 30mg/L

Co(mg)	*k*(mn^{-1})	1/*k*(min)
15	0.00468	213.6752
20	0.00436	229.3578
30	0.00388	257.732

Wolframite calcined at 800^{o}C (W800)

Table E17: Absorbance test for photocatalytic degradation of MO using wolframite calcined at 800^{o}C (W800) at a concentration of 15, 20, and 30mg/L

	ABSORBANCE a.u		
t (min)	W8(15)	W8(20)	W8(30)
0	1.004	1.359	2.008
20	0.900	1.238	1.896
40	0.882	1.196	1.863
60	0.871	1.175	1.845
80	0.850	1.168	1.829
	CONC. (C) in mg/L		
t (min)	W8(15)	W8(20)	W8(30)
0	13.38667	18.12000	26.77333
20	12.00000	16.50667	25.28000
40	11.76000	15.94667	24.84000
60	11.61333	15.66667	24.60000
80	11.33333	15.57333	24.38667

	Ln C		
t (min)	W8(15)	W8(20)	W8(30)

0	2.594259	2.897016	3.287406
20	2.484907	2.803764	3.230014
40	2.464704	2.76925	3.212455
60	2.452154	2.751535	3.202746
80	2.427748	2.74556	3.194037

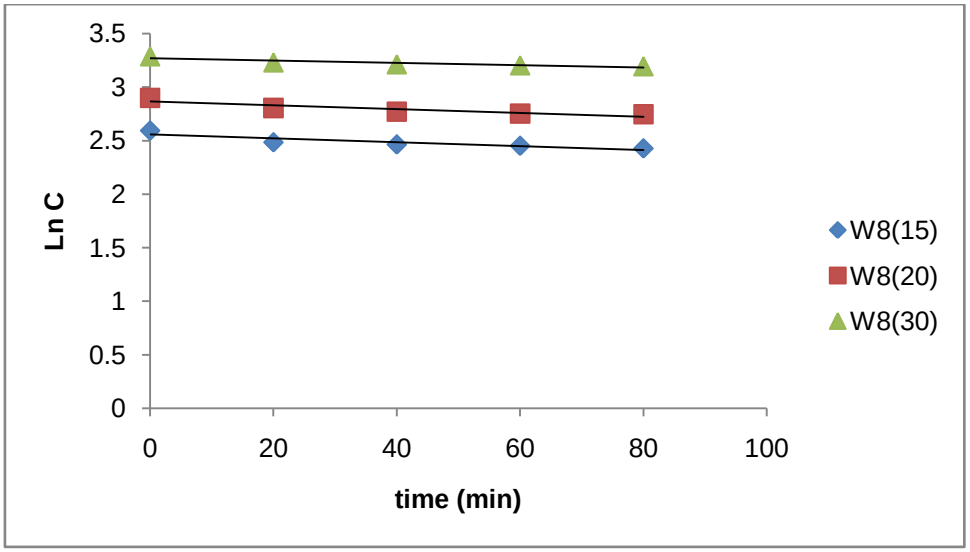

Figure E9: Photocatalytic degradation of MO at 15, 20 and 30mg/L with 1.2g dose of wolframite calcined at 800^{o}C as a function of irradiation time.

Table E18: Apparent rate constant, ***k*** values for the photocatalytic degradation of MO using wolframite calcined at 800oC (W800) at a concentration of 15, 20, and 30mg/L

Co(mg)	*k*(mn^{-1})	1/*k*(min)
15	0.00183	546.4481
20	0.00178	561.7978
30	0.00107	934.5794